

Negative Lift Generation in a Tidal Device Structure

This thesis is submitted in fulfilment of the
requirements for the degree of Master of Science
(MSc by Research)

By Olivia Thilleul

School of Engineering

October 2009

Negative Lift Generation in a Tidal Device Structure

This thesis is submitted in fulfilment of the
requirements for the degree of Master of Science
(MSc by Research)

By Olivia Thilleul

Supervised by F. Trarieux

Department of Applied Mechanics
Offshore Engineering and Naval Architecture group

Academic year 2008 – 2009

Presentation October 2009

*© Cranfield University 2009. All rights reserved. No part of
this publication may be reproduced without the written
permission of the copyright owner.*

ABSTRACT

Becoming aware of the impact of global warming, all countries of the European Union have agreed to produce 20% of their electricity from renewable energy by 2020. Hence, a new market emerged to develop more efficient technologies of sustainable power production.

Cranfield University has been involved since 2006 in wave and tidal energy design projects through various government agencies funded partnerships with the emerging industry of marine renewable energy. This thesis is based on one of these projects called “DeltaStream” which was developed by Tidal Energy Ltd (TEL).

The tidal stream turbine is one of the most efficient concepts in marine renewable energy, because of the high predictability of tidal streams compared to wave and wind energy. Many devices are currently being developed in the UK. Most of them are moored to the seabed using traditional methods used in the offshore oil industry, which means drilling the sea floor.

The goal of this work is to avoid drilling the seabed by adding hydrofoils on the structure. Indeed, by setting a hydrofoil in the tidal stream, the goal is to prove that a downward lift force is created and is efficient enough to maintain the structure at its location, avoiding mooring costs and ecological issues relative to drilling the sea floor.

Computational Fluid Dynamics (CFD) models have been performed, studying the sensitivity of mesh size compared to results quality, and testing then different hydrofoils to get the best downward lift force in local conditions. The main characteristics of the simulation are unsteady and one phase. The chosen geometry is a “quasi-2D” domain in order to minimize computational requirements.

A validation case has been first performed on a well-known geometry of a circular cylinder, to compare analytical results and CFD data. Small variations between results validated the model to enable us to use the model on a less-known simulation such as a hydrofoil. Different parameters influencing the efficiency of the hydrofoil in terms of lift production and drag reduction have been tested.

These results have been compared with tank tests undertaken by the OENA Group in June-July 2009 in IFREMER (France). And complementary studies have been performed to compare these results and CFD results.

CONTENTS

ABSTRACT.....	i
CONTENTS.....	iii
ACKNOWLEDGEMENTS.....	viii
LIST OF SYMBOLS.....	ix
CHAPTER 1: INTRODUCTION.....	1
1.1 General background	1
1.2 Scope of work.....	2
1.3 Structure of the thesis	3
CHAPTER 2: ENERGY MARKET AND TIDAL STREAM DEVICES	5
2.1 Energy in the world and in UK.....	5
2.1.1 <i>Production and consumption.....</i>	5
2.1.2 <i>Energy policy.....</i>	7
2.1.3 <i>Marine renewable energy potential in UK.....</i>	8
2.2 Existing tidal stream energy extraction systems	9
2.2.1 <i>Types of marine current turbine.....</i>	9
2.2.1.1 <i>Horizontal axis turbine</i>	9
2.2.1.2 <i>Venturi Effect.....</i>	10
2.2.1.3 <i>Oscillating Hydrofoil.....</i>	11
2.2.1.4 <i>Vertical Axis Turbine.....</i>	11
2.2.2 <i>Power harnessed from a tidal stream turbine</i>	12
2.3 The DeltaStream Concept	12
2.3.1 <i>The device.....</i>	12
2.3.2 <i>Location.....</i>	13
2.4 Rationale of the research	14
CHAPTER 3: LITERATURE REVIEW.....	18
3.1 Background.....	18
3.2 Typical flow regimes around a circular cylinder	19
3.3 Theory of lift	22
3.4 Drag and lift coefficients.....	24
3.5 Hydrofoil shape	26

3.6 Numerical methods	28
CHAPTER 4: MATHEMATICAL APPROACH.....	29
4.1 Governing equations of fluid dynamics.....	29
4.1.1 Mass conservation.....	29
4.1.2 The momentum equation	31
4.1.3 The energy equation	34
4.1.4 Turbulence equation.....	34
4.2 Important dimensionless parameters.....	37
4.2.1 Reynolds number	37
4.2.2 Froude number.....	37
4.3 Discretization and solution theory	37
4.3.1 General principles.....	37
4.3.2 Convergence.....	40
4.3.3 Accuracy.....	40
CHAPTER 5: CFD MODELLING	41
5.1 Introduction	41
5.2 Geometry and meshing.....	41
5.2.1 Choice of Geometry.....	41
5.2.2 Choice of Mesh.....	42
5.2.3 The Boundary Layer description.....	42
5.3 Pre-processing stage.....	44
5.3.1 Boundary conditions.....	44
5.3.2 A special boundary condition : the velocity inlet.....	45
5.3.3 Simulation type	46
5.4 Solver stage	47
5.5 Post-processing stage	47
CHAPTER 6: VALIDATION CALCULATIONS	49
6.1 Introduction	49
6.2 Geometry and set up	49
6.2.1 Reynolds number	50
6.2.2 Boundary layer.....	50
6.2.3 Drag coefficient for a cylinder near a wall.....	50
6.3 Results	52
6.3.1 Mesh size influence.....	52

6.3.1.1	<i>Boundary layer mesh</i>	52
6.3.1.2	<i>Number of nodes, sensitivity study</i>	53
6.3.2	<i>Velocity influence</i>	54
6.3.3	<i>Comparison with theory</i>	55
6.4	Conclusion	56
CHAPTER 7: DESIGN OF A FOIL GENERATING NEGATIVE LIFT		57
7.1	Preliminary studies of the hydrofoil	57
7.1.1	<i>Introduction</i>	57
7.1.2	<i>Geometry and set up</i>	57
7.1.3	<i>Comparison between ideal symmetrical and asymmetrical wing</i>	58
7.1.4	<i>Comparison between real asymmetrical wings</i>	62
7.1.5	<i>Influence of the foil chord</i>	66
7.1.6	<i>Influence of the distance from the sea floor</i>	68
7.1.7	<i>Conclusion</i>	71
7.2	Shape optimization on the hydrofoil	72
7.2.1	<i>Introduction</i>	72
7.2.2	<i>Geometry and set up</i>	72
7.2.3	<i>Results</i>	72
7.2.3.1	<i>Chord optimization</i>	72
7.2.3.2	<i>Distortion optimization</i>	75
7.2.4	<i>Conclusion</i>	78
CHAPTER 8: COMPARISON OF TANK TESTING AND CFD RESULTS		80
.....		
8.1	Tank testing results	80
8.1.1	<i>Introduction</i>	80
8.1.2	<i>Installation and set up</i>	80
8.1.3	<i>Results</i>	82
8.1.4	<i>Conclusion</i>	84
8.2	Complementary two dimensional CFD results	84
8.2.1	<i>Introduction</i>	84
8.2.2	<i>Geometry and set up</i>	84
8.2.3	<i>Results</i>	85
8.2.3.1	<i>Comparison between small scale sharp foils and tank testing</i>	85
8.2.3.2	<i>Full scale comparison between sharp and smooth shape</i>	87
8.2.4	<i>Conclusion</i>	89

CHAPTER 9: CONCLUSION.....	91
CHAPTER 10: FUTURE WORK	94

LIST OF FIGURES

Figure 2.1 : World energy consumption in million tonnes of oil equivalent (TOE). (Schilling & Al. 1977, IEA et Jean-Marc Jancovici).....	5
Figure 2.2 : Final energy consumption in UK in 2004 (DTI).....	6
Figure 2.3 : UK production and imports of energy in 2004 (DTI)	6
Figure 2.4 : Marine energy R&D budgets by IEA member country. (Department for Business, Innovation and Skills).....	8
Figure 2.5 : Average Annual Tidal Power around Great Britain (DTI)	9
Figure 2.6 : SeaGen horizontal axis turbine (Marine Current Turbine Ltd).....	10
Figure 2.7 : Venturi effect turbine (Lunar Energy)	10
Figure 2.8 : Oscillating hydrofoil (Stingray, Engineering Business Ltd).....	11
Figure 2.9 : Vertical axis turbine (New Energy Corporation).....	11
Figure 2.10 : Artistic impression of DeltaStream structure.	13
Figure 2.11 : Chart of Ramsey Sound and picture of St David’s point	13
Figure 2.12 : Evolution of drag produced by the frame and the 3 turbines, versus tidal current velocities at the sea surface.....	15
Figure 2.13 : Direction of the tidal current (in blue) and forces acting on the structure. Drag in red, weight in black. (Tidal Energy Ltd).....	16
Figure 3.1 : Flow regimes around a circular cylinder depending on the Reynolds number [28].....	21
Figure 3.2 : Illustration of the circulation theory of lift [40]	23
Figure 3.3 : Conformal mapping from a circulating flow around a cylinder to an aerofoil generating lift [18]	24
Figure 3.4 : Drag coefficient versus Reynolds number for a circular cylinder [35].....	25
Figure 3.5 : NACA foil parameters [18].....	27
Figure 4.1 : Surface forces acting on a fluid element in x direction [1]	31
Figure 4.2 : Control volume surface (Ansys-CFX theory guide)	38
Figure 4.3 : Process used to reach solution of the flow in Ansys CFX (Ansys-CFX theory guide)	39
Figure 5.1 : Boundary conditions	45
Figure 5.2 : Velocity profile for a depth of 35 m and a maximum velocity of 4.5 m.s^{-1}	46
Figure 6.1 : Drag coefficient for various roughness of a circular cylinder for steady flow in critical flow regime [10].	51
Figure 6.2 : Influence of a fixed boundary on the drag coefficient of a circular cylinder [10].	51
Figure 6.3 : Influence of y^+ parameter on boundary layer mesh quality	52

Figure 6.4 : Mesh sensitivity study	54
Figure 6.5 : Vortex shedding and wake at 120° for a Re of 4.10 ⁶	55
Figure 7.1 : Typical mesh used for preliminary studies on the hydrofoil.....	58
Figure 7.2 : Velocity field around the foil (A) : symmetrical foil ; (B) asymmetrical foil	59
Figure 7.3 : Lift force on a 4 cm slice of foils A and B.....	59
Figure 7.4 : Drag force on the 4 cm slice of foil A and B	60
Figure 7.5 : Pressure one a line around foils A and B	61
Figure 7.6 : Velocity field around asymmetrical foils C and D.....	63
Figure 7.7 : Pressure distribution on a line around foils C and D.....	64
Figure 7.8 : Influence of the foil length	66
Figure 7.9 : Pressure distribution on a line around foils C and E.....	67
Figure 7.10 : Influence of the distance from the sea floor for shape C	69
Figure 7.11 : Pressure distribution on a line around foils C and C2.....	70
Figure 7.12 : Profile F : thickness to chord ratio of 1/3.5. Profile G ratio of ¼	73
Figure 7.13 : Pressure distribution on a line around foils F and G	74
Figure 7.14 : Profile G : 8.4 m chord, side at 0.5m. Profile H : 8.4 m chord, side at 0.776	
Figure 7.15 : Pressure distribution on a line around foils G and H	77
Figure 8.1 : Difference between profile G (green) and profile I (red).....	81
Figure 8.2 : Small scale delta stream structure being tested in the Ifremer water tank ...	81
Figure 8.3 : Lift force (top picture) and drag force (bottom picture) measured on the structure without profile	83
Figure 8.4 : Lift force (top picture) and drag force (bottom picture) measured on the structure with profile I.....	83
Figure 8.5 : Pressure distribution on a line around foil I.....	86
Figure 8.6 : Full scale comparison between smooth (G) and sharp (I2) edges profile....	87
Figure 8.7 : Pressure distribution on a line around foils G and I2.....	88

LIST OF TABLES

Table 2.1: Drag on the frame depending on the tidal current velocity	14
Table 2.2 : Drag induced by the three turbines, depending on the tidal current velocity. 15	
Table 2.3: Necessary lift to maintain the structure at its location for different velocities and different coefficient of friction.	16
Table 6.1 : Drag and lift around a 25 m cylinder for two different boundary layers.....	53
Table 6.2: Drag and lift force for two velocities around the 25 m length cylinder	54
Table 6.3 : Drag and lift coefficient for two velocities around the cylinder.....	55
Table 7.1 : Drag and lift for the 25 m length foil A and B	60
Table 7.2: Drag and lift coefficient for foils A and B.....	60
Table 7.3: Drag and lift force for the 25 m length foil C and D	65
Table 7.4: Drag and lift coefficient for foils C and D.....	65
Table 7.5: Drag and lift for the 25 m length foil C and E.....	68
Table 7.6 : Drag and lift coefficient for foils C and E	68

Table 7.7: Drag and lift on a 25 m length shape C for different distances above the ground	71
Table 7.8: Drag and lift coefficient around foils C and C2	71
Table 7.9: Drag and Lift on a 22 m length profile of 7m chord (F) and 8.4 m chord (G)	75
Table 7.10 : Drag and lift coefficient on foils F and G.....	75
Table 7.11 : Drag and Lift of a 22m length profile. G: side at 0.5m. H: side at 0.7m.....	78
Table 7.12: Drag and lift coefficient for foils G and H	78
Table 8.1 : Drag and Lift on the structure for tank testing and CFD results in small scale.	87
Table 8.2 : Drag and Lift of a 22 m length full scale profile. G: smooth, I2: sharp.	89

ACKNOWLEDGEMENTS

I would like to thank my supervisor Dr Florent Trarieux for his guidance throughout this project. I would like to express my deepest gratitude to Dr Joao Amaral Teixeira for the time he spent in advices about CFD and for my project. I am also very grateful for his everyday happiness.

I would also thank Dr Leitia de Nagornoff, whom I shared my office with, for her good and experienced advices about work and life.

LIST OF SYMBOLS

ROMAN CHARACTERS:

A = characteristic area (2.2.2, 3.4)

\vec{a} = acceleration vector (4.1.2)

a_x = x component of acceleration (4.1.2)

B = Net mass flow out of control volume through surface S (4.1.1)

C = Time rate of decrease of mass inside control volume (4.1.1)

C_D = drag coefficient (3.4)

$C_{d\infty}$ = drag coefficient far from the wall (6.2.3)

C_f = friction coefficient (5.2.3)

C_L = lift coefficient (3.4)

C_p = power coefficient (2.2.2)

C_{ϵ_1} = adjustable constant (4.1.4)

C_{ϵ_2} = adjustable constant (4.1.4)

c_μ = adjustable constant (4.1.4)

D = characteristic length (3.2, 4.2.1, 5.2.3)

D_{est} = destruction term (4.1.4)

D_r = drag per length of unit (3.4)

e = total energy per mass unit (4.1.3)

\vec{F} = force vector (4.1.2)

F = force on full scale (8.2.3.1)

F_{drag} = drag force (3.4)

F_{lift} = lift force (3.4)

F_r = Froude number (4.2.2)

F_x = x component of force (4.1.2)

\vec{f} = body forces vector (4.1.2, 4.1.3)

f = frequency of the vortex shedding (3.2)
 f = force on small scale (8.2.3.1)
 f_x = x component of body forces (4.1.2)
 f_y = y component of body forces (4.1.2)
 f_z = z component of body forces (4.1.2)
 g = gravity acceleration (4.2.2)
 h = depth of the sea (5.3.2)
 k = turbulent kinetic energy (4.1.4)
 L_i = lift per length of unit (3.4)
 m = mass (4.1.2)
 P = production term (4.1.4)
 P_{over} = power extracted from a tidal turbine (2.2.2)
 p = pressure (4.1.2, 4.1.3)
 Q = heat (4.1.3)
 \vec{q} = rate of heat lost by thermal conduction (4.1.3)
 r = loss of heat by radiation by unit of volume (4.1.3)
 Re = Reynolds number (3.2, 4.2.1, 5.2.3)
 s = scale factor (8.2.3.1)
 S_t = Strouhal number (3.2)
 U = absolute value of the flow velocity (3.2, 4.2.1, 5.2.3, 5.3.3)
 U_∞ = maximum velocity at the sea surface (5.3.2)
 u = x component of velocity (3.4, 4.1.2, 4.1.4, 5.3.2)
 u_τ = friction velocity (5.2.3)
 \vec{V} = velocity vector in three dimensions (4.1.1, 4.1.2, 4.1.3)
 V_{tide} = fluid velocity (2.2.2)
 v = y component of velocity (4.1.2, 4.1.4)
 W = work done (4.1.3)

w = z component of velocity (4.1.2, 4.1.4)

x = x component of the z plane (3.3)

y = y component of the z plane (3.3)

y = distance of the first node from the wall (5.2.3)

$y+$ = parameter which sets the distance between the wall and the first node of the mesh (5.2.3)

z = plane after conformal mapping (3.3)

GREEK CHARACTERS:

Δd = finest mesh size (5.3.3)

Δt = timestep (5.3.3)

δ = boundary layer thickness (5.2.3)

ε = rate of dissipation of turbulent energy (4.1.4)

ϕ = velocity potential (3.3)

η = y component of the complex plane (3.3)

λ = bulk viscosity coefficient (4.1.2)

μ = molecular viscosity coefficient (4.1.2, 5.2.3)

ρ = density of sea water (2.2.2, 3.4, 4.1.1, 4.1.2, 4.1.3, 5.2.3, 8.2.3.1)

ρ_w = density of water (8.2.3.1)

σ_ε = adjustable constant (4.1.4)

σ_k = adjustable constant (4.1.4)

$\vec{\tau}$ = stress tensor (4.1.2, 4.1.3)

τ_w = average wall shear stress (5.2.3)

τ_{xx} = x component of stress on the surface of the fluid element in the yz plane (4.1.2)

τ_{yx} = x component of stress on the surface of the fluid element in the zx plane (4.1.2)

τ_{zx} = x component of stress on the surface of the fluid element in the yx plane (4.1.2)

τ_{xy} = y component of stress on the surface of the fluid element in the zy plane (4.1.2)

τ_{yy} = y component of stress on the surface of the fluid element in the zx plane (4.1.2)

τ_{zy} = y component of stress on the surface of the fluid element in the xy plane (4.1.2)

τ_{xz} = z component of stress on the surface of the fluid element in the yz plane (4.1.2)

τ_{yz} = z component of stress on the surface of the fluid element in the xz plane (4.1.2)

τ_{zz} = z component of stress on the surface of the fluid element in the xy plane (4.1.2)

ν = kinematic viscosity (4.2.1)

ν_t = kinematic turbulent viscosity (4.1.4)

ξ = x component of the complex plane (3.3)

ψ = stream function (3.3)

ζ = complex plane (3.3)

Chapter 1: Introduction

1.1 General background

Anchoring offshore devices has first been a requirement for offshore platforms, barges or FPSO in the oil and gas industry. Indeed, while operating at sea, ships and jackets need to be moored to resist wind, waves and currents. To secure such big devices to the sea bed, several types of anchorage and mooring are considered: drag embedment, clump or gravity anchors are used for vessels, depending on the nature of the soil whereas pile anchors are more effective for offshore platforms, since the pile is drilled in, it can operate in a various range of soil type [13]. All these techniques can damage life diversity settled on the sea bed and are noisy.

With the emerging market of marine renewable energy, smaller structures have to be anchored to the sea bed, and the industry tries to look for a lighter way of mooring systems. An innovative concept would be to use a hydrofoil on the structure to avoid costly and intrusive mooring requirements, or at least to reduce them. Hydrofoils are, in most cases, used to generate an upward lift and reduce drag on fast boats. In the case covered in this study, the concept is to install a reverse hydrofoil on the frame of the device, enabling the velocity of the tidal stream to interact with the hydrofoil to generate a downward lift force, in the direction of the sea floor. Hence, the structure would then be pushed onto the sea floor, and could then resist the lateral force owing to the current and of the turbines thrust. Therefore it could behave as if it was anchored, and traditional mooring systems would not be longer necessary, or would be considerably reduced. This concept is designed for the DeltaStream marine current device, a 1.2MW unit, installed on the sea bed.

The main goal of this work is to carry out a study of shape optimization on hydrofoils, to try to get a hydrofoil shape which produces the greatest lift force with site tidal stream velocities. Most of the time, shape optimization studies are performed from a prescribed pressure distribution and the design tool improves the shape to reach the prescribed pressure distribution, repeating the process until no more improvements can be made. In the case of the DeltaStream project, important constraints have to be respected, notably the hydrofoils must fit around a 2m diameter pipe, and they must be used for two symmetrical directions of incident flow, since tidal currents can be oriented to the offshore direction or to the shore direction. Hence, classical aerodynamics or hydrodynamics shapes, such as NACA profiles, cannot be used. Lift generated from bluff bodies could then be a more appropriate inspiration, but design tool optimization does not apply for shapes with such constraints.

Hence, from a simple shape meeting the criteria and respecting the constraints, studies are performed by CFD modelling. In this case, the main solution to perform a shape optimization is then to explore different parameters which affect the lift force generated by the profile. Limits of parameters variation and a combination of these parameters would produce the better shape producing as much as lift as possible and respecting the project constraints.

1.2 Scope of work

The first step of this work was to learn how the meshing software Gambit and the CFD code Ansys-CFX work. A good description of the boundary layer is important to describe viscous effects and to get an accurate result of lift generated, and so the building of a good boundary layer mesh is a first important goal to achieve. Then learning how to create a growing mesh, starting from the boundary layer with small size mesh and increasing the size mesh to boundaries of the domain is essential to get accurate results in the area of interest, without wasting computational resources. A good understanding of the physics and mathematics on which the code is based on, is also a work to perform to understand the results produced and keep a critical point of view on them. These steps are performed on a validation case basis, for which theoretical results are already known, and so a comparison between these theoretical results and results obtained from different boundary layer and global meshes can be done.

Once the first stage of coming to grips with the CFD code is performed, it is time to move forward the step of hydrofoil shape optimization. The most effective way to reach a shape which will produce enough lift force is to study quasi-2D profile, changing different parameters on each run. Hence, parameters influencing the most the quantity of lift force produced can be rearranged together to get the wanted shape. To confirm results produced in quasi-2D, a comparison with tank testing results of the structure with hydrofoils is carried out. Hence, the main goal is to know if hydrofoils can produce at least few hundred tons of downward lift. From this quantity of lift generated, setting up such hydrofoils on the structure would start to have an interest to reduce the importance of intrusive mooring.

1.3 Structure of the thesis

First of all, a summary of the current situation of energy needs and production all around the world and then in the UK is performed in Chapter two. From global policy about greenhouse gases emissions to the European Union decisions, the description then focuses on why UK decided to choose marine energy as one of its sources of renewable energy. A short presentation of different ways of harnessing the energy from tidal streams is then presented, and the DeltaStream structure studied here is presented in this context.

In Chapter three, a review of literature papers which brought significant information is presented. From history of tidal stream energy through the ages to a point of the current technology, a review of physical and mathematical concepts addressed in the thesis is then carried out. To finish this chapter, numerical methods used to design hydrofoils are shown with some highlights on experiments such as tank testing.

In Chapter four, the mathematical approach of governing equations of fluid dynamics is described, and important physical parameters used in this study are presented. Furthermore, a description of the physical phenomenon such as the flow around a circular cylinder is made.

Chapter five shows the different stages of a CFD run, from setting it up, to running it and getting results from it. It also describes the parameters used in a CFD run, such as

how to calculate the parameters defining the boundary layer, or what kind of velocity is used at the inlet boundary condition.

Chapter six presents the validation calculations: to find out the good compromise between an accurate physics representation and computational requirements, a sensitivity study on the mesh size and the boundary layer parameters are performed. T

Chapter seven presents the preliminary studies performed on the foil characteristics to find out the best influencing parameters. These parameters are then used to find the foil shape which produces the greatest downward lift force

On Chapter eight, the foil is tested at small scale in a towing tank, and unexpected results are compared to complementary CFD runs to find out an explanation. All these results are discussed and summarized in the conclusion.

Chapter 2: Energy market and tidal stream devices

2.1 Energy in the world and in UK

2.1.1 Production and consumption

Before the industrial revolution, most of energy needs were met by renewable sources, but at the end of eighteenth century, the change from an agricultural society to an industrial society was the first step to an always increasing need in more energy. Energy is needed for industries of course, but with increasing domestic comfort, the apparition of more and more electric devices for everyday tasks and the increasing use of transport, to go further and faster, the global energy demand is literally exploding years after years. Figure 2.1 shows a curve of world energy consumption with a shape close to exponential growth.

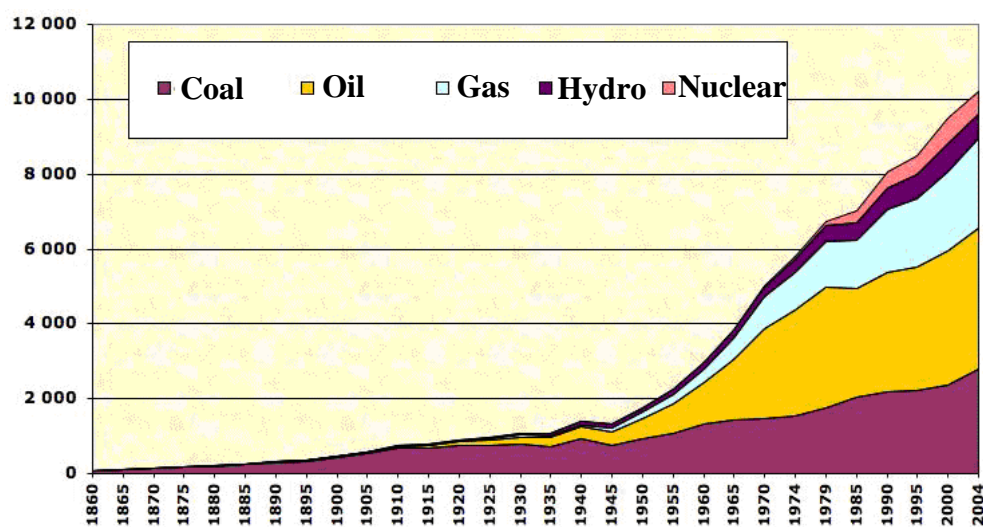


Figure 2.1 : World energy consumption in million tonnes of oil equivalent (TOE). (Schilling & Al. 1977, IEA et Jean-Marc Jancovici)

In 2004, more than 10 000 million tonnes of oil equivalent (TOE) have been consumed in the world, of which 37% of oil, 25% of coal, 23% of gas, 6% of nuclear, 4% of biomass, 3% of hydro, 0.5% of solar heat, 0.3% of wind, 0.2% geothermal, 0.2% biofuels and 0.04% of solar photovoltaic. But the consumption is not equivalent for every inhabitant of the world: in developed countries, inhabitants who represent 20% of the world inhabitants use 60% of the world energy consumption. For example, UK consumed 173.5 million tonnes of oil equivalent in 2004. As shown on Figure 2.2, 33 % of the final consumption of UK is consumed by the transport sector, 28% is consumed for domestic use and 18.5% is used for the industry.

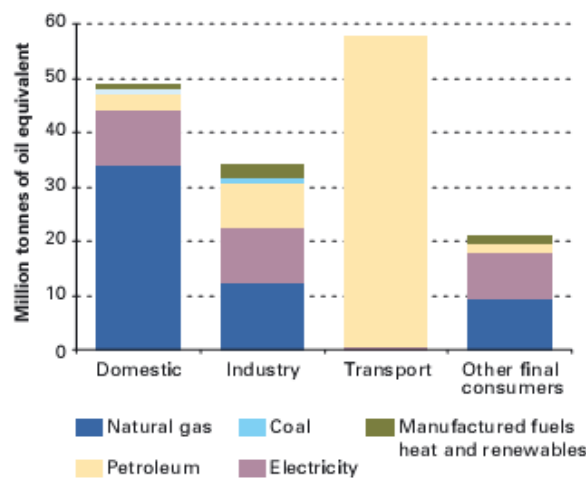


Figure 2.2 : Final energy consumption in UK in 2004 (DTI)

Like for the global energy consumption, the UK first source of energy is oil, which represents 53% of all of the energy produced and imported in the UK, 29.5% from gas and 11% from coal. The part from renewable energy seems to be negligible with only 4%, including all renewable sources together.

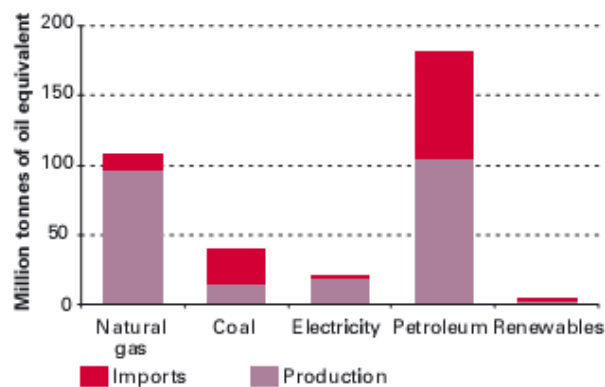


Figure 2.3 : UK production and imports of energy in 2004 (DTI)

2.1.2 Energy policy

From the 1980's, the scientific community started to research deeper on climate and on greenhouse gas emissions, and a correlation between the amount of fossil fuel combustion and global warming was highlighted. At a global scale, the policy to reduce the amount of greenhouse gases rejected into the atmosphere led to the Kyoto protocol, ratified by 172 countries, with the notable exception of the USA. This protocol requires that all countries publish the amount of greenhouse gas emitted, to establish, apply and publish national policy to reduce climate changes.

In this frame, in 2007, heads of state of the 27 member countries of the European Union agreed on the restrictive target of producing 20% of their energy by renewable sources in 2020. To reach the European target in the UK, politicians set up an innovative energy policy. The government launched a plan called "Renewable Obligation Order" to promote and plan the use of renewable energy. The "RO" places an obligation on licensed electricity suppliers to have an increasing proportion of electricity from renewable energy. This proportion is an additional percent point every year, which would enable the UK to reach the goal set by the European Union in 2020.

Hence, in July 2009, the government launched the renewable energy strategy which includes £405 million funding for renewable energy, of which 15%, representing £60 million, for marine renewable energy. This willingness of developing marine renewable energy is very specific to UK, as shown on Figure 2.4. Since 2002 and the stop of funding in marine renewable energy in Japan, UK has the potential to become a leader in marine energy systems.

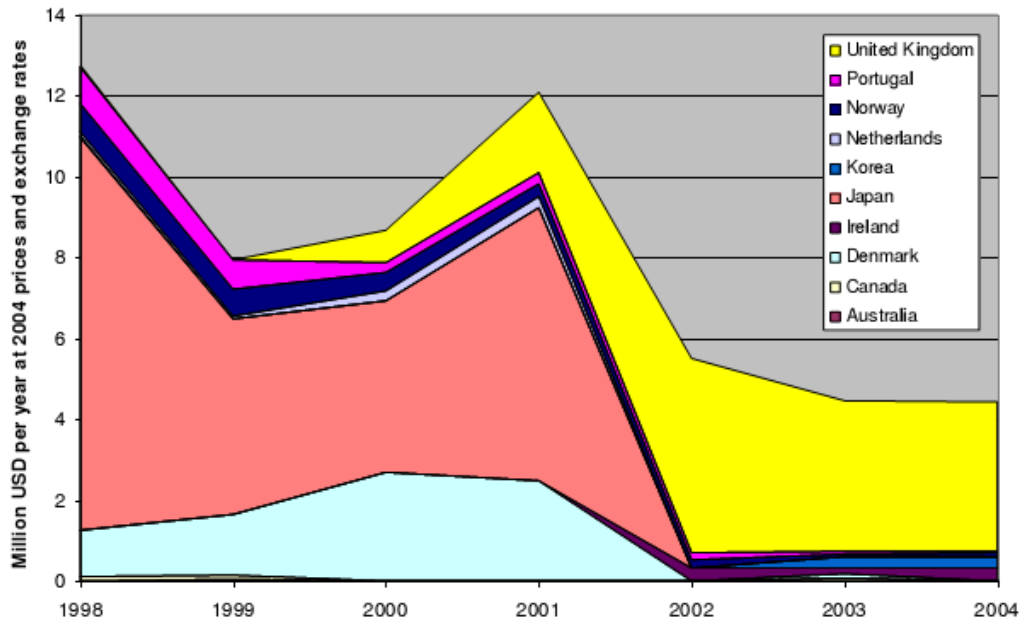


Figure 2.4 : Marine energy R&D budgets by IEA member country. (Department for Business, Innovation and Skills)

2.1.3 Marine renewable energy potential in UK

Because there is no single answer to produce renewable energy, the UK government decided to integrate marine energy as one of the sources used to produce renewable energy, between hydro-electricity, biomass energy, onshore and offshore wind power... Marine energy can provide a significant amount of UK energy needs in the future, because the geographic situation of the island is exposed to strong waves and important tidal streams, marine renewable systems explore both ways. With an electricity consumption of 350 TWh (Terra Watt hour) per year, it's estimated that marine renewable energy could provide 15 to 20% of this amount [5].

With its 5000 miles of coastline and its estuaries and peninsulas where energy focuses, Great Britain is very well exposed to tidal stream power. With gravity effects of Sun and Moon on the oceans, the rise and fall in height of the sea happen twice a day, creating fast currents where the flow is funnelled, like between islands. Furthermore, because the Sun and Moon orbits are totally predictable, tidal flow can also be predicted accurately a long time in advance, and so the amount of energy extracted can be forecast exactly.

Figure 2.5 shows the best potential sites of tidal energy, and shows that tides are amplified by bathymetric changes, estuaries and reflections by peninsulas.

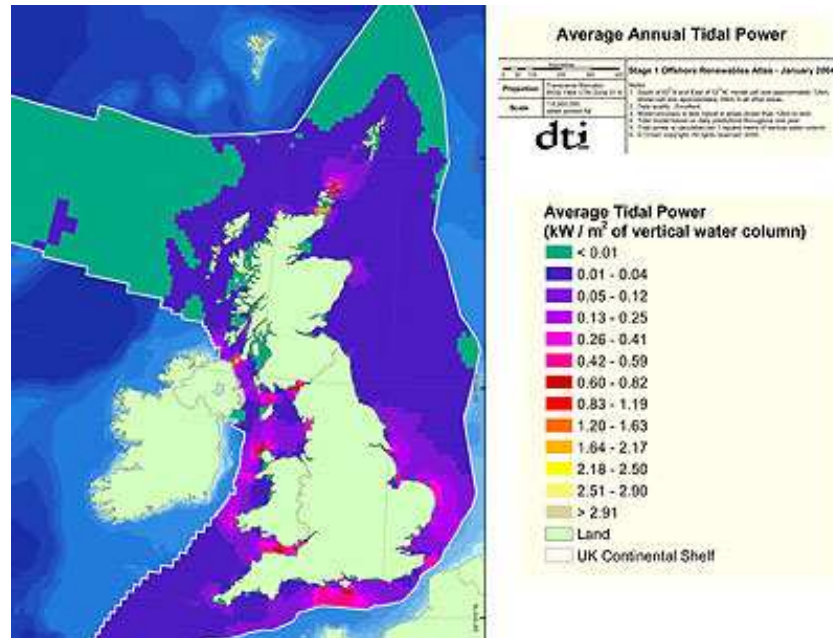


Figure 2.5 : Average Annual Tidal Power around Great Britain (DTI)

2.2 Existing tidal stream energy extraction systems

To extract tidal stream energy, devices must be made of four main parts. The first one is the feet of the device or foundation, which allows holding the blades in the tidal current. Then, the mechanical systems which can harness the flow of energy, so this part include the blades block and is called the rotor. Then there is the gearbox and the generator, allowing to the system to convert mechanical energy into electrical energy. Then the power take-off system allows connecting the device to the electrical network. Based on these main elements, different types of tidal stream devices can be listed.

2.2.1 Types of marine current turbine

2.2.1.1 Horizontal axis turbine

This type of turbine extracts energy from moving water in the same way as wind turbines extract energy from moving air. The better known example of this technology

is SeaGen, a 1.2 MW, twin turbine device operational in Strangford Lough in Northern Ireland (Figure 2.6)

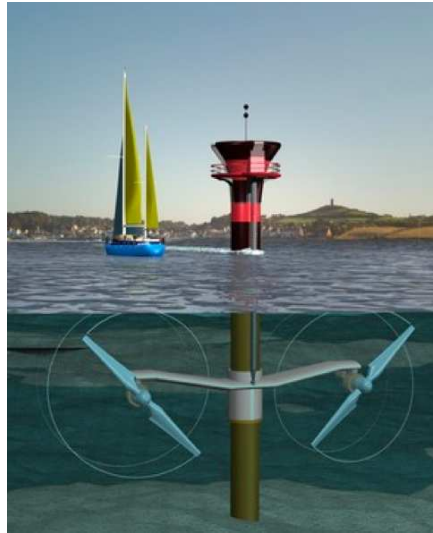


Figure 2.6 : SeaGen horizontal axis turbine (Marine Current Turbine Ltd)

2.2.1.2 Venturi Effect

By housing the device in a duct, this has the effect of concentrating the flow past the turbine. The flow of water can drive a turbine directly or the induced pressure differential in the system can drive an air-turbine. An example of this type of device is the lunar energy device (Figure 2.7)

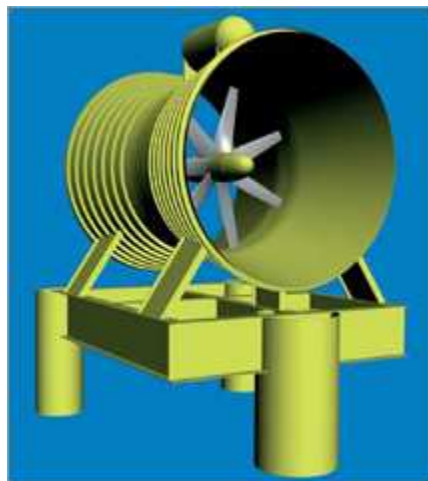


Figure 2.7 : Venturi effect turbine (Lunar Energy)

2.2.1.3 Oscillating Hydrofoil

In this device, a hydrofoil is attached to an oscillating arm and the motion is caused by the tidal current flowing either side of a wing, which results in lift. This motion can then drive fluid in a hydraulic system to be converted into electricity. The Stingray device, produced by Engineering Business Ltd is one of this type of device (Figure 2.8)

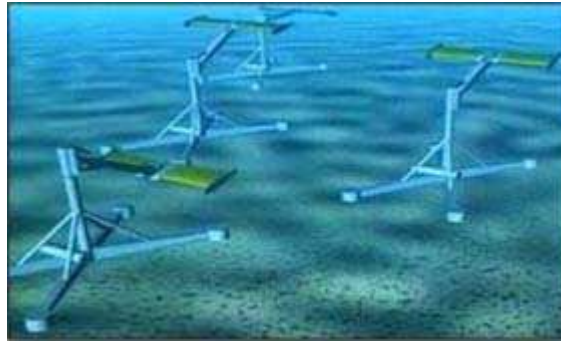


Figure 2.8 : Oscillating hydrofoil (Stingray, Engineering Business Ltd)

2.2.1.4 Vertical Axis Turbine

This technology extracts energy from moving in a similar fashion to that above, however the turbine is mounted on a vertical axis, as shown on Figure 2.9 with the device from New Energy Corporation.

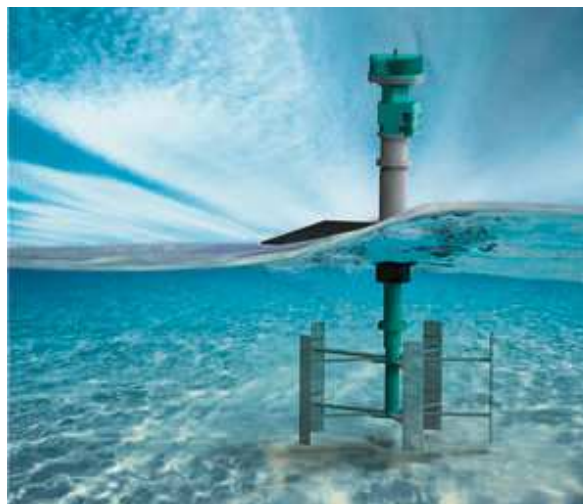


Figure 2.9 : Vertical axis turbine (New Energy Corporation)

2.2.2 Power harnessed from a tidal stream turbine

Tidal turbines have the same behaviour as wind turbine, and so the power harnessed from marine current turbines can be calculated in the same way as a wind turbine, except that the density changes. The kinetic power available to the turbine can be calculated as:

$$P_{ower} = \frac{1}{2} \rho A V_{tide}^3 \quad (2.1)$$

Where the density of the fluid is ρ , A is the area swept by the turbine and V_{tide} is the velocity of the tidal stream. However, several losses imply that the full power can not be extracted, and only a fraction of it is harnessed. So the power can now be written as :

$$P_{ower} = \frac{1}{2} \rho C_p A V_{tide}^3 \quad (2.2)$$

C_p is the power coefficient and it basically represents the percentage of power which can actually be extracted from the turbine [3]. It cannot exceed the value of 0.593, according to the Betz limit.

2.3 The DeltaStream Concept

2.3.1 The device

The DeltaStream device is a nominal 1.2MW unit which sits on the seabed without the need for a positive anchoring system. It generates electricity from three separate horizontal axis turbines mounted on a common frame (Figure 2.10). The use of three turbines on a single, circa 30 m wide, triangular frame produces a low centre of gravity enabling the device to satisfy its structural stability requirements, including the avoidance of overturning and sliding

Situated at a depth of about 35 m, the location has been chosen for its tidal stream which reaches up to 4.5 m/s in spring tides. So the name illustrates well the concept of a delta shaped structure built to make electricity from tidal stream.

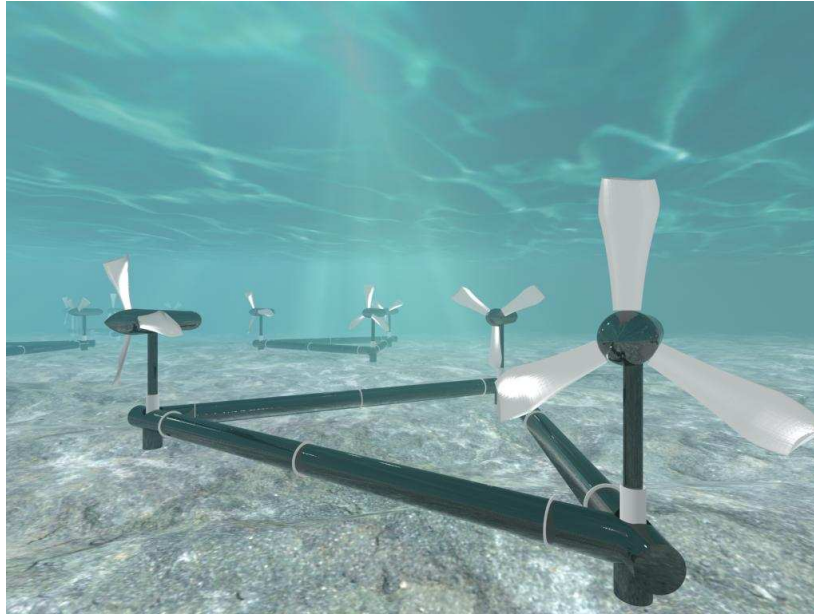


Figure 2.10 : Artistic impression of DeltaStream structure.

2.3.2 Location

DeltaStream prototype will be commissioned in Wales in Pembrokeshire between St David's point and Ramsey Island (Figure 2.11), where tidal stream can reach 4.5 m/s, but most of the time, tidal stream are more between 2 and 3 m/s.

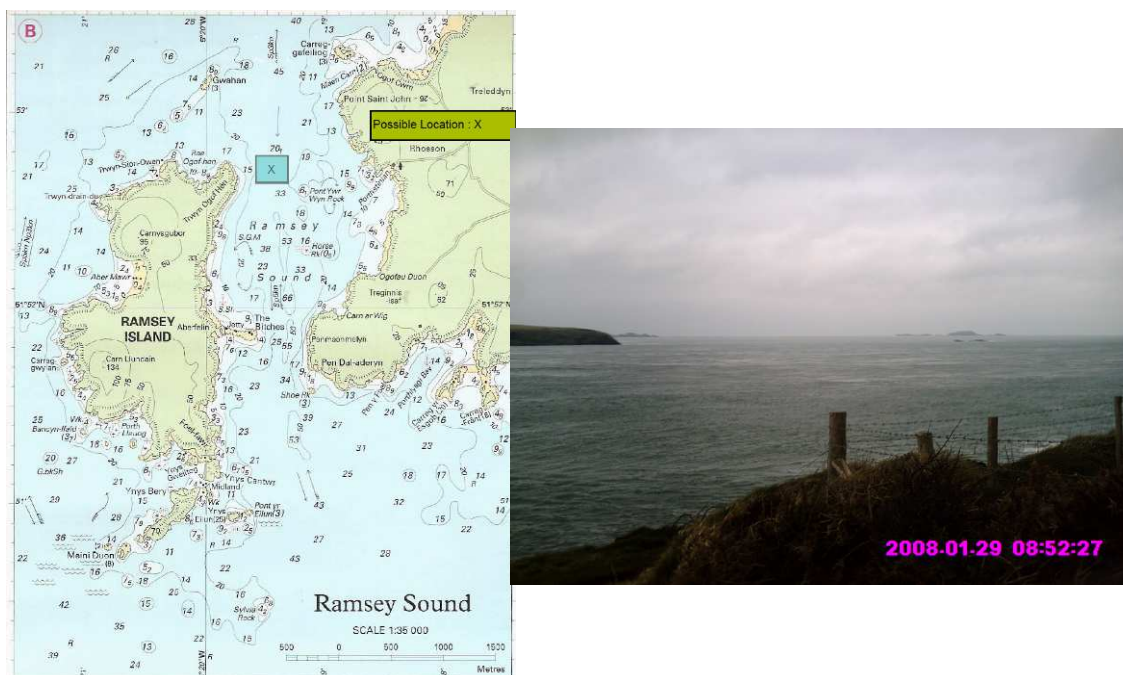


Figure 2.11 : Chart of Ramsey Sound and picture of St David's point

2.4 Rationale of the research

Because several forces will act on the device structure, if the frame is not anchored to the sea bed, the frame will move with the highest tidal currents due to the drag created by both the frame and turbines. An estimation of forces acting on the device has to be performed to know how much the anchoring system has to counteract these forces.

The device is assumed to have a weight force of some 250 tons in water. The drag produced by the frame is mostly the drag around circular pipes, and can be estimated through theoretical calculation of drag around a cylinder (§3.4 and 6.2.3) for several tidal current velocities (Table 2.1). For this study velocities between 2 and 4.5 m/s are considered, which means approximately between 4 and 9 knots. It is obvious that 9 knots is too high to be a steady tidal current velocity, but it is used here because it can represent the highest velocity peaks existing in the flow.

Velocity at surface (m/s)	Velocity at 2.5m from bottom (m/s)	Drag on the frame (Tons)
2.00	1.37	5.16
3.00	2.06	11.60
4.50	3.09	26.10

Table 2.1: Drag on the frame depending on the tidal current velocity

The drag produced by the three turbines can be roughly estimated from the Rankine-Froude actuator disk model [3]. In this method, the rotor is replaced by a circular surface of zero thickness, representative of an infinite number of blades, and to which a pressure difference is applied. From this model, the drag can be calculated as follows for steady loads:

$$F_{drag} = \frac{1}{2} \rho A (V_{tide}^2 - V_{\infty}^2) = \frac{1}{2} \rho A V_{tide}^2 [4\alpha(1-\alpha)] \quad (2.3)$$

With $\alpha = \frac{V}{V_{tide}}$

With V_{tide} the undisturbed tidal velocity and V is the velocity decrease induced by the rotor. The maximum value of α is $1/3$, and with this value, the drag induced by the three turbines of 15m diameter each can be calculated (Table 2.2).

Velocity at surface (m/s)	Velocity at 12.5m from bottom (m/s)	Drag by the 3 turbines (Tons)
2.00	1.73	71.95
3.00	2.59	161.88
4.50	3.88	364.23

Table 2.2 :Drag induced by the three turbines, depending on the tidal current velocity

Hence the drag force evolution chart, representing the drag induced by the frame and the drag induced by the three turbines can be plotted for several velocities (Figure 2.12).

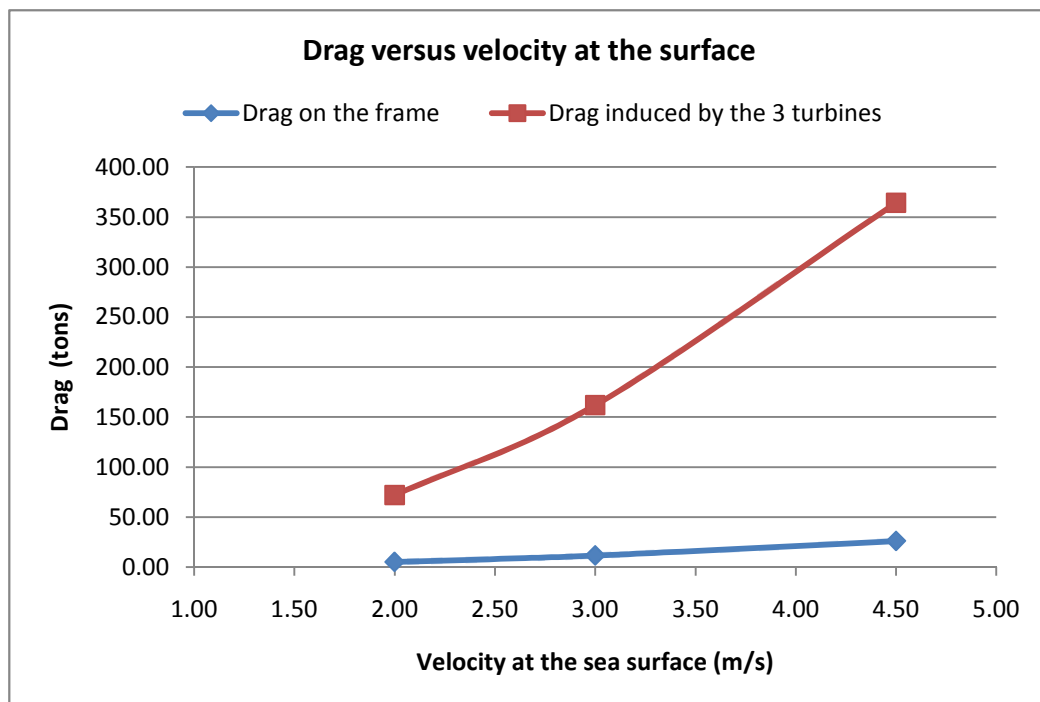


Figure 2.12 : Evolution of drag produced by the frame and the 3 turbines, versus tidal current velocities at the sea surface

When adding the drag on the frame and the drag induced by the three turbines, it is a total drag force between 77 and 390 tons, depending on the tidal current velocity (cf red

arrow on Figure 2.13). On the other hand, the friction coefficient is estimated to be between 0.45 and 0.75, with a safety factor of 1.35. So the friction coefficient is between 0.33 and 0.55 when including the safety factor, which means that with a weight of 250 tons, only a percentage between 33 and 55% is actually transmitted to the ground, which represents between 79 and 137 tons (cf black arrow on Figure 2.13). The difference between the total drag and the weight transmitted to the ground is calculated to get the lift force necessary to maintain the structure at its location (Table 2.3).

	Total drag (frame + turbines) (in tons)	Range of weight force (tons)	Necessary Lift (tons)
U = 2 m/s	77.11	79 - 137	0
U = 3 m/s	173.48	79 - 137	40 - 94
U = 4.5 m/s	390.33	79 - 137	253 - 311

Table 2.3: Necessary lift to maintain the structure at its location for different velocities and different coefficient of friction.

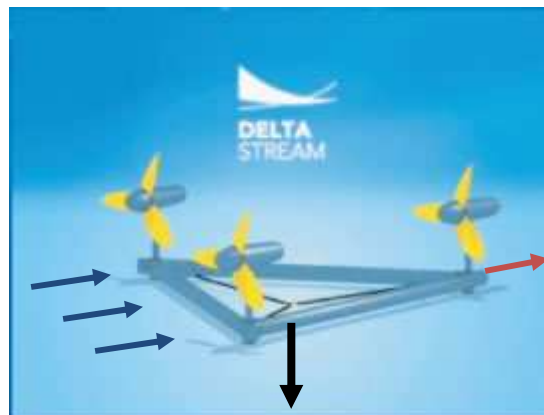


Figure 2.13 : Direction of the tidal current (in blue) and forces acting on the structure. Drag in red, weight in black. (Tidal Energy Ltd)

Therefore the structure would not need a downward lift for a velocity of 2 m/s, but to resist the highest velocity peaks of 9 knots, between 253 and 311 tons of downward lift force would have to be produced by the hydrofoils.

However this vision of the situation is too simple, because the loads considered are the main loads but additional parameters such as wave loads, or the dependence of the turbine loads versus the current velocity should be taken into account. This estimation is then a rough estimation to get an idea of the range of lift values expected to be produced.

Chapter 3: Literature review

3.1 Background

The rise and fall of the sea represents a vast and relentless phenomenon. Since the Middle Ages, tides are used to provide energy, through small tidal mills on rivers. In 1921, the idea of building a much bigger tidal barrage in La Rance in France emerged. In 1966 the construction was completed and a year later the plant was able to provide electricity to the network [5].

Because it changes the flow regime and creates an impact on the environment, the idea of using conventional tidal barrages was then progressively replaced by increasing research in hydrokinetic systems since approximately 20 years [11]. This type of small underwater and offshore systems, using the natural tidal currents, doesn't alter significantly the flow pathway, since "10% of the raw energy flux produced by the tide can be extracted without causing undue modification to the flow characteristics" [6]. Being installed offshore and underwater, they seem to have a lesser visual and environmental impact than tidal barrages. Tidal streams are mainly driven by the moon, and so it makes this potential much more predictable than wind, solar or wave energy, which conditions can only be forecasted few days or hours ago. Furthermore, these devices are quite light, and there are many potential sites across the world, as listed recently through preliminary assessments. [14][34]

However, the negative side of this kind of systems is to be exposed to rough offshore conditions like "corrosive salt water, fouling growth and abrasive suspended particles" [25] and the access for maintenance is more difficult. [38] Another point is that hydrokinetic system projects didn't get the commercial scale yet, because of the "low energy density produced, which is still between one and two orders of magnitude of the

energy produced with a same diameter turbine in a tidal barrage” [7]. Hence, the price per MW is high to match economical criteria at a commercial scale [9].

All these advantages, and the willing to minimise disadvantages are encouraging the research in hydrokinetic systems, and in this frame, seventy-six devices which can be used for tidal current and river stream have been listed in 2009 both in academia research projects and in companies [21]. They all can be ranged in two types of technology:

- Tidal current turbines (vertical or horizontal axis)
- Tidal stream generators (oscillating hydrofoil, vortex induced vibration)

The last category appeared recently, and they are more about the proof-of-concept stage whereas the first category has already the non negligible experience of wind turbines, in particular theory and methodology for tidal turbines can be widely inspired from wind turbines. [25]

Hence, the first full scale prototype to be installed in 2003 was a horizontal axis turbine from Marine Current Turbine Ltd (MCT Ltd), just followed by Hammerfest Strom. In 2008, MCT installed its 1.2 MW SeaGen tidal system in Stangford Narrows, Northern Ireland and in 2009 it became “the first-ever marine renewable energy project to be accredited by the UK energy regulator and so will receive payment for the power it is generating” [39].

3.2 Typical flow regimes around a circular cylinder

Before reaching this stage, the goal of this project is to model the flow around the horizontal pipes of the structure, to characterize the flow regime from laminar flow to turbulent wake, going through Karman vortex shedding [27]. The pipes are circular when hydrofoils are not set on them, and that’s why knowing the behaviour of the flow around cylinders can be interesting. Furthermore, the flow around a circular cylinder constitutes the validation case of CFD runs, and knowing the theory is essential to estimate CFD results.

To describe the flow around a circular cylinder, the main parameter is the Reynolds number (cf §4.2.1). A picture of different flow regimes is shown in Figure 3.1.

- For a $Re < 1$, the flow is symmetrical and the problem is laminar. There is no separation behind the cylinder.
- For $10 < Re < 40$, a steady separation behind the cylinder starts to appear. The length of this separation increases with the Reynolds number.
- For $30 < Re < 50$, downstream instabilities are added to the steady separation just behind the cylinder.
- For $50 < Re < 150$, the Karman vortex street starts to be created in the wake, and for $80-90 < Re < 150-300$ a pure periodic vortex shedding is observed, as a result of boundary layer vortices being shed alternately from either side of the cylinder.
- For a flow with a Reynolds number between 300 and $2 \cdot 10^5$, the flow is said to be subcritical, there is still a laminar separation on the cylinder and turbulent vortices are observed downstream. The wake starts at about 80° from the incoming flow direction. The frequency f of the vortex shedding can be calculated by using the Strouhal number:

$$St = 0.198 \left(1 - \frac{19.7}{Re} \right) \quad (3.1)$$

and

$$St = \frac{fD}{U} \quad (3.2)$$

- Between 2 and $6 \cdot 10^5$, the flow is said to be critical, it's the complex phenomenon of laminar separation, reattachment, and then turbulent separation which explains the important decrease of the drag coefficient curve versus the Reynolds number. The wake starts at about 120° from the incoming flow direction.
- For $6 \cdot 10^5 < Re < 3 \cdot 10^6$, the supercritical flow is characterized by a wide turbulent wake behind the cylinder and downstream.
- For $Re > 3 \cdot 10^6$, the flow is said to be transcritical, the separation on the cylinder is turbulent, and there is a turbulent wake downstream, with vortex shedding again.

The Reynolds number found in §4.2.1 shows that the flow expected would be the last one in our validation case of a circular cylinder.




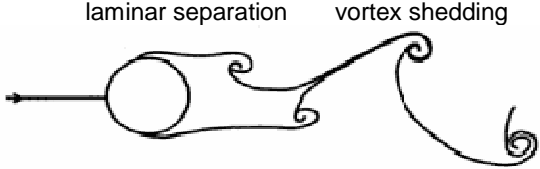
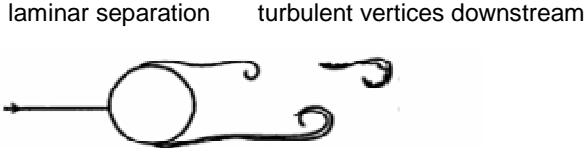
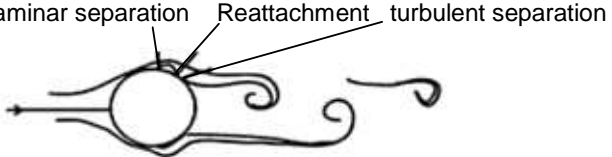
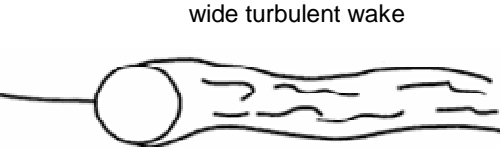
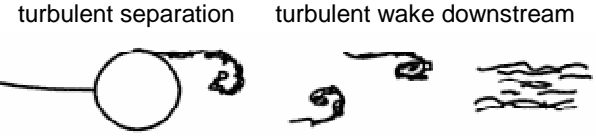
	Re < 1
	Re 10 - 40 L raises with Re
	Re 30 - 50 Downstream instabilities
	Re 50 - 150 Von Karman street vortex shedding
	Re = 300 - 2.10 ⁵ Subcritical flow
	Re = 2 - 6.10 ⁵ Critical flow
	Re = 6.10 ⁵ - 3.10 ⁶ Supercritical flow
	Re > 3.10 ⁶ Transcritical flow

Figure 3.1 : Flow regimes around a circular cylinder depending on the Reynolds number [28]

A lift force on a circular cylinder can occur in the following circumstances which are outside the scope of this thesis:

- Asymmetrical cross-section:

Lift and drag forces and torsional moment on slender structures with asymmetrical cross-section (relative to the flow direction) can lead to large amplitude galloping and flutter [4]

- Wake effects:

The velocity field in the wake of one or several cylinders is non-uniform. Position dependent lift and drag forces on a cylinder in the wake may lead to wake induced oscillations.

- Wall effects:

The asymmetrical flow past a cylinder close to a wall gives rise to a non-zero lift force. A narrow gap between the cylinder and the wall leads to increased velocity and reduced pressure in the gap with a resulting lift force acting towards the wall.

- Vortex shedding.

The lift force due to vortex shedding oscillates with the Strouhal frequency.

3.3 Theory of lift

Once the study of the circular cylinder is done, the horizontal pipes with hydrofoils set on them are studied. To understand how the hydrofoils will produce a downward lift to replace a traditional mooring system, the theory of lift is summarized. The generation of lift is associated with the circulation, and this concept needs to be explained. The circulation concept means that the flow has a component of rotation. Indeed when the flow arrives on the hydrofoil, the shape of the hydrofoil deviates the flow and creates a circulation. The circulating flows can be resolved as a uniform irrotational part and a circulating part, and it implies the existence of vorticity when there is circulation in a flow [18].

A fluid flow can hence be represented with parallel streamlines added to circulation around a wing. On the suction side of the wing, this circulation is in the same direction as the undisturbed air flow, and in this area, the undisturbed air flow and the circulation

are added one to the other. On the pressure side of the wing, the circulation is in the opposite direction of the undisturbed air flow, and so the circulation is subtracted to the undisturbed air flow.

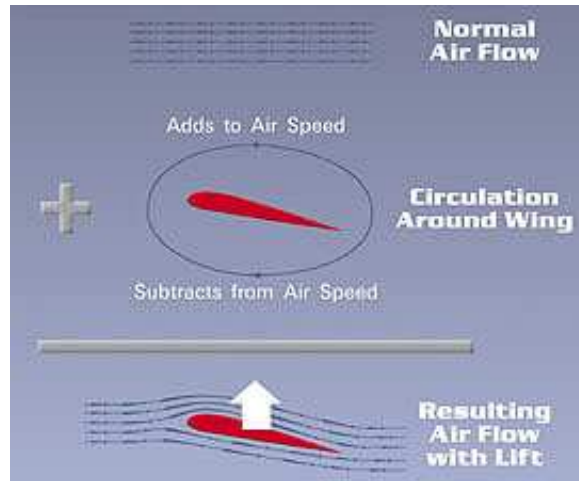


Figure 3.2 : Illustration of the circulation theory of lift [40]

This difference of the circulation between the suction side and the pressure side of the wing creates a difference of fluid velocity between the two sides of the wing: the velocity is higher on the suction side than on the pressure one. Hence, the difference between the lower pressure on the suction side of the wing and the higher pressure on the pressure side, results in an upward lift force [40].

It's on this idea that Zhukovsky bases the first successful aerofoil theory. From a complex plane $\zeta = \xi + i\eta$ where a circle is plotted, a conformal transformation makes an aerofoil in the $z = x + iy$ plane. Indeed, in the ζ plane and using potential flow theory, a spinning cylinder in a uniform flow can be described by ψ , the stream function, as a combination of doublet (a source and a sink), a uniform horizontal flow and a line vortex. In the z plane, the spinning cylinder is mapped to a lifting aerofoil. Then when ϕ is the velocity potential and ψ is the stream function, the potential flow can be represented in a complex definition by $\Phi = \phi + i\psi$. The conformal transformation applied by Zhukovsky can be expressed as:

$$z = \zeta + \frac{C^2}{\zeta}$$

Where C is a parameter, and this transformation is used to map the complex potential flow from the ζ plane to the z plane, allowing the flow around the circle in the ζ plane to represent the flow around the aerofoil in the z plane.

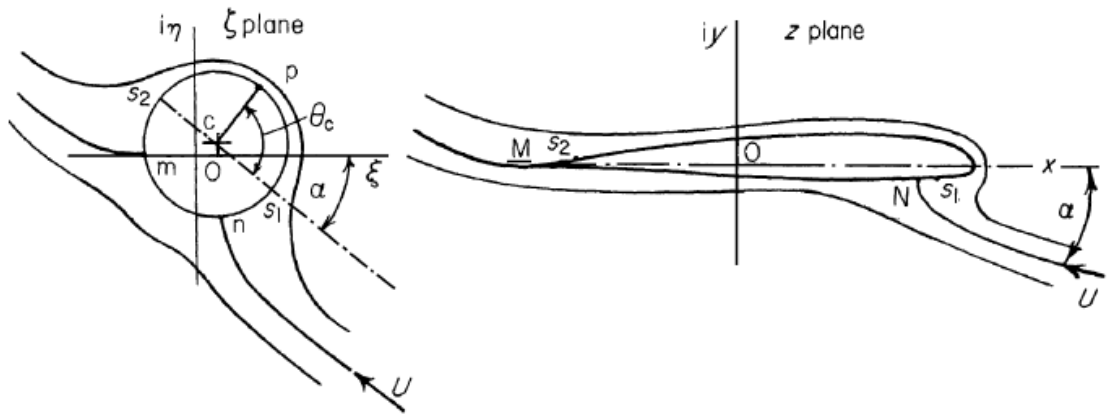


Figure 3.3 : Conformal mapping from a circulating flow around a cylinder to an aerofoil generating lift [18]

Hence, results of the flow around a circle with circulation can be used for the knowledge of the flow around an aerofoil. Through this transformation, the Kutta condition must be respected: it means that the magnitude of circulation must be chosen in order to have the rear stagnation point on the trailing edge of the wing. So when the Kutta condition is respected, only one value of circulation exists for an aerofoil at an angle of attack.

3.4 Drag and lift coefficients

Now that the principle of lift is understood, it is shown that by fitting a hydrofoil to the pipe, the down-force is greater than the drag, so that the structure could stay in its location by an inverted lift effect. To show this, using drag and lift coefficients are necessary, and the lift coefficient is first explained. Theoretical lift coefficient can be calculated analytically, depending on the roughness of the cylinder and the Reynolds number, as shown by Hoerner [16]. The lift force can be calculated as follows:

$$F_{lift} = \frac{1}{2} \rho A C_L u^2(y) \quad (3.3)$$

Where ρ is the density of sea water $\rho = 1025 \text{ kg.m}^3$

A is the characteristic area in m^2 , which means the projected area. In the case of a cylinder, A is equal to the diameter of the cylinder multiplied by its length.

C_L is the lift coefficient.

For the drag around a slice of pipe, it can be calculated the same way as the lift force, using the drag coefficient C_D and the velocity $u(y)$:

$$F_{drag} = \frac{1}{2} \rho A C_D u^2(y) \quad (3.4)$$

And so the drag coefficient can be defined as:

$$C_D = \frac{F_{drag}}{\frac{1}{2} \rho u^2 A} \quad (3.5)$$

The shape of the drag coefficient versus the Reynolds number has been explained by Tritton (1977) [35]. Indeed, as can be seen on Figure 3.4, three different parts in the shape of the curve can be observed.

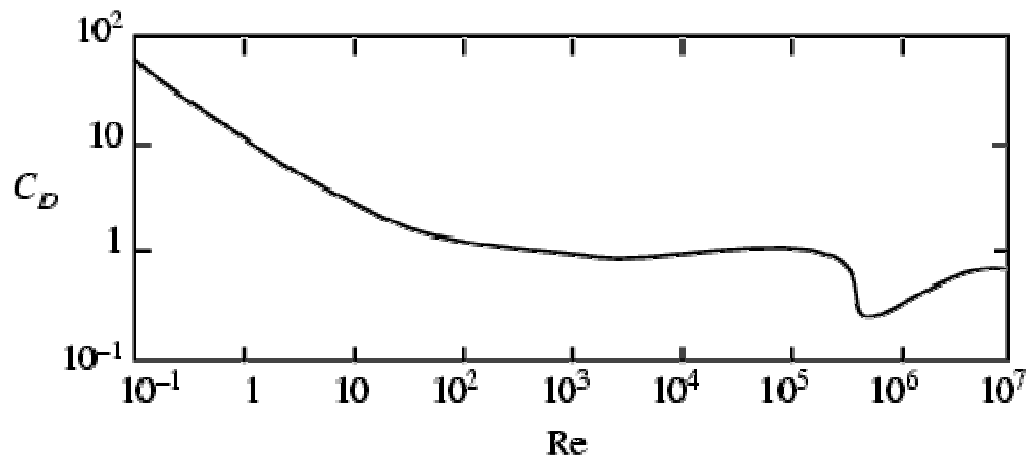


Figure 3.4 : Drag coefficient versus Reynolds number for a circular cylinder [35]

The first part of the curve is for Re between 10^{-1} and 10^2 , and for these low Reynolds number, the drag coefficient approximation is :

$$C_D \propto \frac{1}{Re} \quad (3.6)$$

It means that the drag is proportional to the speed at low Reynolds numbers and hence this part of the curve is a straight line.

The second part of the curve is for Re between 10^2 and 3.10^5 , the drag coefficient doesn't vary much and the drag is proportional to the square velocity: $F_{drag} \propto u_0^2$, so the drag coefficient is almost constant.

The last part of the curve is for Re greater than 3.10^5 . On this part of the curve a drop happens at $Re \approx 3.10^5$, and the drag decreases while the speed increases. This can be explained by the boundary layer which starts to be turbulent, and implies a transitional phenomenon of separation and reattachment of the boundary layer on the cylinder (cf

Figure 3.1). The separation makes a drop of pressure behind the cylinder, and the difference of pressure between the front and the rear of the cylinder creates a drag which counteracts the viscous drag, hence decreasing the total drag. For $Re \geq 3.10^6$ the fully turbulent separation of the boundary layer generates a bigger wake, the pressure drag decreases, and the total drag increases again, causing the increase of the drag coefficient. However, because of the proximity of the structure under study to the ground, the drag coefficient corresponding to the Reynolds number of the flow should be adjusted according to "Recommended Practice" from DNV [10] and as shown in paragraph 6.2.3.

Estimating the drag around a circular cylinder is only the first part of the model, and the comparison between theoretical and CFD results constitutes a validation case. To decrease the drag and increase the lift, a profile, usually known as hydrofoil or aerofoil and characterized by a high lift-to-drag ratio should be used [15]. The lift to drag ratio is a dimensionless parameter, which allows comparing efficiency of different foils. It represents the amount of lift generated by the foil, divided by the drag when fluid flows past the foil. It is written as L_i/D_r . In the case being examined, the lift to drag ratio target is not exactly defined, the goal is to get as most negative lift force as possible.

3.5 Hydrofoil shape

Hydrofoils are mainly used in fast boats. The lift created allows the ship to plane, such that the hull drag is significantly reduced, meaning that the craft velocity can be highly increased. That is why papers in literature are mostly oriented to simulation of hydrofoils near the free surface, and no paper has been found about hydrofoil far from

the surface. As a downward lift needs to be produced, the generation of high pressure on the top face and low pressure on the bottom face of the hydrofoil results in a downward lift force [8].

Since to produce lift, a foil should have either an asymmetrical shape or be inclined to the flow direction, or both [35], foil design usually starts from a NACA profile. NACA means National Advisory Committee on Aeronautics and was the organization which preceded NASA. Parameters of drag and lift coefficient for several types of NACA profiles are described by Hoerner [17]. A NACA profile is characterized by four digits, one describes the maximum camber as percentage of the chord, one describes the distance from the leading edge of the maximum camber (in tens of percent of the chord) and two digits describe the maximum thickness of the foil as percent of the chord [20].

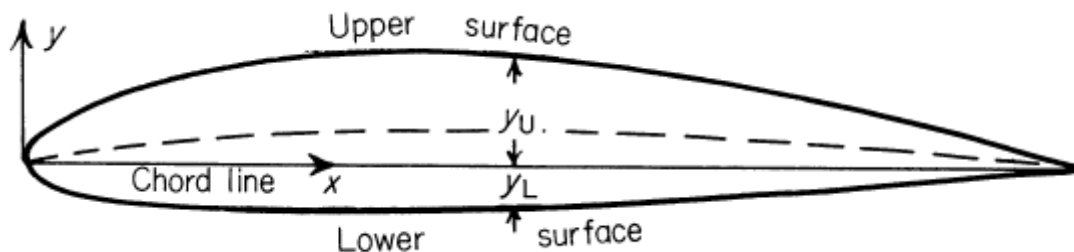


Figure 3.5 : NACA foil parameters [18]

However, several constraints have to be respected in the foil design process. Geometrical constraints are the two meters diameter horizontal pipes around which the foil has to fit. This constraint imposes a huge maximum thickness of the foil. Furthermore, the foil has to be symmetrical to the y axis, since the tidal flow can be either in the +x or -x axis direction. This constraint is very important, since it imposes not to use a NACA profile, which can not meet this criterion. This constraint also prevents the introduction of an angle of attack between the flow and the foil. But the asymmetrical aspect of NACA airfoils to the x axis can be a source of inspiration to design a downward lifting foil for the DeltaStream structure. From this basis, numerical studies are performed to get more information about the lift produced by the designed shape.

3.6 Numerical methods

To design a hydrofoil, several numerical methods exist: codes based on the Newton-Raphson method can produce foil geometry from a prescribed pressure distribution, following physical constraints like the presence of a stagnation point [19]. The geometry can then be tested with panel methods codes, based on Zhukovsky's theory of conformal transformation (cf §3.3). They are light numerical codes, using doublets, uniform flow and vortices distribution around the hydrofoil surface to model the flow around it. Lift and drag coefficients can be calculated from this method [41]. One of the most used panel method code is Xfoil, which is an open source code, developed originally for airfoils. The last tool which can be used is Computational Fluid Dynamics (CFD), which resolves the Reynolds Averaged Navier-Stokes (RANS) equations [36] and hence, is more accurate than other methods. Indeed, for the particular case of hydrofoils, results from CFD and from experiments reach a reasonable agreement, and the force exerted by the flow on the structure can be calculated directly with CFD [23]. For example, hydrofoils used on America's cup boats are modelled in CFD [32].

Even if numerical methods are nowadays very trustable, wind tunnel experiments or towing tank experiments are still widely used. In this study, numerical studies have been used as a tool for preliminary studies on foil design. These results are then compared with tank testing results. However, the usage of appropriate model laws has to be undertaken to trust tank testing results. The scaling laws of similitude technique are based on the conservation of dimensionless parameters such as Froude number (cf §4.2.2) for hydrodynamic testing driven by gravity. However, the conservation of both Froude and Reynolds law simultaneously is not possible [30]. Hence, when the Froude similitude is chosen, the Reynolds number for the prototype is lower than at the real scale, and thus drag and lift coefficient can be misestimated.

Being aware of the limitations of CFD results, it appears that tank testing does not always reflect what happens at a biggest scale, and so final CFD runs are performed to compare two different foil shapes both at full and prototype scale in CFD. Small scale results are then compared with tank testing results.

Chapter 4: Mathematical approach

4.1 Governing equations of fluid dynamics

4.1.1 Mass conservation

A finite control volume V is defined by a surface control S and fixed in space. In this control volume there is another elemental volume δV defined by a elemental surface control δS . The velocity perpendicular to the surface is \vec{V} . When the mass conservation principle is applied to these volumes, it means:

$$\left\{ \begin{array}{l} \text{Net mass flow out of} \\ \text{control volume} \\ \text{through surface S} \end{array} \right\} = \left\{ \begin{array}{l} \text{Time rate of} \\ \text{decrease of mass} \\ \text{inside control} \\ \text{volume} \end{array} \right\}$$

Which can be written as:

$$B = C \quad (4.1)$$

The net mass flow rate out of control volume through surface S , named B in the previous equation can be expressed as :

$$B = \oiint_S \rho \vec{V} \cdot \vec{dS} \quad (4.2)$$

And in the elemental volume δV the mass is $\rho \delta V$ and when integrated on the whole volume, the total mass is :

$$\iiint_V \rho dV \quad (4.3)$$

In volume V , the time rate of decrease of mass, called C in Equation (4.1), is then:

$$C = -\frac{\partial}{\partial t} \iiint_v \rho dV \quad (4.4)$$

Then from Equation 4.1, it becomes:

$$\oiint_S \rho \vec{V} \cdot \vec{dS} = -\frac{\partial}{\partial t} \iiint_v \rho dV \quad (4.5)$$

Or,

$$\boxed{\frac{\partial}{\partial t} \iiint_v \rho dV + \oiint_S \rho \vec{V} \cdot \vec{dS} = 0} \quad (4.6)$$

Equation 4.6 is the integral form of the continuity equation. It can be transformed if the divergence theorem is applied :

$$\oiint_S (\rho \vec{V}) \cdot \vec{dS} = \iiint_v \nabla \cdot (\rho \vec{V}) dV \quad (4.7)$$

So by replacing Equation 4.7 in Equation 4.6, and because the control volume is fixed in space, integration limits are constant and the derivative sign can be moved under the integral in Equation 4.6:

$$\iiint_v \frac{\partial \rho}{\partial t} dV + \iiint_v \nabla \cdot (\rho \vec{V}) dV = 0 \quad (4.8)$$

Or

$$\iiint_v \left[\frac{\partial \rho}{\partial t} dV + \nabla \cdot (\rho \vec{V}) \right] dV = 0 \quad (4.9)$$

Because the volume control is chosen arbitrarily in space, the only way to have Equation 4.9 equal to zero is the integrand should be equal to zero in each point of the volume control, it means:

$$\boxed{\frac{\partial \rho}{\partial t} dV + \nabla \cdot (\rho \vec{V}) = 0} \quad (4.10)$$

Equation 4.10 is the continuity equation in the conservation form. After applying a model of volume control and surface control, the integral form (Equation 4.6) is obtained directly. After few mathematical manipulations, the differential Equation 4.10 is obtained.

4.1.2 The momentum equation

In this section, the fundamental Newton's second law is applied to a flow. The physical principle of Newton's second law being $\vec{F} = m\vec{a}$

If the x component of Newton's second law is considered, it is written:

$$F_x = ma_x \quad (4.11)$$

Where F_x is the scalar x-component of the force and a_x of the acceleration. Forces can be either:

- Body forces: they are acting on the mass of the volume control, it can be for example gravity. They can be written as:

$$\{Bodyforces\} = \rho f_x (dxdydz) \quad (4.12)$$

- Surface forces: they are acting on the surface control and can only be: the pressure distribution around the volume and the shear and normal stress created by the surrounding fluid.

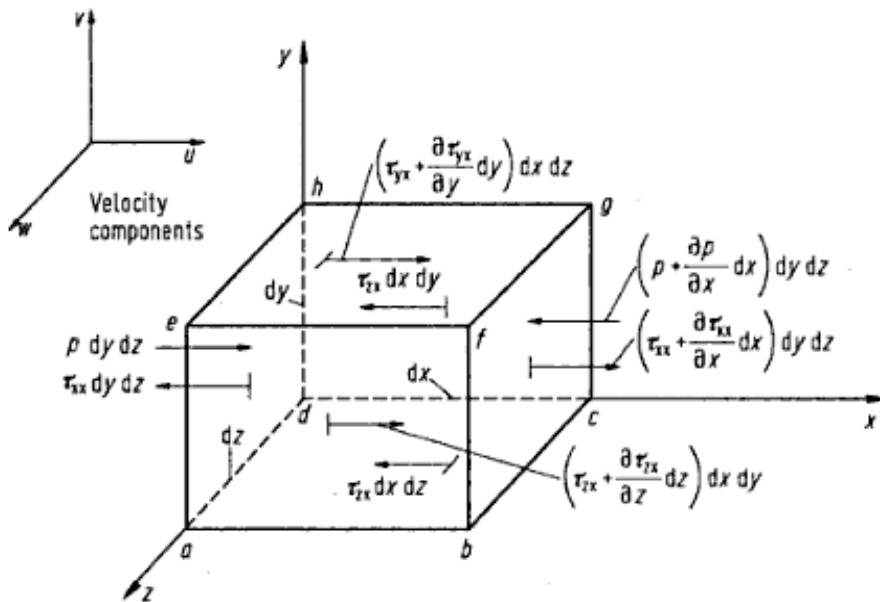


Figure 4.1 : Surface forces acting on a fluid element in x direction [1]

Hence, surface forces acting in the x direction are summarized:

$$\{Surfaceforce\} = \left[p - \left(p + \frac{\partial p}{\partial x} dx \right) \right] dydz + \left[\left(\tau_{xx} + \frac{\partial \tau_{xx}}{\partial x} dx \right) - \tau_{xx} \right] dydz$$

$$+ \left[\left(\tau_{yx} + \frac{\partial \tau_{yx}}{\partial y} dy \right) - \tau_{yx} \right] dx dz + \left[\left(\tau_{zx} + \frac{\partial \tau_{zx}}{\partial z} dz \right) - \tau_{zx} \right] dx dy \quad (4.13)$$

So in the x-direction, F_x is the sum of equations 4.12 and 4.13:

$$F_x = \left(-\frac{\partial p}{\partial x} + \frac{\partial \tau_{xx}}{\partial x} + \frac{\partial \tau_{yx}}{\partial y} + \frac{\partial \tau_{zx}}{\partial z} \right) dx dy dz + \rho f_x dx dy dz \quad (4.14)$$

When the right part of Equation 4.11 is considered, the mass can be calculated as:

$$m = \rho dx dy dz \quad (4.15)$$

And the acceleration is:

$$a_x = \frac{Du}{Dt} \quad (4.16)$$

So from equations 4.14, 4.15 and 4.16, it becomes :

$$\rho \frac{Du}{Dt} = -\frac{\partial p}{\partial x} + \frac{\partial \tau_{xx}}{\partial x} + \frac{\partial \tau_{yx}}{\partial y} + \frac{\partial \tau_{zx}}{\partial z} + \rho f_x \quad (4.17)$$

This is the component in the x direction for the momentum equations in viscous flows.

So y and z components can be written as:

$$\rho \frac{Dv}{Dt} = -\frac{\partial p}{\partial y} + \frac{\partial \tau_{xy}}{\partial x} + \frac{\partial \tau_{yy}}{\partial y} + \frac{\partial \tau_{zy}}{\partial z} + \rho f_y \quad (4.18)$$

$$\rho \frac{Dw}{Dt} = -\frac{\partial p}{\partial z} + \frac{\partial \tau_{xz}}{\partial x} + \frac{\partial \tau_{yz}}{\partial y} + \frac{\partial \tau_{zz}}{\partial z} + \rho f_z \quad (4.19)$$

Equations 4.17, 4.18 and 4.19 are differential equations of the momentum equations, obtained directly from Newton's second law. These equations have been discovered by M. Navier and G.Stokes in the beginning of nineteenth century and they now have the name of Navier-Stokes equations. They can also be written as a conservation form:

$$\rho \frac{Du}{Dt} = \rho \frac{\partial u}{\partial t} + \rho \vec{V} \cdot \nabla u \quad (4.20)$$

And

$$\frac{\partial(\rho u)}{\partial t} = \rho \frac{\partial u}{\partial t} + u \frac{\partial \rho}{\partial t} \quad (4.21)$$

And

$$\nabla \cdot (\rho u \vec{V}) = u \nabla \cdot (\rho \vec{V}) + (\rho \vec{V}) \cdot \nabla u \quad (4.22)$$

So

$$\rho \frac{Du}{Dt} = \frac{\partial(\rho u)}{\partial t} - u \frac{\partial \rho}{\partial t} - u \nabla \cdot (\rho \vec{V}) + \nabla \cdot (\rho u \vec{V}) \quad (4.23)$$

$$\rho \frac{Du}{Dt} = \frac{\partial(\rho u)}{\partial t} - u \left[\frac{\partial \rho}{\partial t} - \nabla \cdot (\rho \vec{V}) \right] + \nabla \cdot (\rho u \vec{V}) \quad (4.24)$$

And according to the continuity equation, the expression in brackets is equal to zero.

And the Navier-Stokes equations can be written as:

$$\boxed{\frac{\partial(\rho u)}{\partial t} + \nabla \cdot (\rho u \vec{V}) = -\frac{\partial p}{\partial x} + \frac{\partial \tau_{xx}}{\partial x} + \frac{\partial \tau_{yx}}{\partial y} + \frac{\partial \tau_{zx}}{\partial z} + \rho f_x} \quad (4.25)$$

$$\boxed{\frac{\partial(\rho v)}{\partial t} + \nabla \cdot (\rho v \vec{V}) = -\frac{\partial p}{\partial y} + \frac{\partial \tau_{xy}}{\partial x} + \frac{\partial \tau_{yy}}{\partial y} + \frac{\partial \tau_{zy}}{\partial z} + \rho f_y} \quad (4.26)$$

$$\boxed{\frac{\partial(\rho w)}{\partial t} + \nabla \cdot (\rho w \vec{V}) = -\frac{\partial p}{\partial z} + \frac{\partial \tau_{xz}}{\partial x} + \frac{\partial \tau_{yz}}{\partial y} + \frac{\partial \tau_{zz}}{\partial z} + \rho f_z} \quad (4.27)$$

The components of shear and normal stress can be written as follows:

$$\tau_{xx} = \lambda \nabla \cdot \vec{V} + 2\mu \frac{\partial u}{\partial x} \quad (4.28)$$

$$\tau_{yy} = \lambda \nabla \cdot \vec{V} + 2\mu \frac{\partial v}{\partial y} \quad (4.29)$$

$$\tau_{zz} = \lambda \nabla \cdot \vec{V} + 2\mu \frac{\partial w}{\partial z} \quad (4.30)$$

$$\tau_{xy} = \tau_{yx} = \mu \left(\frac{\partial v}{\partial x} + \frac{\partial u}{\partial y} \right) \quad (4.31)$$

$$\tau_{xz} = \tau_{zx} = \mu \left(\frac{\partial u}{\partial z} + \frac{\partial w}{\partial x} \right) \quad (4.32)$$

$$\tau_{yz} = \tau_{zy} = \mu \left(\frac{\partial w}{\partial y} + \frac{\partial v}{\partial z} \right) \quad (4.33)$$

With μ the molecular viscosity coefficient and λ the bulk viscosity coefficient, with

$$\lambda = -\frac{2}{3}\mu \text{ often used.}$$

In a vectorial form, Navier-Stokes equations can also be written as:

$$\boxed{\frac{\partial(\rho\bar{V})}{\partial t} + \nabla \cdot (\rho\bar{V} \otimes \bar{V}) = -\nabla p + \nabla \cdot \bar{\tau} + \rho\bar{f}} \quad (4.34)$$

Where p is the pressure, $\bar{\tau}$ is the stress tensor and \bar{f} represents body forces.

The terms of these equations represents the influence of local acceleration, advection, pressure gradient and viscous effect, and body forces such as gravity, which influence the trajectory of water particles.

4.1.3 The energy equation

The energy equation is based of the physical principle that energy is conserved.

This equation comes from the first law of thermodynamics:

$$\text{Time rate of change of energy} = \text{Net rate of heat added} \left(\sum \dot{Q} \right) + \text{Net rate of work done}$$

Which leads to:

$$\frac{\partial(\rho e)}{\partial t} + \nabla \cdot [(\rho e + p)\bar{V}] = \nabla \cdot (\bar{\tau} \cdot \bar{V}) + \rho \bar{f} \cdot \bar{V} - \nabla \cdot \bar{q} + r \quad (4.35)$$

With e the total energy per mass unit, \bar{q} the rate of heat lost by thermal conduction, r is the lost of heat by radiation by unit of volume.

Physically, this equation defines the rate of temperature change of a fluid element because of the local acceleration derivative and the advection derivative.

4.1.4 Turbulence equation

All flows are totally described by the continuity, momentum, and energy equations described above, and they can be resolved analytically in some simple cases. However,

industrial or practical flows have to be resolved numerically by CFD methods. Small disturbances can appear because of the fluid motion or induced by the surface roughness, where they will be amplified in the direction of the flow. That is what happens for a circular cylinder at high Reynolds numbers, when inertia forces are much more important than viscous effects. Small disturbances are then amplified and the turbulence starts to occur, which means that random fluctuations are existing in the fluid. One of the parameters fluctuating can be the velocity, which can be represented versus time as a mean velocity \bar{u} , and from there, turbulent fluctuations u' are oscillating around this mean value. Hence, this principle of formulating variables as the sum of the mean value and turbulent fluctuations can be applied to the equation of continuity and to the conservative form of momentum and energy equation [36]. For example, the momentum equation can be written as the sum of time averaged equation and additional terms known as Reynolds stresses and made of fluctuating components. This can be seen on Equation 4.36, written for the x component.

$$\rho \frac{\partial \bar{U}}{\partial t} + \rho \bar{U} \frac{\partial \bar{U}}{\partial x} + \rho \bar{V} \frac{\partial \bar{U}}{\partial y} = -\frac{\partial p}{\partial x} + \frac{\partial}{\partial x} \left(\mu \frac{\partial \bar{U}}{\partial x} \right) + \frac{\partial}{\partial y} \left(\mu \frac{\partial \bar{U}}{\partial y} \right) - \rho \frac{\partial \overline{u'^2}}{\partial x} - \rho \frac{\partial \overline{(u'v')}}{\partial y} \quad (4.36)$$

The time averaged equation is the same as the original momentum equation but with time averaged velocities. To take account of turbulence effects, the two additional terms on the right of the equation, called Reynolds stresses, are modelled. They are treated as additional viscous stresses, and hence Equation 4.36 can be written as:

$$\rho \frac{\partial \bar{U}}{\partial t} + \rho \bar{U} \frac{\partial \bar{U}}{\partial x} + \rho \bar{V} \frac{\partial \bar{U}}{\partial y} = -\frac{\partial p}{\partial x} + \frac{\partial}{\partial x} \left((\mu + \mu_T) \frac{\partial \bar{U}}{\partial x} \right) + \frac{\partial}{\partial y} \left((\mu + \mu_T) \frac{\partial \bar{U}}{\partial y} \right) \quad (4.37)$$

The instantaneous components are replaced by the mean velocity components and an additional turbulent viscosity is added to the viscosity, due to the turbulence of the flow. To complete the turbulence modelling, the turbulent viscosity can be found from the other flow variables [33].

That is why two differential transport equations are added to the system. These equations are similar to the momentum equations and describe the distribution of turbulent kinetic energy k and the distribution of the dissipation rate of k called ε . k is defined as:

$$k = \frac{1}{2}(u'^2 + v'^2) \quad (4.38)$$

These equations means that the rate of change and the advection transport of the turbulent kinetic energy k or the rate of dissipation of turbulent energy ε equals the diffusion transport combined with the rate of production and destruction of k or ε .

$$\frac{\partial k}{\partial t} + \frac{\partial(uk)}{\partial x} + \frac{\partial(vk)}{\partial y} + \frac{\partial(wk)}{\partial z} = \frac{\partial}{\partial x} \left[\frac{\nu_T}{\sigma_k} \frac{\partial k}{\partial x} \right] + \frac{\partial}{\partial y} \left[\frac{\nu_T}{\sigma_k} \frac{\partial k}{\partial y} \right] + \frac{\partial}{\partial z} \left[\frac{\nu_T}{\sigma_k} \frac{\partial k}{\partial z} \right] + P - D_{est} \quad (4.39)$$

$$\frac{\partial \varepsilon}{\partial t} + \frac{\partial(u\varepsilon)}{\partial x} + \frac{\partial(v\varepsilon)}{\partial y} + \frac{\partial(w\varepsilon)}{\partial z} = \frac{\partial}{\partial x} \left[\frac{\nu_T}{\sigma_\varepsilon} \frac{\partial \varepsilon}{\partial x} \right] + \frac{\partial}{\partial y} \left[\frac{\nu_T}{\sigma_\varepsilon} \frac{\partial \varepsilon}{\partial y} \right] + \frac{\partial}{\partial z} \left[\frac{\nu_T}{\sigma_\varepsilon} \frac{\partial \varepsilon}{\partial z} \right] + \frac{\varepsilon}{k} (C_{\varepsilon 1} P - C_{\varepsilon 2} D_{est}) \quad (4.40)$$

where the production term

$$P = 2\nu_T \left[\left(\frac{\partial u}{\partial x} \right)^2 + \left(\frac{\partial v}{\partial y} \right)^2 + \left(\frac{\partial w}{\partial z} \right)^2 \right] + \nu_T \left[\left(\frac{\partial u}{\partial y} + \frac{\partial v}{\partial x} \right)^2 + \left(\frac{\partial v}{\partial z} + \frac{\partial w}{\partial y} \right)^2 + \left(\frac{\partial w}{\partial x} + \frac{\partial u}{\partial z} \right)^2 \right] \quad (4.41)$$

And the destruction term $D_{est} = \varepsilon$.

$$\sigma_k = 1.0, \sigma_\varepsilon = 1.3, C_{\varepsilon 1} = 1.44 \text{ and } C_{\varepsilon 2} = 1.92$$

These adjustable constants have been are issued by data fitting for a wide range of turbulent flows [22].

When k and ε are found by solving the differential transport equations, the turbulent viscosity is calculated by Equation 4.42, with c_μ a constant which can be determined by carrying out experiments for simple turbulent flows.

$$\mu_T = \rho c_\mu \frac{k^2}{\varepsilon} \quad (4.42)$$

This model is called $k-\varepsilon$ model and is chosen because its performance has been assessed against a number of practical flows, and especially because it predicts well shear layers and boundary layers.

4.2 Important dimensionless parameters

4.2.1 Reynolds number

The Reynolds number is a number used in fluid mechanics to describe the flow regime. This is one of the first parameters to calculate in a fluid-structure interaction study, because it is then used to calculate other parameters or to know if other parameters can be used. The Reynolds number is calculated as follows:

$$\text{Re} = \frac{UD}{\nu} \quad (4.43)$$

With U : velocity of the flow ($m.s^{-1}$)

D : characteristic length (m)

ν : kinematic viscosity ($m^2.s^{-1}$)

In cases met in this study, Reynolds numbers are between the order of 10^5 and 10^6

4.2.2 Froude number

In a flow, the Froude number characterized the relative importance of velocity forces compare to gravity forces. This number is used in free surface phenomenon, particularly in naval architecture studies.

$$Fr = \frac{U}{\sqrt{gD}} \quad (4.44)$$

4.3 Discretization and solution theory

4.3.1 General principles

A review of general principles of how the CFD code Ansys CFX works is performed here. Indeed, from the Navier-Stokes equations governing the flow to CFD results, the step of equations resolution has to be highlighted.

Governing equations of fluid dynamics can have an analytical solution only for a very simple flow in ideal conditions. Then, a numerical approach must be adopted to find

solutions for real flows. Hence, equations are discretized in order to be solved by a numerical method.

The domain where the flow needs to be resolved is split into a large number of control volumes through a mesh. Each quantity is conserved in each control volume where the equations are integrated on the volume [2]. This finite-volume method has been first introduced in two dimensions by McDonald in 1971 [26] and MacCormack and Paulay in 1972 [24]. It then extended in three dimensions by Rizzi and Inouye in 1973 [31].

If a mesh of a unit depth is considered, it can be represented in two dimensions as follows:

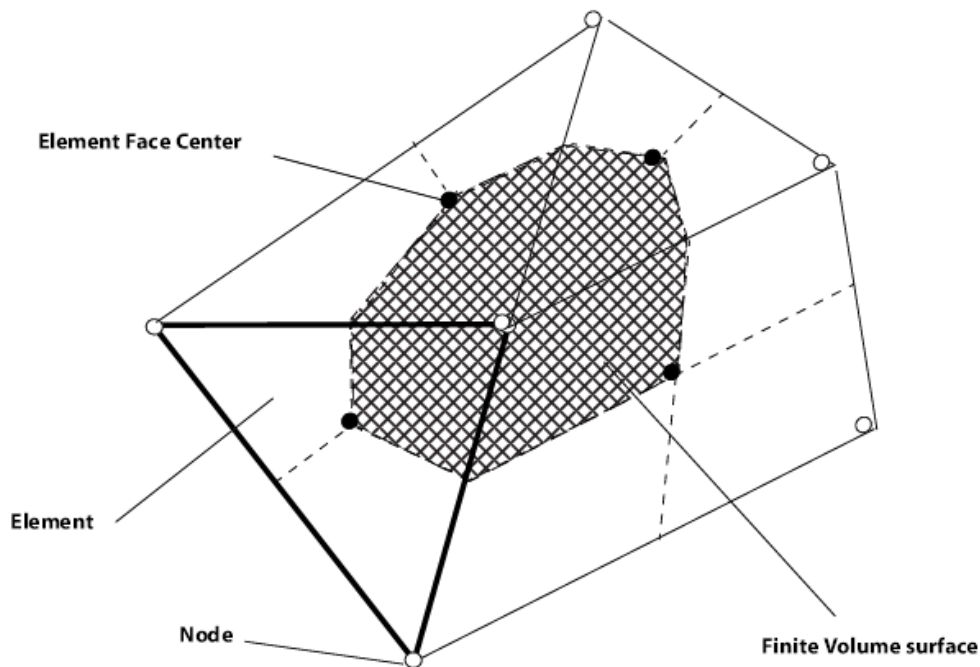


Figure 4.2 : Control volume surface (Ansys-CFX theory guide)

In the centre of each element of the mesh, the element face center defines a point. When there are several elements, points in the centre of the elements define a set of surfaces which defines the control volume. Control volumes are surrounding a node, where fluid properties and the solution of variables are stored.

Governing equations are then discretely approximated, on a base of series expansion approximations of continuous functions, such as the Taylor series. This approximation has an order-accuracy, which can be estimated by the factor of the timestep in the largest term truncated or the mesh spacing exponent. Most of the time, the order-

accuracy is the order of the first term truncated from the approximation. Increasing the order of accuracy by using more terms in the approximation is not always a good idea, since it increases computational needs, and it can imply a less robust behavior of the code, which means that numerical instabilities can develop.

Differential equations are then integrated over a control volume and solutions are stored at the mesh nodes. The operation is repeated until the convergence criteria or the maximum of iterations is reached, as can be seen on Figure 4.3.

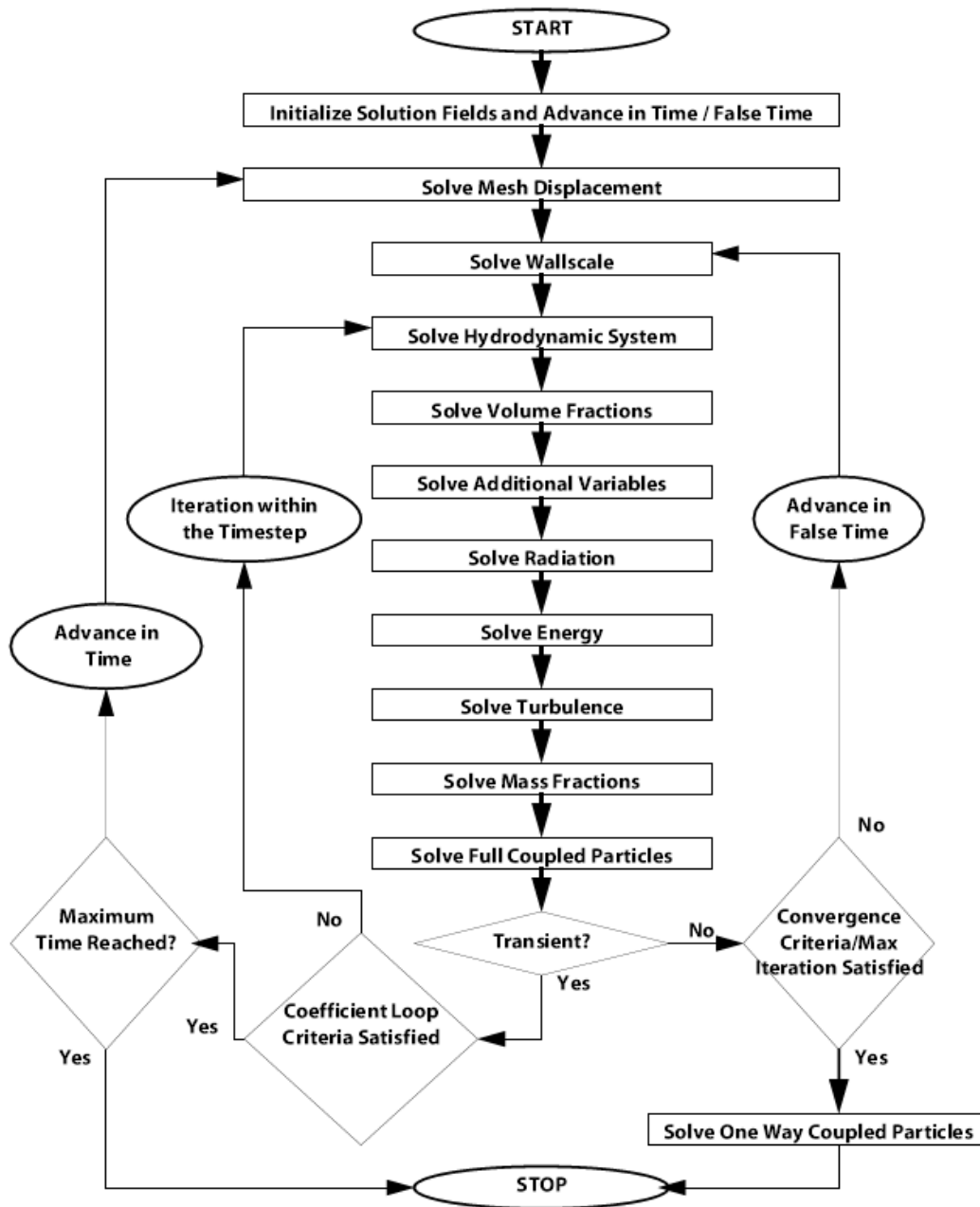


Figure 4.3 : Process used to reach solution of the flow in Ansys CFX (Ansys-CFX theory guide)

4.3.2 Convergence

It is considered that the flow solution can be trustable only if the run is converged, but what does convergence mean?

Stability and consistency are two necessary and sufficient criteria to obtain convergence. The stability is verified if errors are not propagated and amplified through the numerical solution process, this condition avoids the code to diverge. Consistency is when the truncation error approaches zero when the time step or the mesh spacing approaches zero [36].

A numerical method is said to be converged if the algebraic equations system has a solution approaching the true solution of the partial differential equations. In other words, the computed solution from discretized equations should approach the exact initials partial differential equations. For iterative solving, (used in CFD runs), the errors of the discretized equations are called residuals and are monitored on each time step. To say that the numerical process is converged, these residuals must be below the residual convergence criteria set for the run, on each node, and adding more iterations to the run must not change the solution. In order to get a satisfactory convergence, the residuals are supposed to decrease as the numerical process goes on.

4.3.3 Accuracy

If the mesh is refined enough, the accuracy of the solution, is the same as the order-accuracy of the equations approximations, this means it is the order of the first truncated term in the Taylor series approximation. To increase accuracy, a higher order approximation can be used in accordance with a more refined mesh. However, an accurate configuration can be insufficient for a more complicated case. Hence, the best way to get an accuracy solution is to perform a grid independency study, to determine the better mesh configuration, keeping in mind computational efficiency of resources.

Chapter 5: CFD modelling

5.1 Introduction

The software package used in this study to perform CFD calculations on the hydrofoils is ANSYS-CFX V11. CFX is based on a Reynolds Averaged Navier Stokes (RANS) finite-volume solver. The main characteristics of this simulation are unsteady, one phase flow, and use of a velocity profile and boundary layer meshing.

The main characteristics of the calculations performed for each stage of the process are presented in this section. Geometry and meshing considerations are shown first, then parameters for pre-processing stage, solver features, convergence and post-processing point of interests.

5.2 Geometry and meshing

5.2.1 Choice of Geometry

The first task is to define the size of the domain, depending on the size of the structure in this domain. If the domain is too small, the flow is not established when it leaves the domain. If it is too large, it has more nodes and a longer calculation time for results with no added benefits. Several first tests were performed to get the optimum size of the domain depending on the number of nodes and the results. It was decided to use a 40 m length, 35 m depth and 0.04 m width domain, which is a quasi-2D model to perform studies on foil shape design. When running the full delta shape, the domain is much larger, of 130m length by 35 m depth and 75 m width.

The axis basis is situated in the centre of the foil. The positive y-axis is oriented in the surface direction. Hence, when a lift result is positive, it means the lift is generated

upward, in the surface direction, whereas when the lift is negative, it is generated in the direction of the sea floor, which is what is expected.

5.2.2 Choice of Mesh

Being interested in drag and lift force, viscous effects around the structure have to be perfectly described. The choice of using a boundary layer mesh around the structure is made. From there, a size function is applied, so the fine mesh near the structure can rise slowly to a coarser shape elsewhere. The mesh is structured using a Cooper scheme. A mesh sensitivity study is performed to get the better compromise between number of nodes, calculation time and quality of results (cf § 6.3.1.2).

5.2.3 The Boundary Layer description

To represent correctly viscous effects near the foil, the numerical simulation has to take into account viscous effects at the wall and to resolve the rapid variations of flow variables that occur in the boundary layer region. This near wall region can be divided in two regions: the closest one from the wall is called the viscous sub layer, where the flow is almost laminar and the dominant role in momentum and heat transfer is played by molecular viscosity. Further away from the wall, turbulence dominates the mixing process in the logarithmic layer. Between those two regions, a transition region called buffer layer is a place of equal importance for viscous and turbulence effects.

With a $k-\varepsilon$ turbulence model used in this study, the flow is modelled in the boundary layer by a function called “wall function” and integrated in the code. This function is based on the idea that a logarithmic profile approximates well the velocity distribution near the wall, and then, at a given distance from the wall, a log law provide a mean to compute the fluid shear stress as a function of the velocity. The wall function method does not actually resolve the boundary layer but uses empirical formulas that impose suitable conditions near to the wall.

For accurate boundary layer computations, minimal requirements have to be satisfied when describing the boundary layer mesh, such as the distance of the first node from the wall, the spacing between nodes and the number of nodes in the boundary layer. The y^+ parameter is based on the distance from the wall to the first node and the wall shear stress, and is defined as follows:

$$y^+ = \frac{\rho u_\tau y}{\mu} \quad (5.1)$$

Where the friction velocity u_τ can be written:

$$u_\tau = \left(\frac{\tau_w}{\rho} \right)^{\frac{1}{2}} \quad (5.2)$$

And the average wall shear stress τ_w :

$$\tau_w = \rho U^2 \frac{C_f}{2} \quad (5.3)$$

And the friction coefficient C_f :

$$\frac{C_f}{2} = \frac{0.0296}{\text{Re}^{\frac{1}{5}}} \quad (5.4)$$

So

$$\tau_w = \rho U^2 \frac{0.0296}{\text{Re}^{\frac{1}{5}}} \quad (5.5)$$

And

$$u_\tau = U \sqrt{\frac{0.0296}{\text{Re}^{\frac{1}{5}}}} \quad (5.6)$$

And finally

$$y = \frac{\mu y^+}{\rho U \sqrt{\frac{0.0296}{\text{Re}^{\frac{1}{5}}}}} \quad (5.7)$$

For the structure considered, a $y^+ = 11$ is chosen. This value is based on experience of engineers in CFD. More generally, a y^+ chosen between 1 and 50 allows a small enough distance between the wall and the first node to produce accurate results. Hence, a value in the order of 10 produces very good results for the description of the boundary layer.

And $\mu = 1,5 \cdot 10^{-3} \text{ kg.m}^2 .\text{s}^{-1}$ for water at 5°C

$$\rho = 1000 \text{ kg.m}^{-3}$$

$U \approx 3m.s^{-1}$ velocity near the foil .

Re is the Reynolds number and it varies for cases considered in the study.

Once the distance of the first node from the wall is calculated, a growth ratio factor between 1.2 and 1.4 is set with a number of nodes of approximately 10, to reach the boundary layer thickness calculated as follows:

Another parameter called boundary layer thickness is defined as follows:

$$\delta = \frac{D \times 0.385}{Re^{\frac{1}{5}}} \quad (5.8)$$

5.3 Pre-processing stage

5.3.1 Boundary conditions

Boundary conditions were applied on the seven surfaces of the domain. As can be seen on Figure 5.1, INLET, OUTLET, BOTTOM, TOP, SIDES and PIPE are the name of the surfaces to set the boundary conditions.

- At the INLET, the condition of velocity inlet is set, and then a file with the characteristics of the velocity profile described at §5.3.2 is set as input.
- At the OUTLET, the condition of OUTFLOW is set with an average static pressure of 300000 Pa or a mass flow rate.
- On the BOTTOM and PIPE, a condition of no slip smooth wall is set. This means that the roughness is small on these boundaries, and it is the same for the bottom and on the structure.
- On the TOP, a condition of free slip wall is set, which means that the free surface can be represented as a wall boundary condition but without any roughness. A free surface boundary condition is not used to simplify the case, and because this boundary condition wouldn't bring additional information since the underwater structure is deep enough not to interfere on the free surface.

- At SIDES, a condition of symmetry is applied. This condition allows using a very small thickness for the domain, and having a quasi-2D domain instead of representing the 36 m length of the pipe.

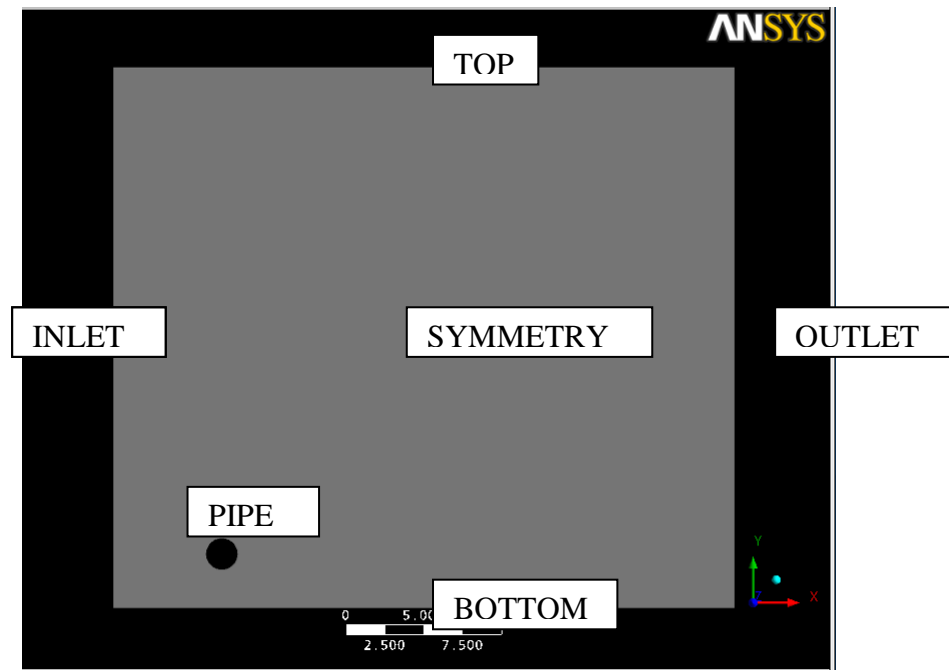


Figure 5.1 : Boundary conditions

5.3.2 A special boundary condition : the velocity inlet

To replicate tidal flows, a velocity profile has been created at the inlet. Indeed, in the sea, the velocity at the sea floor is equal to zero, because of viscous effect near the sea floor, and is maximal at the sea surface. Between the sea floor and the surface, the velocity has a profile which can be defined by a numerical expression. The velocity profile used is a turbulent profile, commonly used when designing a tidal turbine. The velocity profile is calculated in each vertical point as follows:

$$u = U_{\infty} \left(\frac{y}{h} \right)^{\frac{1}{7}} \quad (5.9)$$

h : Depth of the sea

y : Vertical position of the point where the velocity is being calculated

U_{∞} : Maximum velocity at sea surface

For a maximum velocity at sea surface of 4.5 m.s^{-1} , and a depth of 35 m , this is the velocity profile:

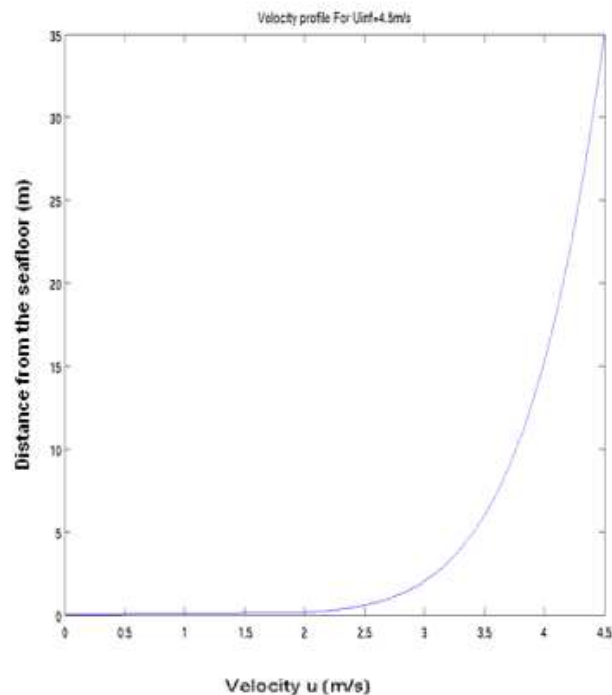


Figure 5.2 : Velocity profile for a depth of 35 m and a maximum velocity of 4.5 m.s^{-1}

The Matlab script written to compute this velocity profile and the output velocity profile file are shown in Appendix 2.

5.3.3 Simulation type

For all simulations, the steady case was run first. But because of alternately vortex shedding in the wake of the cylinder, a picture of the flow taken at a time t won't be the same as a picture taken at a later time. This is the characteristic of unsteady flows and so the simulations are then run in unsteady mode. To run an unsteady case, a file, describing the initial conditions issued from the steady run results, needs to be loaded.

For the unsteady run, the total simulation time and the timestep need to be set up. To calculate the timestep, the following rule is followed:

$$U = \frac{\Delta d}{\Delta t} \quad (5.10)$$

With U the velocity near the pipe, Δd the finest mesh size near the pipe and Δt the timestep. Another important parameter is the number of outer loop iterations performed during one timestep. As shown on Figure 4.3 in §4.3.1, outer loop iterations are iterations performed during one timestep and a sufficient number of outer loop iterations allows a better convergence of unsteady runs.

5.4 Solver stage

The high resolution advection scheme is used here, because of the high velocities and high gradient velocities considered. The second order backward Euler is applied for transient scheme. The k- ϵ turbulence model was chosen for the computations as it is robust, handles rotational flow and changes in turbulent length scale well, and is an industry standard, allowing for fair comparisons to previous computations.

A number of between 10 and 500 maximum coefficient loops is set in convergence control, depending on the case considered and its ability to converge quickly or not, and a residual target of 1.10^{-6} is requested as the convergence criteria. This is a factor of hundred lower than the default setting, as it is felt that the flow pattern is of greater importance for unsteady flows.

As only residuals are plotted in Ansys-CFX Solver, a checking of the drag and lift force evolution needs to be performed from a monitor file in the pos-processing stage: when drag and lift forces reach regular oscillations, with a constant mean, the run can be considered as converged.

5.5 Post-processing stage

A first view of results can be obtained with the post-processor included in Ansys CFX: velocity, streamlines or vectors can be plotted on a plane to have a visual representation of the flow around the structure. But for accurate results, to have data of the forces (such as drag and lift force) exerted on the structure at each timestep, a monitor options file is written. Indeed, much information are written in this file, like the force and moment exerted in all direction and on all boundary conditions. So to get the main

interesting information, which is the drag and lift on the structure, the file needs to be post-processed, to get the full drag, the drag in the x and y direction need to be added, and the same operation is performed for the lift. This operation is carried out with the help of a Matlab script, and drag and lift evolution charts are also plotted (cf Appendix 3). For unsteady runs, drag and lift evolution charts allows monitoring the convergence of drag and lift coefficients, and help to decide if the numerical process is converged. Indeed, drag and lift coefficient residuals, which are plotted with Fluent, are not in CFX, and hence, this technique is required to check unsteady runs convergence.

Chapter 6: Validation calculations

6.1 Introduction

Because the case of the circular cylinder has been the subject of a large number of studies, from the theoretical point of view to numerical ways, in CFD or in panel method, it makes a good validation case to start the studies. The presentation of the case is first performed, with geometry and mesh parameters. Then, parameters used in the set-up of the case are described, and to finish results are shown in a last section. For the particular case of the cylinder, lift and drag results with two different boundary layer meshes are shown and compared to theoretical results, then a sensitivity study on the number of nodes in the mesh is performed, then the influence of the velocity on the quantity of lift force generated is presented, and a visual description of the flow from CFD results is made and compared to descriptions found in literature.

6.2 Geometry and set up

The considered geometry is quasi-2D, it uses a 2m diameter cylinder, the centre of which is situated 2.5 m from the sea floor. The domain used is 35m depth by 40 m long and since it is symmetrical along the height of the cylinder, only a 4 cm wide slice is modelled, to reduce the number of nodes. A boundary layer is set up (cf § 6.2.2) and the mesh is growing up gradually from this boundary layer to a coarser mesh through a size function.

The case ran with a velocity profile of 4.5 m.s^{-1} at the sea surface at inlet, and an average pressure of 300 000 Pa at the outlet. It ran first steady and then unsteady, with a k- ϵ turbulence model. The others important parameters are calculated here.

6.2.1 Reynolds number

For the studied structure, the cylinder centre is situated at 2.5m from the sea floor. At this depth, the velocity is $u=3.09 \text{ m.s}^{-1}$ according to the velocity profile law. D , the characteristic length is the diameter of the pipe and is 2 m. And ν the kinematic viscosity is $1,520.10^{-6} \text{ m}^2.\text{s}^{-1}$ if the water is at 5°C .

So at 5°C, $Re = 4,06.10^6$ and the flow around the pipe is turbulent.

6.2.2 Boundary layer

Knowing the Reynolds number for the flow around a cylinder case, the parameters used to build the boundary layer mesh from § 5.2.3 can be calculated:

$y = 1,5.10^{-4} \text{ m}$ is the distance of the first node from the wall.

$\delta = 3,7.10^{-2} \text{ m}$ is the boundary layer thickness for the structure considered.

To reach this boundary layer thickness from the first node, 14 rows in the boundary layer mesh are used, with a growth ratio of 1.4.

6.2.3 Drag coefficient for a cylinder near a wall

For a circular cylinder, the drag coefficient is calculated according to the following chart:

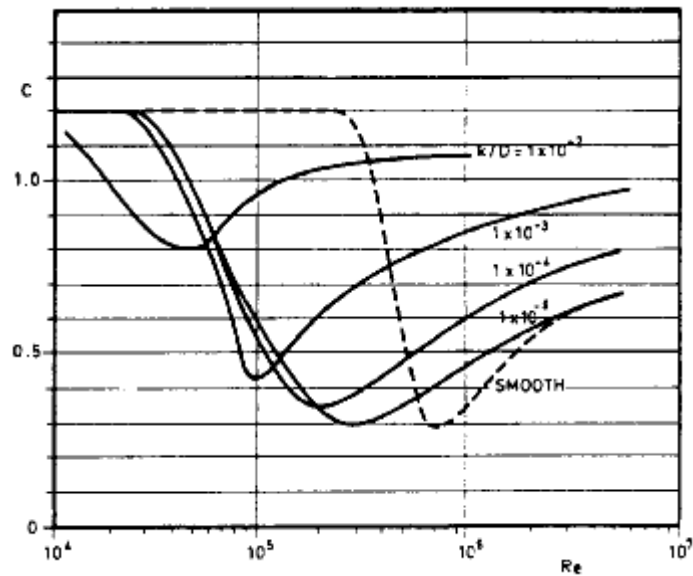


Figure 6.1 : Drag coefficient for various roughness of a circular cylinder for steady flow in critical flow regime [10].

The drag coefficient in infinite domain for the Reynolds number of 10^6 is about 0.33. This coefficient is multiplied by a correction factor for a cylinder close to a fixed boundary (cf Figure 6.2).

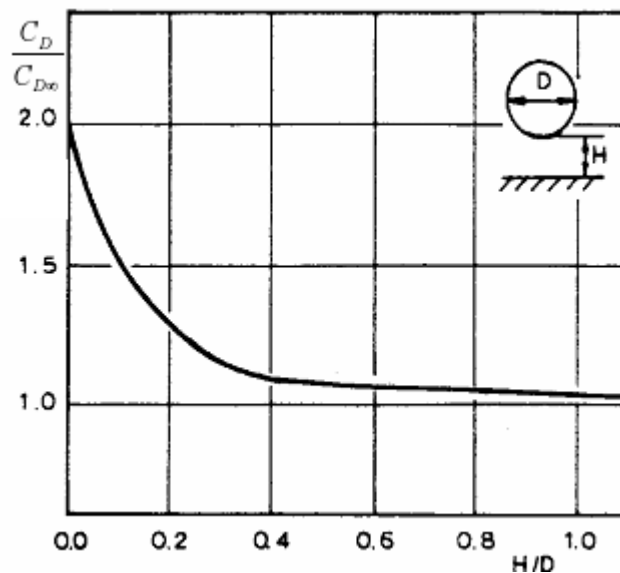


Figure 6.2 : Influence of a fixed boundary on the drag coefficient of a circular cylinder [10].

For the structure considered here, this coefficient is $\frac{C_d}{C_{d\infty}} = 1.08$

So the drag coefficient for the circular cylinder considered near a fixed boundary is $C_d = 1.08 \times C_{d\infty} = 1.08 \times 0.33 = 0.3564$

From this theoretical drag coefficient, the theoretical drag force can be calculated, according to §3.4: $F_{drag} = \frac{1}{2} \rho A C_D u^2(y)$. To estimate the velocity u , which depends on the depth, a constant value is taken as a first approximation. $u = 3.09 m.s^{-1}$, which is the velocity at 2.5 m above the sea floor. A is the characteristic area and is equal to $D \times L$, with $D=2m$ and L the length of the pipe (4 cm in CFD runs).

So the theoretical drag force is calculated as $F_{drag} = 139.5 N$ for the slice of 4 cm. And for a pipe of 25 m length the theoretical drag force is then 87 200 N.

6.3 Results

6.3.1 Mesh size influence

6.3.1.1 Boundary layer mesh

Two different boundary layer meshes are tested here to show the importance of an appropriate boundary layer grid to describe viscous effects around the structure. As described in §5.2.3, the quality of the boundary layer depends on the y^+ parameter. The first boundary layer tested has a y^+ of 700 and the second one of 11.

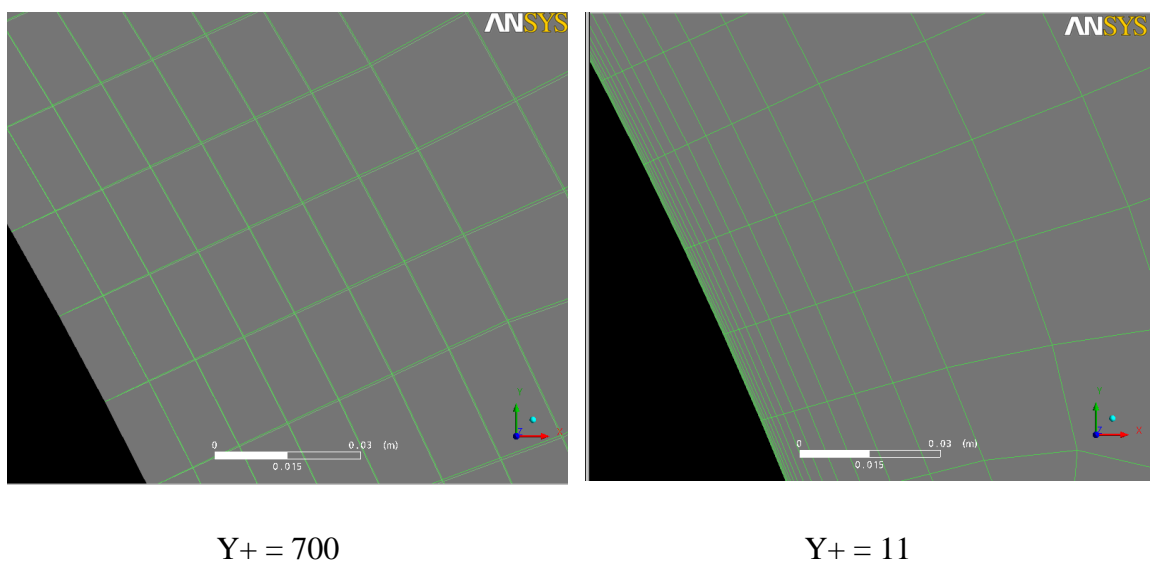


Figure 6.3 : Influence of y^+ parameter on boundary layer mesh quality

For a 25 m length pipe, the comparison between the two meshes and theoretical results are shown in the following table:

	Theoretical	y+ = 11	y+ = 700
Lift	0	-7 000 N	-4 800 N
Drag	87 200 N	86 000 N	91 000 N

Table 6.1 : Drag and lift around a 25 m cylinder for two different boundary layers

These results show that the boundary layer built with a y^+ equal to 11 produces a drag force which can be compared to the theoretical results. The lift force can not really be compared because of the shear flow induced by the velocity profile and the proximity from the ground which can influence the lift force.

These results confirm the fact that viscous effects are better described with a thin boundary layer, in this case with a y^+ equal to 11.

6.3.1.2 Number of nodes, sensitivity study

A sensitivity study is performed to find out the best mesh size to use for simulations. Three different mesh sizes are tested, from 25 000 nodes to 200 000. The drag coefficient is then computed for each simulation and a chart is plotted (cf Figure 6.4). The drag coefficient calculated theoretically in §6.2.3 is also plotted, to identify the point where the two lines meet each other, and obtain the best number of nodes for the simulations.

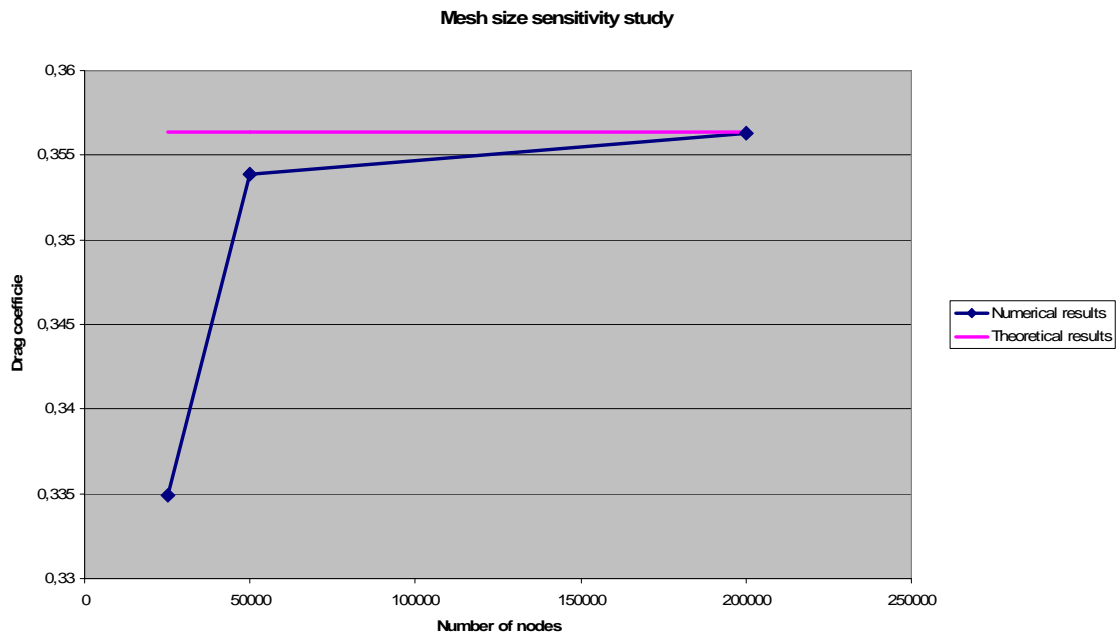


Figure 6.4 : Mesh sensitivity study

It appears that the best number of nodes to match a result close from the theoretical one would be 200 000. Further simulations are then performed with a boundary layer described by a y^+ of 11 and about 200 000 nodes.

6.3.2 Velocity influence

The influence of velocity on drag and lift force is shown for the flow around the circular cylinder. As the lift and drag force are dependant of the square velocity (cf §3.4), they both are more important for a greater velocity than for a slower one, as can be seen on the following table:

	2 m/s	4.5 m/s
Lift	-900 N	-7 000 N
Drag	19 000 N	86 000 N

Table 6.2: Drag and lift force for two velocities around the 25 m length cylinder

6.3.3 Comparison with theory

As can be seen on Figure 6.5, the turbulent wake can be compared to the one observed in the last case of §3.2. The wake is quite small and vortices are shed behind the cylinder. The wake does start at 120° from the incoming flow direction, as mentioned in §3.2.

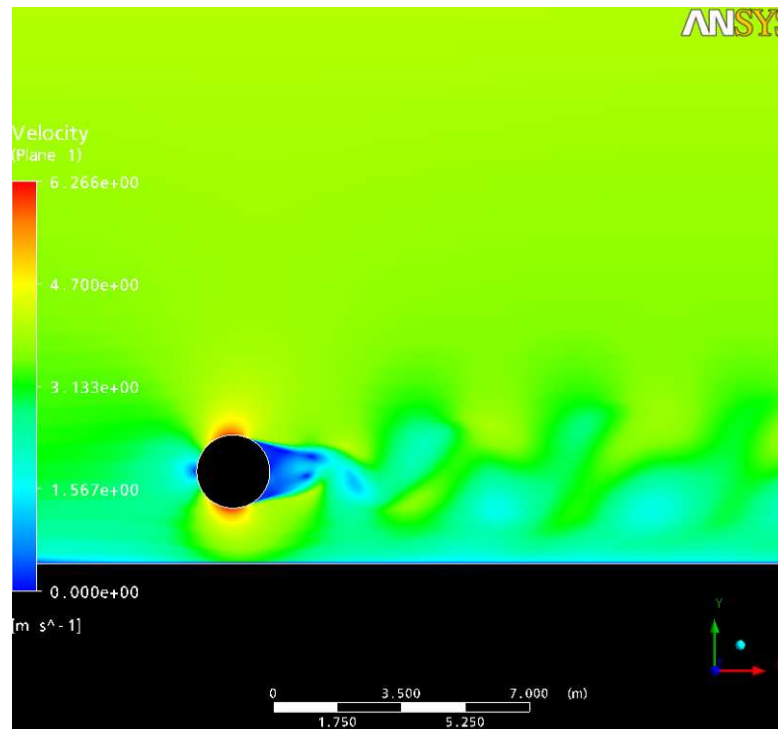


Figure 6.5 : Vortex shedding and wake at 120° for a Re of 4.10^6

The drag and lift coefficients are calculated from CFD results and are presented in the following table:

	2 m/s	4.5 m/s
Lift coefficient	-0.0088	-0.0286
Drag coefficient	0.1854	0.3515

Table 6.3 : Drag and lift coefficient for two velocities around the cylinder

The drag coefficient obtained for a velocity of 4.5 m/s is 0.3515 and is comparable to the drag coefficient of 0.3564 obtained from theory (§6.2.3).

6.4 Conclusion

The visual comparison between CFD results and theory for the flow around a cylinder shows a first point of agreement. This result is confirmed by more accurate results, with a boundary layer efficiently described, and a number of 200 000 nodes in the domain, the drag coefficient issued from CFD runs for the flow around a cylinder also matches the theory presented in §6.2.3. Hence, parameters used in this chapter to perform CFD calculations proved to produce accurate results which are comparable to the theory. These parameters are used again to mesh and run CFD calculations of the flow around a hydrofoil, since both flows are in the same conditions.

Chapter 7: Design of a foil generating negative lift

7.1 Preliminary studies of the hydrofoil

7.1.1 Introduction

After validating the case of a cylinder, the first stage of foil design can start. These preliminary studies are conducted to get some information about how parameters such as symmetry of the foil, distortion (or camber) of the foil, chord or distance from the sea floor are influencing the drag and lift force.

7.1.2 Geometry and set up

The size of the domain is the same as for the cylinder, with 40x35x0.04m. A boundary layer mesh with a y^+ of 11 and a wall function are used to describe viscous effects on the foil, and a size function allows to the mesh to grow up from the foil to the domain boundaries. A typical mesh of 260 000 nodes used for these studies is shown in Figure 7.1.

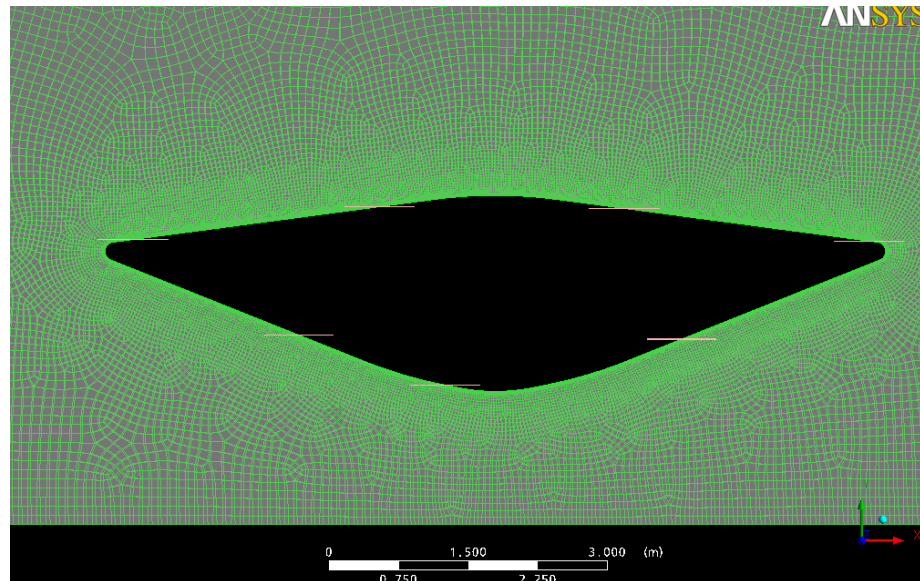
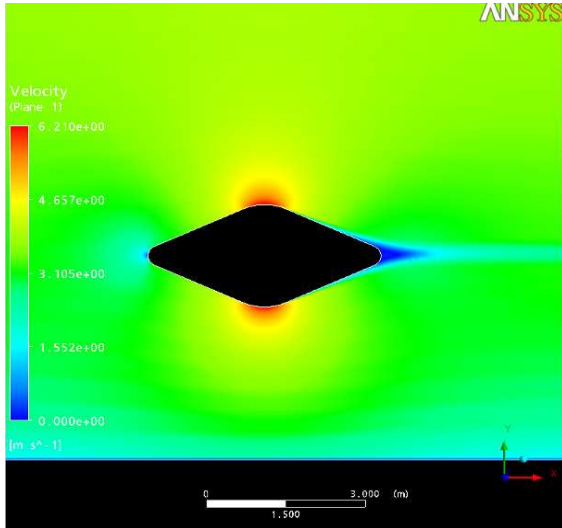


Figure 7.1 : Typical mesh used for preliminary studies on the hydrofoil

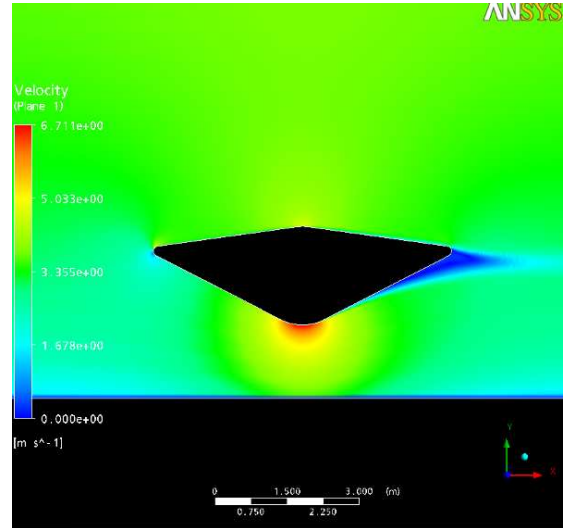
The inlet is a velocity profile with a maximum of 4.5 m/s and the outlet is an average static pressure of 300 000 Pa.

7.1.3 Comparison between ideal symmetrical and asymmetrical wing

To start the shape optimization, a comparison study between a symmetrical and asymmetrical foil with a longer chord is performed. The symmetrical one is named A, and the asymmetrical one called B. These foils are made with ideal plates around the cylinder, it means that the plates do not have any thickness, as in an ideal case. Note the hydrofoil has to be designed so it fits around the 2m diameter horizontal pipe of the structure and also such that three hydrofoils can be accommodated on the structure. This can be achieved if the foil does not exceed 25 m length for a chord of 6 m.



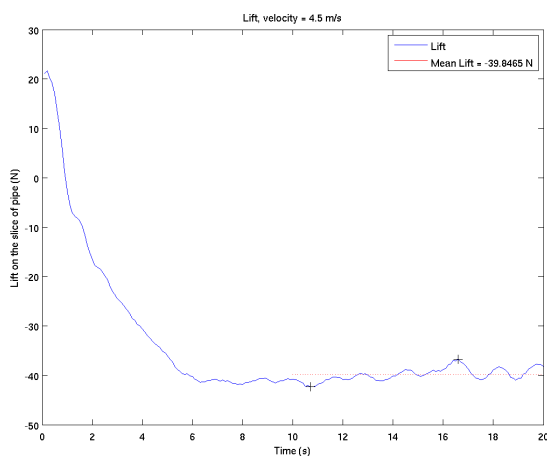
A



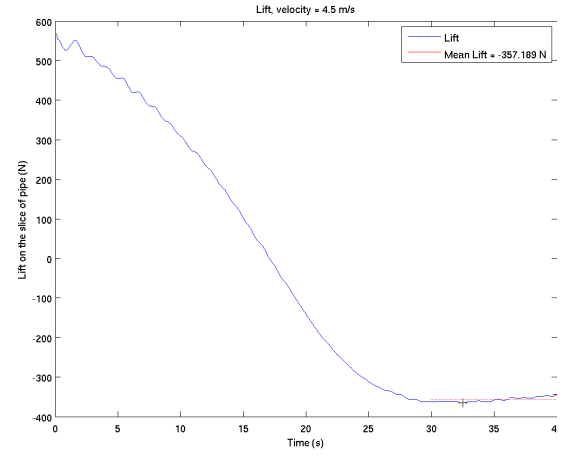
B

Figure 7.2 : Velocity field around the foil (A) : symmetrical foil ; (B) asymmetrical foil

Since all cases are run unsteady, residuals in CFX do not show if the convergence is reached for drag and lift. To verify the convergence of the run, a plot of drag evolution versus time is performed. A first part of the curves show a decrease of values versus time, and on a second part, values are oscillating around a stable mean value which means drag and lift are converged. This mean value is the one considered in results presented. For cases A and B, the plots of lift force time series (cf Figure 7.3) show that the asymmetrical foil generates more downward lift force than the symmetrical one.



A



B

Figure 7.3 : Lift force on a 4 cm slice of foils A and B

When the drag force time series is plotted (cf Figure 7.4) it appears that the asymmetrical foil B has a larger drag force than the symmetrical foil A. This result seems logical, because the symmetrical foil A has a better hydrodynamic shape than foil B.

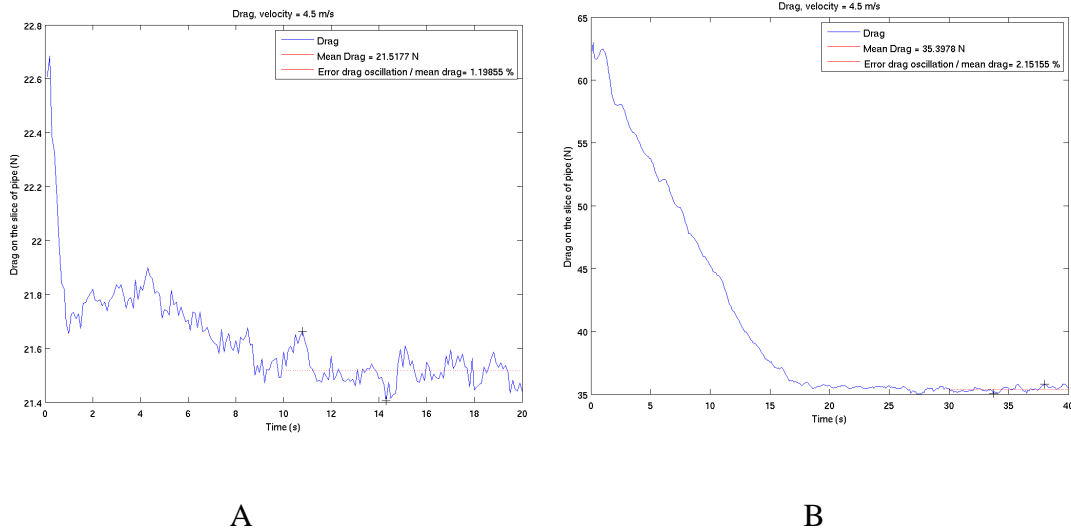


Figure 7.4 : Drag force on the 4 cm slice of foil A and B

When the drag and lift force are multiplied to get values on the 25 m length foil, results obtained are shown in the following table:

	A	B
Lift	-25 000 N	-223 200 N
Drag	13 000 N	22 000 N

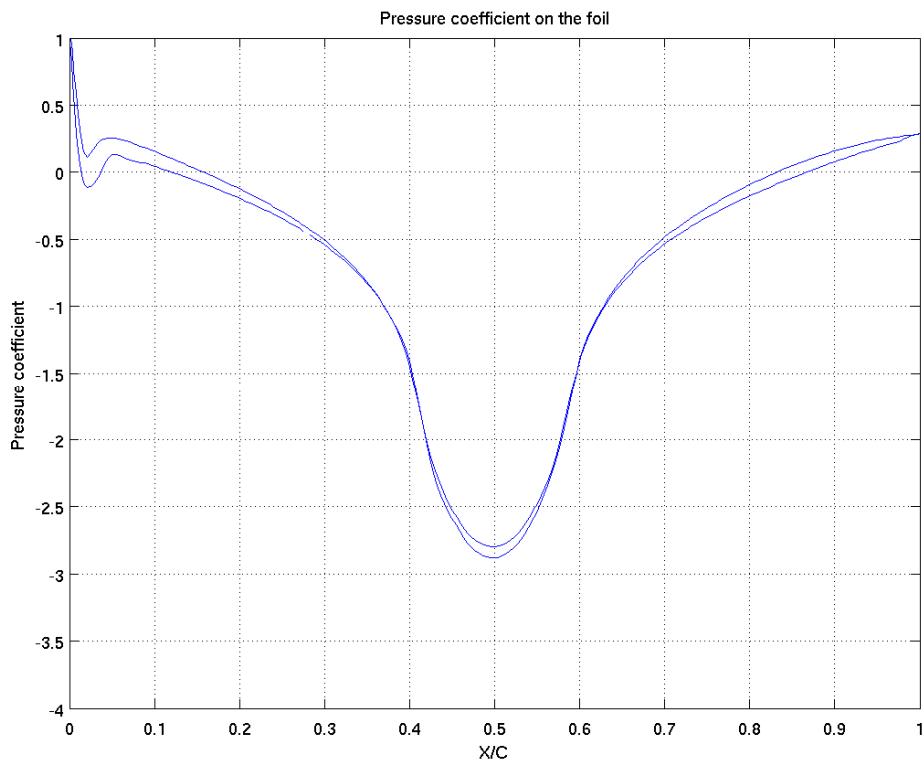
Table 7.1 : Drag and lift for the 25 m length foil A and B

Drag and lift coefficient are shown in Table 7.2.

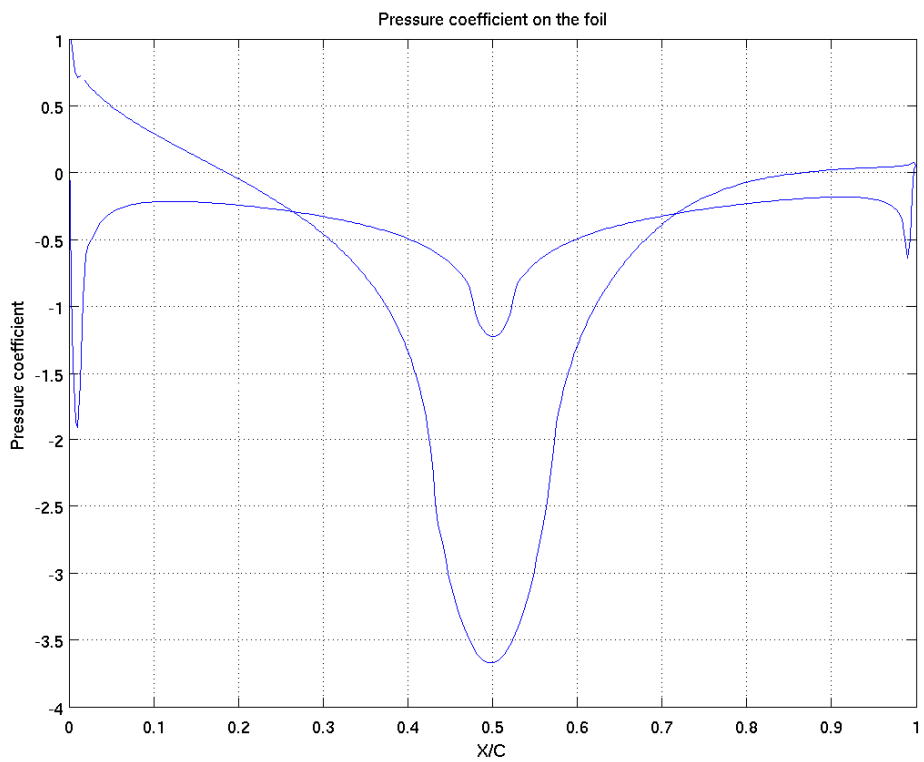
	A	B
Lift coefficient	-0.0339	-0.3041
Drag coefficient	0.0183	0.0301

Table 7.2: Drag and lift coefficient for foils A and B

The following charts are generated by plotting now the pressure distribution on a line around the foil versus the x-coordinate divided by the chord:



A



B

Figure 7.5 : Pressure one a line around foils A and B

These charts show that for a symmetrical profile (A), the pressure distribution is also symmetrical on both faces of the foil, whereas the difference of pressure on the two faces of asymmetrical profile B is more explicit and depends on the position on the foil. Indeed, for profile A there is almost no difference between the upper and lower face of the foil and the lift force is almost equal to zero. Around extremities of profile B, which means for $x/c < 0.3$ and $x/c > 0.7$, the pressure coefficient on the lower face is greater than for the upper face, and this can be seen as an upward lift on these parts of the foil. For the centre of the foil, which means for $x/c > 0.3$ and $x/c < 0.7$, the pressure coefficient is greater on the upper face than on the lower and this can be seen as a downward lift on this part of the foil. The total lift observed on the foil can be related to the difference of areas defined by the curve: the central area is greater than extreme areas and hence, the downward lift is greater than the upward lift, so the total lift is downward for profile B.

7.1.4 Comparison between real asymmetrical wings.

According to the idea that the lift force is greater for asymmetrical foils, when the distance along the bottom part is bigger than the distance on the top to induce an anticlockwise circulation and produce a downward lift, two asymmetrical profiles are now tested. The plates used to create the profile have now a thickness of 10 cm, to replicate the actual dimension of the foil when manufactured. To build a profile with this thickness, this one needs to be larger on the down part of the foil.

The profile named C has the same construction points as profile B, but is built with plates of 10 cm thickness. Profile D is more distorted than profile C, since the sides points of profile D are 0.75 m above the cylinder centre in the Y direction, whereas side points of profile C are 0.5 m above the cylinder centre in the Y direction.

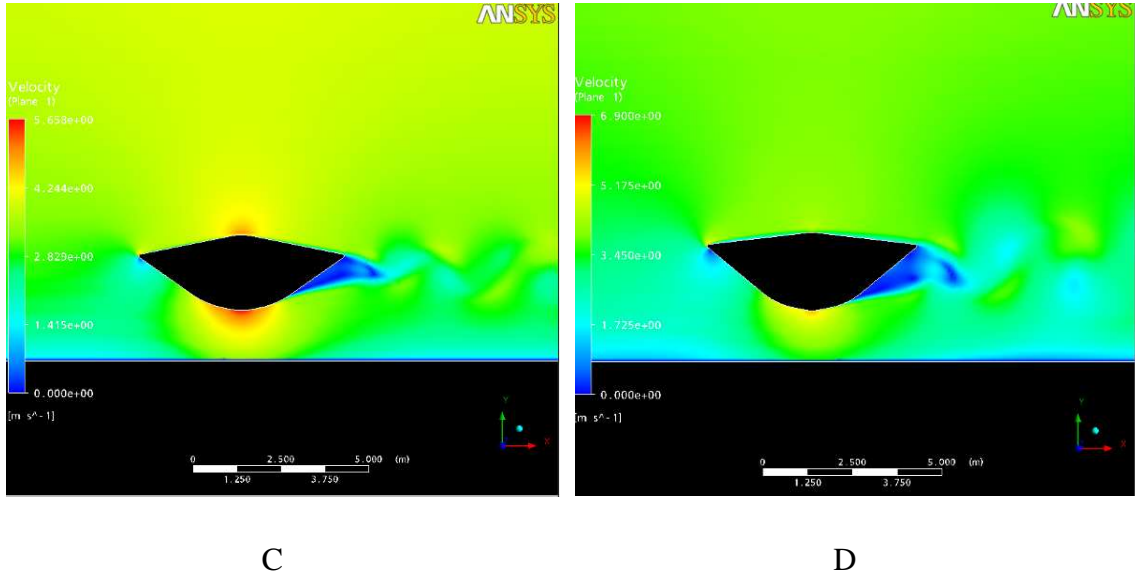
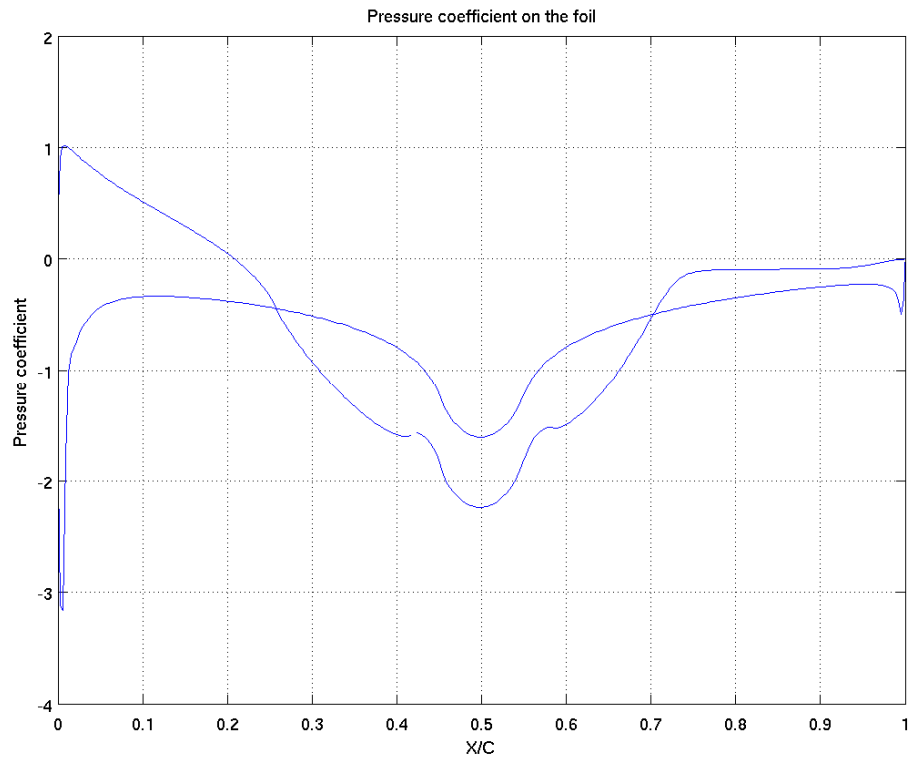
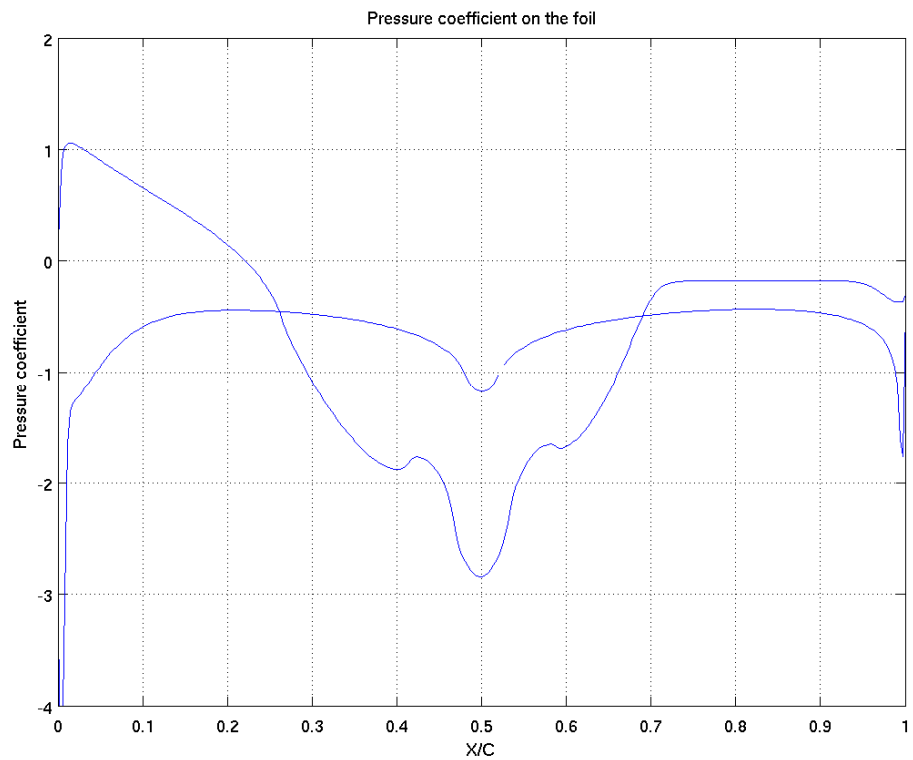


Figure 7.6 : Velocity field around asymmetrical foils C and D

The pressure distribution on a line around the foil is plotted versus the x-coordinate divided by the foil length:



C



D

Figure 7.7 : Pressure distribution on a line around foils C and D

The central area defined by difference of pressure between the upper and lower face of foil C is not as big as foil D, whereas extreme areas are approximately the same. This means that foil D produces more negative lift than foil C. It can also be noted that in both cases, the peak corresponding to the lower point of the foil is centred on two drops. These drops in the curve are due to the geometry of the foils and the way they have been constructed can imply that they are not perfectly smooth.

The results obtained from the interpretation of the pressure coefficient matches well with results presented in the following table for drag and lift force obtained for a 25 m length foil.

	C	D
Lift	40 400 N	-59 000 N
Drag	32 000 N	63 200 N

Table 7.3: Drag and lift force for the 25 m length foil C and D

	C	D
Lift coefficient	0.0553	-0.0806
Drag coefficient	0.0436	0.0862

Table 7.4: Drag and lift coefficient for foils C and D

Hence, profile C provides an upward lift force, which is the opposite of what is needed. However, the more distorted profile (D), produces a downward lift force of 59 000 N for a 25m length foil. This force is equivalent to 5.9 tons of downward lift force for one foil.

This is a start, but it is not enough to maintain the structure at its location. Indeed, 250 tons of downward lift would be needed for a velocity of 4.5 m/s, and with foil D, about 17.7 tons could be generated for the structure with the three foils.

7.1.5 Influence of the foil chord

Regarding the poor downward lift force created by the previous foils, a study of the influence on the chord has been performed. The thickness of the plates is still 10 cm, but instead of being 6 m length like profile C, the chord of profile E is now 10 m length.

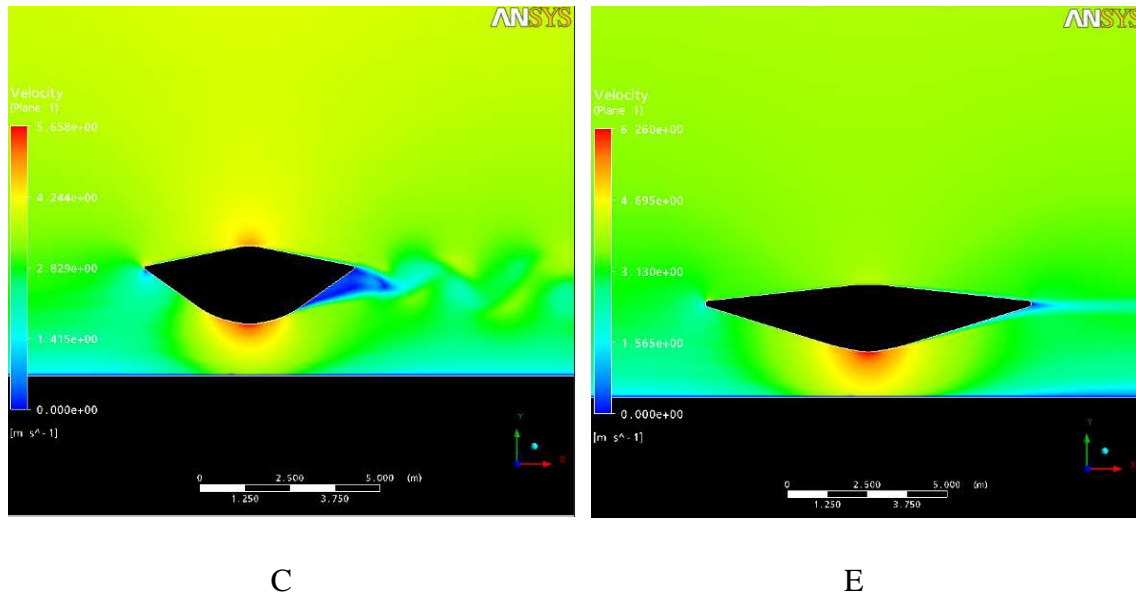
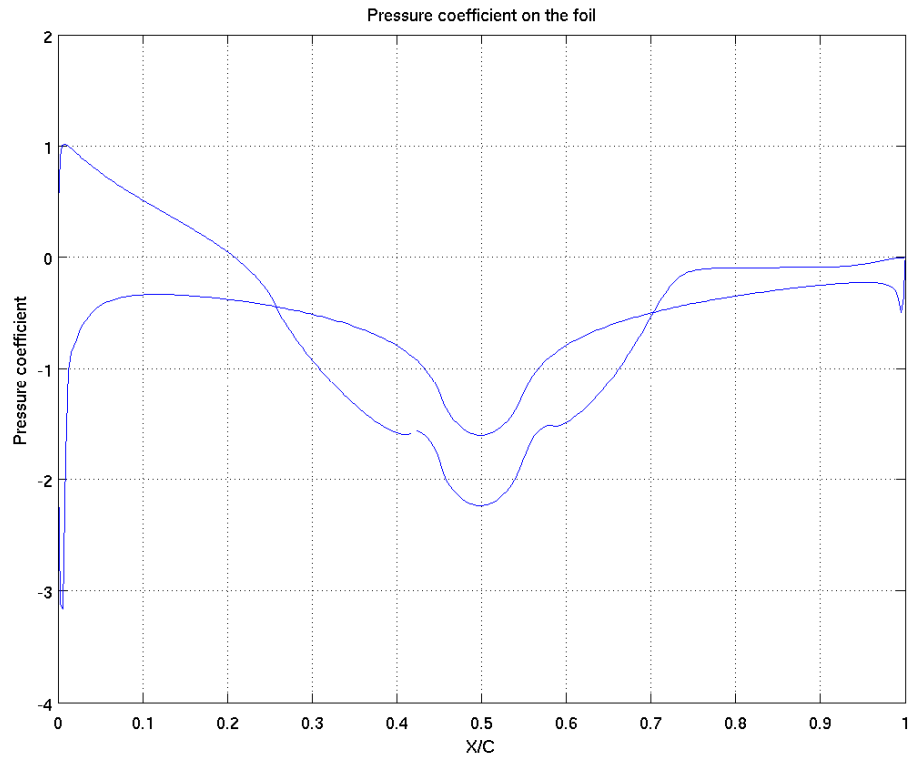
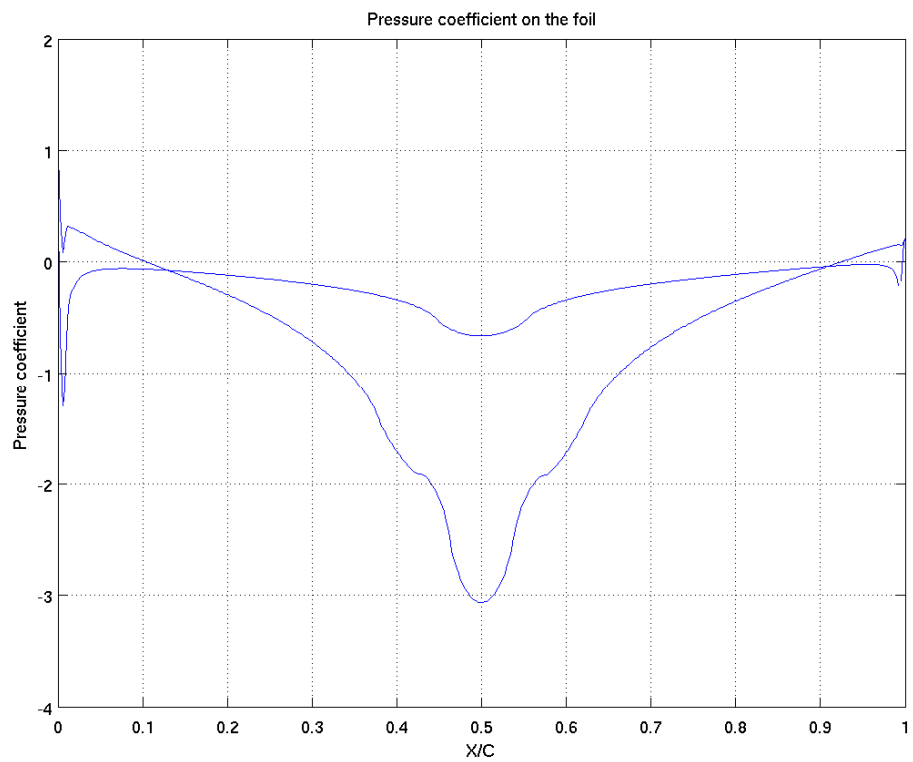


Figure 7.8 : Influence of the foil length

Figure 7.9 shows the pressure distribution on a line around the foil versus the x-coordinate divided by the chord.



C



E

Figure 7.9 : Pressure distribution on a line around foils C and E

It is clear that the difference of pressure between faces of profile E is valuable, and it takes effect on 80% of the foil chord compare to 45% for foil C. In the centre of the curve of profile E, a much bigger area is defined by the difference of pressure coefficient between the two sides of the foil than profile C. Hence, profile E can produce a much more important downward lift than profile C.

This observation matches with results presented in the following table which show that the shortest and less hydrodynamic shape C produces an upward lift and a sizeable drag, compared to the long chord profile E.

	C	E
Lift	40 400 N	-726 600 N
Drag	32 000 N	21 900 N

Table 7.5: Drag and lift for the 25 m length foil C and E

And associated drag and lift coefficient are presented in the following table:

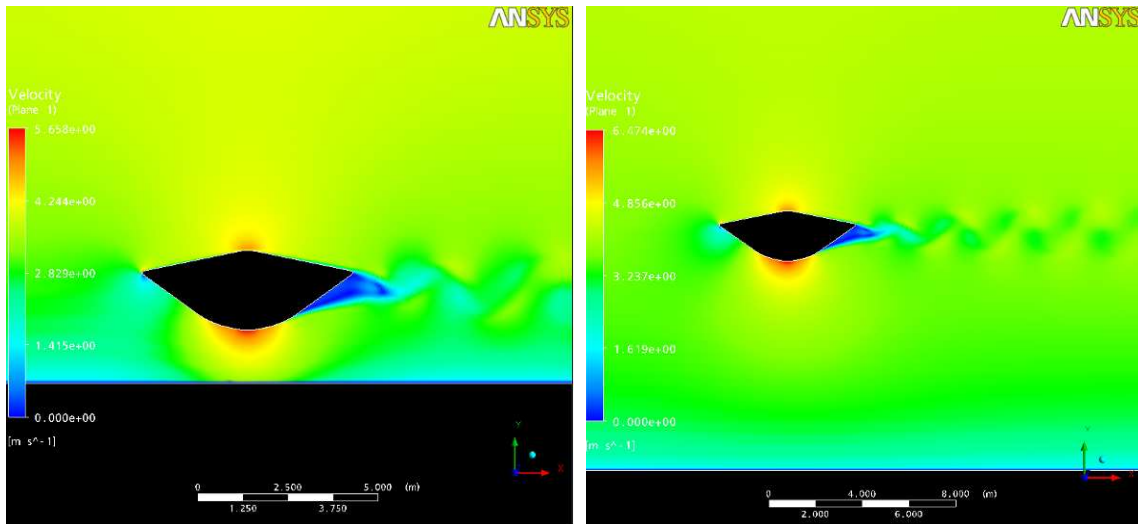
	C	E
Lift coefficient	0.0553	-0.5940
Drag coefficient	0.0436	0.0180

Table 7.6 : Drag and lift coefficient for foils C and E

Unfortunately, and as shown in the previous paragraph, shape C cannot be used on the structure since it does not produce the required effect of downward lift. Shape E produces a sizeable downward lift, with its 10 m wide chord. But it can not be used either because 10 m wide is too large to be fitted on the triangular structure. It would require too much space and too much material to be built, and hence, shape E is more a proof of concept than a proper solution.

7.1.6 Influence of the distance from the sea floor

To understand why the lift force of shape C is upward, the centre of the same shape as been placed 10m away from the sea floor in case C2 while it was only 2.5 m in case C.

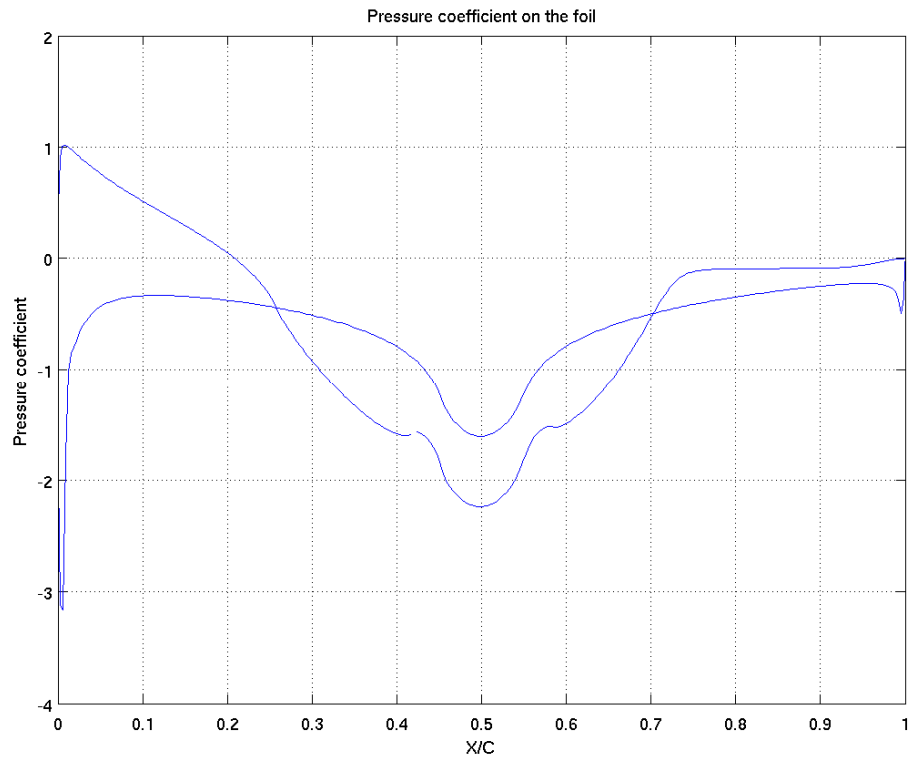


C

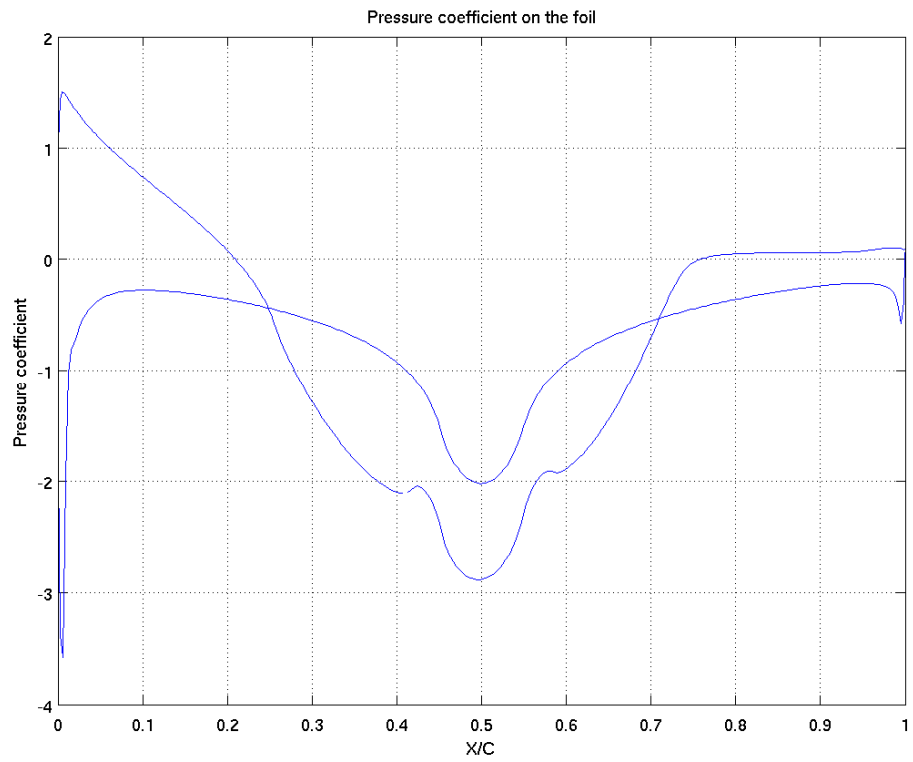
C2

Figure 7.10 : Influence of the distance from the sea floor for shape C

Figure 7.11 shows the pressure distribution on a line around the foil versus the x-coordinate divided by the chord.



C



C2

Figure 7.11 : Pressure distribution on a line around foils C and C2

Areas defined by the pressure coefficient curve are approximately the same for foil C and C2. Areas of curve for foil C2 are slightly bigger than for foil C. But the general shape stays identical since the foil shapes are exactly the same.

Results are shown in the following table, and the influence of the ground near the structure is not very big in the sense of quantity but the direction of the lift force is different. For a same foil shape a downward lift force is generated when the foil is far away from the ground whereas the force is generated upward when the structure is near the ground.

	C	C2
Lift	40 400 N	-10 500 N
Drag	32 000 N	32 500 N

Table 7.7: Drag and lift on a 25 m length shape C for different distances above the ground

	C	C2
Lift coefficient	0.0553	-0.0144
Drag coefficient	0.0436	0.0443

Table 7.8: Drag and lift coefficient around foils C and C2

This information is important because it means that the lift would have been greater if horizontal pipes (and hence profiles) would be situated further from the sea floor.

7.1.7 Conclusion

The influences of three shape parameters have been tested: the distortion of the foil in ideal and real condition, the chord of the foil and the distance from the sea floor. It has been shown that all these parameters are influencing the quantity of lift generated by the foil, but the increase of the chord and the distortion are the most influent.

7.2 Shape optimization on the hydrofoil

7.2.1 Introduction

Preliminary studies showed that main parameters influencing the quantity of the lift force are the distortion and the chord of the profile. For cost reasons, the profile cannot be too large, because the larger the quantity of materials is, the more expensive the profile becomes. That is why different chord are tested, between the one of 6 m and the one of 10m tested in §7.1.5. The profiles which produce the best downthrust are kept to perform distortion studies on.

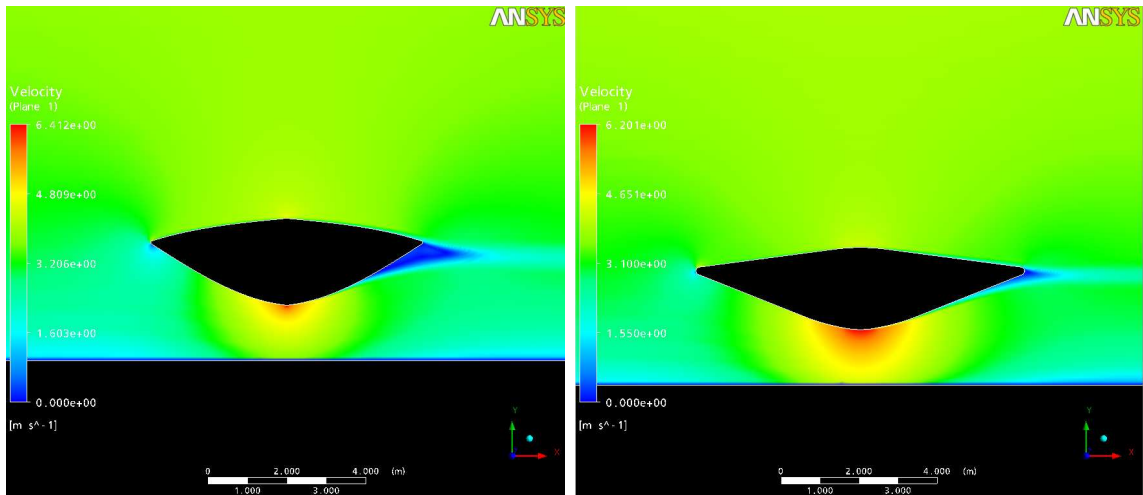
7.2.2 Geometry and set up

The geometry used is quite the same as in the last paragraph, meaning the size of the domain is still the same, with 40x35x0.04m. A boundary layer mesh with a y^+ of 11 is used to describe the viscous effects on the foil, and a size function allows to the mesh to grow up from the foil to the domain boundaries. A typical mesh of 260 000 nodes is used for these studies. A velocity profile with 4.5m/s surface velocity is used and the outlet boundary condition is set as an average static pressure of 300 000 Pa.

7.2.3 Results

7.2.3.1 Chord optimization

The foil dimensions can be defined by a ratio equal to the maximum thickness of the foil divided by the chord. The profiles tested in § 7.1.5 had a ratio of 1/3 (profile C) and 1/5 (profile E). Since the profile C does not produce enough downward lift and the profile E is too large to be reasonably constructed, other ratios can be tested. Profile F has a ratio of 1/3.5 and profile G of $\frac{1}{4}$. The pictures of the flow around the foils (Figure 7.12) already show that profile G has a much better hydrodynamic shape than F.

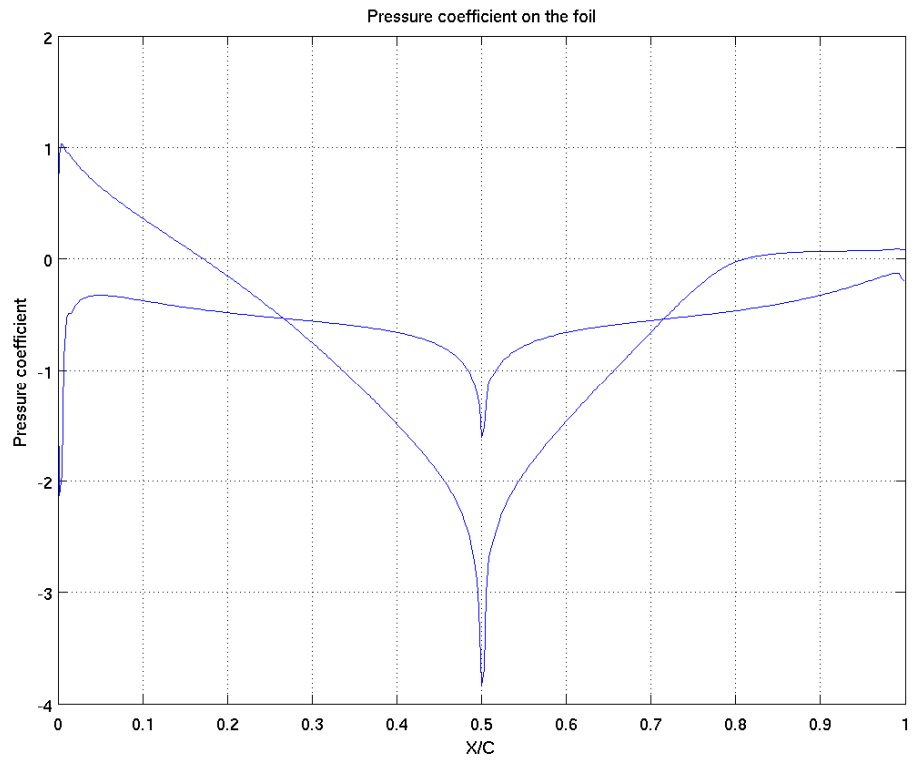


F

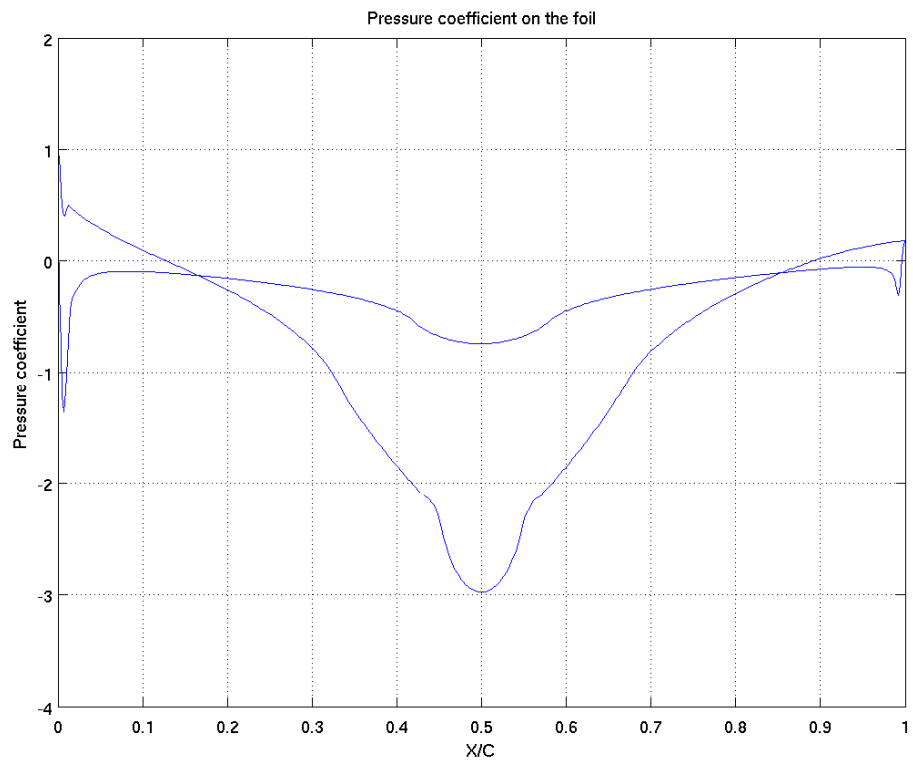
G

Figure 7.12 : Profile F : thickness to chord ratio of $1/3.5$. Profile G ratio of $1/4$

Figure 7.13 shows the pressure distribution on a line around the foil versus the x-coordinate divided by the chord.



F



G

Figure 7.13 : Pressure distribution on a line around foils F and G

The area defined by the difference of pressure coefficient between the upper and the lower face in the middle part of the foil is greater for foil G than for foil F. Foil F presents peaks value on the middle of the foil, which can be related to its shape, which is not as smooth as profile G on the higher and lower points of the foil.

The results of the 7m and the 8.4 m profile are shown in the following table. The difference between the profiles is important, because by increasing by 20% the chord of the foil, the lift increases by 800%.

	F	G
Lift	-54 700 N	-488 900 N
Drag	22 000 N	18 100 N

Table 7.9: Drag and Lift on a 22 m length profile of 7m chord (F) and 8.4 m chord (G)

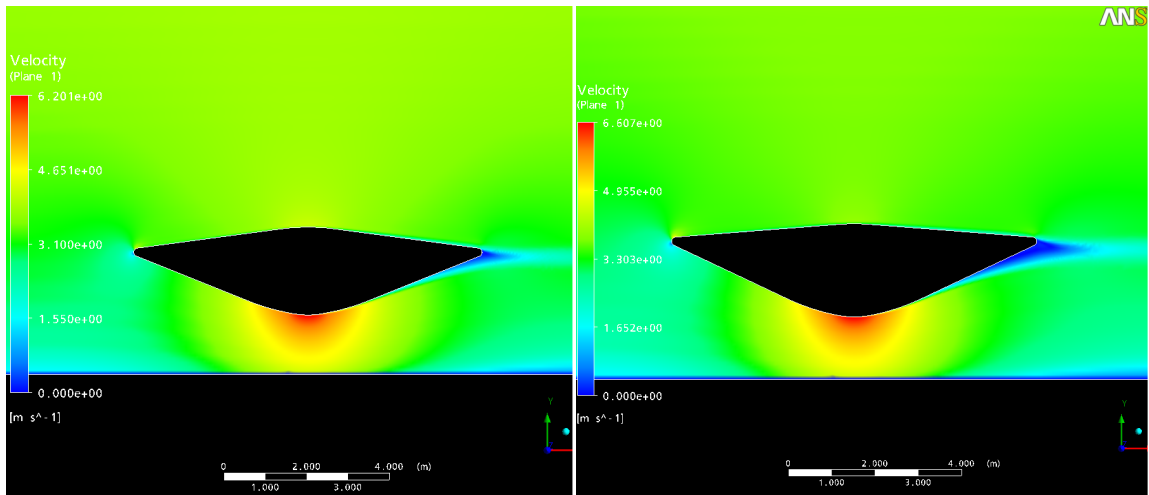
	F	G
Lift coefficient	-0.0675	-0.5419
Drag coefficient	0.0272	0.0200

Table 7.10 : Drag and lift coefficient on foils F and G

It's then clear that for a reasonable size, the profile G, with a chord of 8.4 m, produces a much better downward lift than profile F. Hence, this profile should be tested for different distortion parameters.

7.2.3.2 Distortion optimization

In this section, profile G is tested with two distortion parameters, like in §7.1.4. Profile G has its side points 0.5m above the cylinder centre in the Y direction whereas profile H has its side points 0.7m above the cylinder centre in the Y direction.

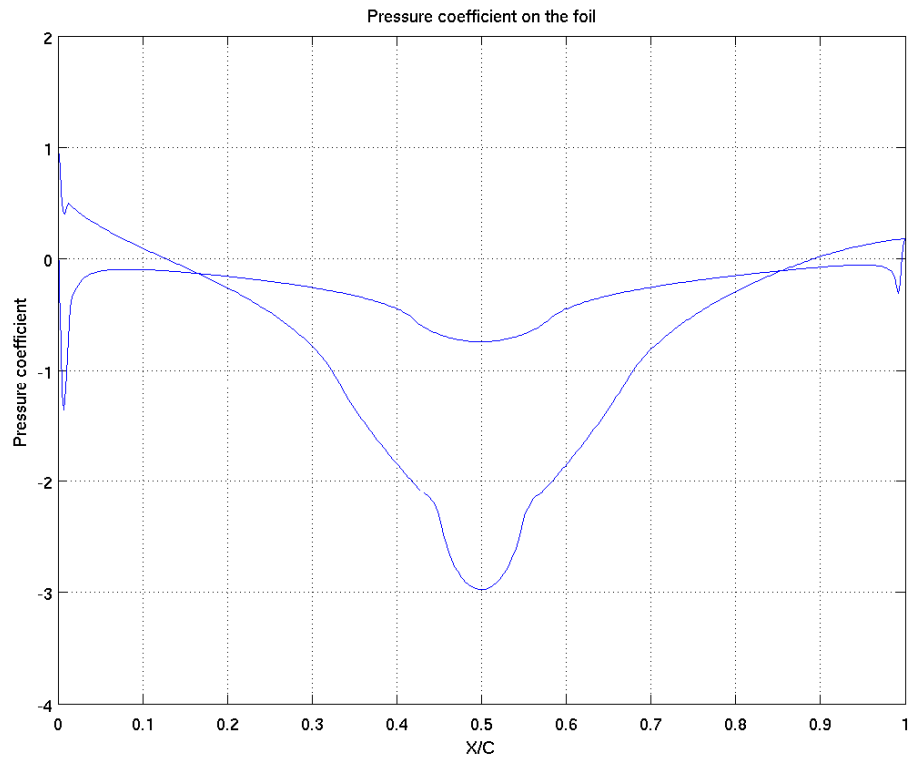


G

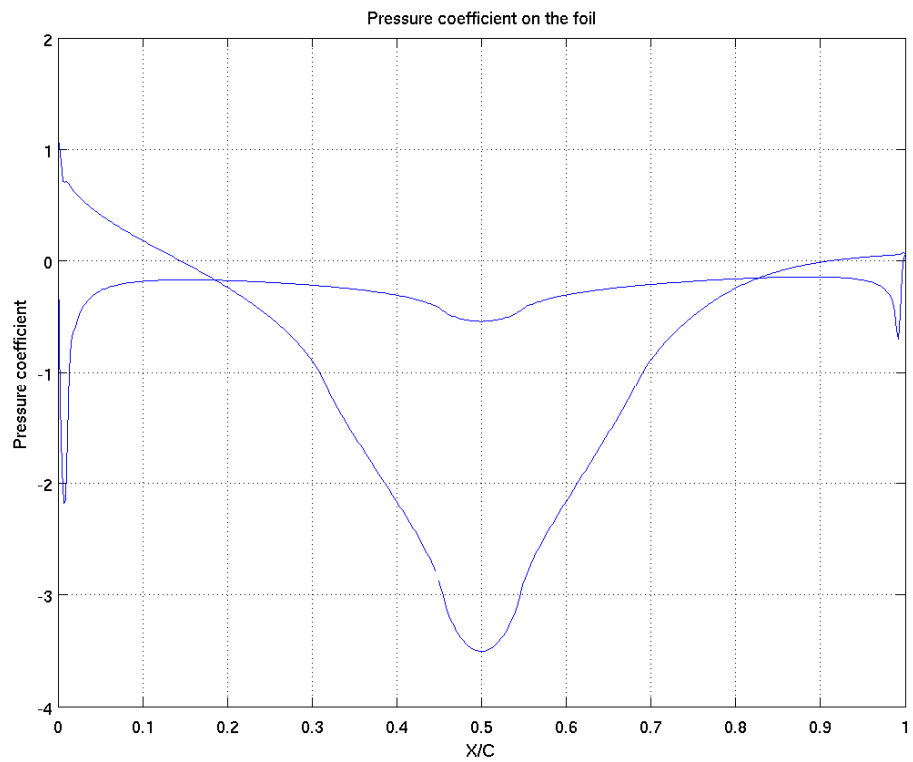
H

Figure 7.14 : Profile G : 8.4 m chord, side at 0.5m. Profile H : 8.4 m chord, side at 0.7

Figure 7.15 shows the pressure distribution on a line around the foil.



G



H

Figure 7.15 : Pressure distribution on a line around foils G and H

The area defined by the difference of pressure coefficient between the upper and lower face of profile H is bigger than profile G and results matches well with this observation, as can be seen in the following table:

	G	H
Lift	-488 900 N	-620 400 N
Drag	18 100 N	24 700 N

Table 7.11 : Drag and Lift of a 22m length profile. G: side at 0.5m. H: side at 0.7m

	G	H
Lift	-0.5419	-0.6864
Drag	0.0200	0.0276

Table 7.12: Drag and lift coefficient for foils G and H

Results in the previous table show that the more distorted profile produces 25% more lift than the less distorted one. The results were expected, since the effect of distortion on the rise of downward lift force production has been shown in §7.1.4. Hence profile H is the profile which generates the most downward lift.

7.2.4 Conclusion

The optimum chord for the profile was found to be 8.4 m. From this chord, a distortion study showed that the more distorted profile H could produce 62 tons of negative lift on a 22m foil facing the flow while the less distorted one, profile G would produce 50 tons. The two foils behind the flow could probably not produce as much lift as the foil facing the flow, because they are in the wake of the front foil, and because they will have an inclination of 30 degrees compare to the flow direction. Hence, with profile H, the maximum lift generated would be 186 tons, whereas it has been shown in §2.4 that between 250 and 311 tons are necessary to maintain the structure at its location, but this amount of negative lift generated could still help to reduce the amount of dead ballast used in anchoring.

Profile H generates the biggest downward lift but it is not chosen to be built for tank testing, since the distortion could be a problem for manufacturing. Furthermore, connection between edges would be too sharp and the profile could be brittle. Hence, profile G is the one which is constructed for tank testing, since it is the foil shape which produces the most important downward lift and respects the cost and material constraints.

Chapter 8: Comparison of tank testing and CFD results

8.1 Tank testing results

8.1.1 Introduction

Tank testing of the DeltaStream structure was performed in the IFREMER water tunnel in Boulogne sur Mer in July 2009, by Dr Florent Trarieux of the OENA group and Mr Christopher Freeman, who is a consultant with the turbomachinery group. Ifremer's testing basin in Boulogne sur Mer is designed to test devices towed on the sea floor, submersed, anchored in deep water or floating on the surface. The basic principle is to provide a homogeneous water flow around the model or the device being tested. The latter is maintained in the channel by either a towing device or the force and behavioural measuring devices. The tank overall dimensions are a length of 34 m, a width of 5 m and a height of 9 m. The working section dimensions are a length of 18 m, width of 4 m and height of 2 m. With its free surface vertical loop with water flow, and two 250 kW propeller pumps, the tank allows to generate an adjustable speed from 0.15 to 2 m/s. The goal of tank testing is to compare physical tests with results obtained in CFD, as it is still done in naval architecture and offshore engineering when designing a new structure.

8.1.2 Installation and set up

The DeltaStream structure is scaled to $1/30^{\text{th}}$ and the Froude similitude is applied to make the link between full scale and small scale parameters, and hence, a range of velocities from 0.6 to 1m/s are tested. The foil design process, described in Chapter 7, through a series of chronological events, would have lead to the employment of the

profile known as “profile G” in §7.2.3.2. But because of time and money constraints, the profile tested in small scale, which is called “profile I”, was built with sharper edges than its CFD basis, profile G. The difference between profile G and profile I (converted to full scale) is shown on Figure 8.1. Foot 1 and 3 are the feet facing the flow, and foot 2 is situated behind. A picture of the small structure being tested in the tank is shown on Figure 8.2.

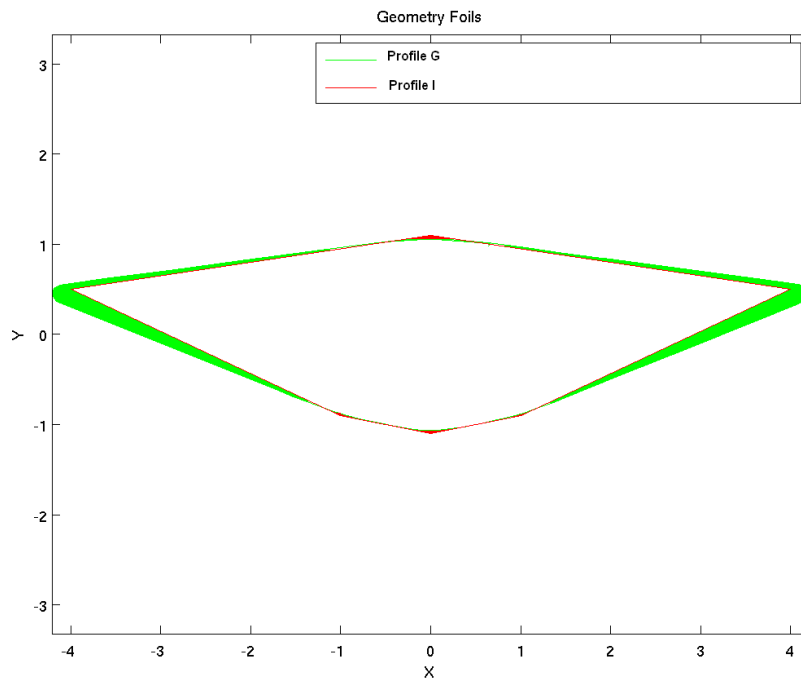


Figure 8.1 : Difference between profile G (green) and profile I (red)

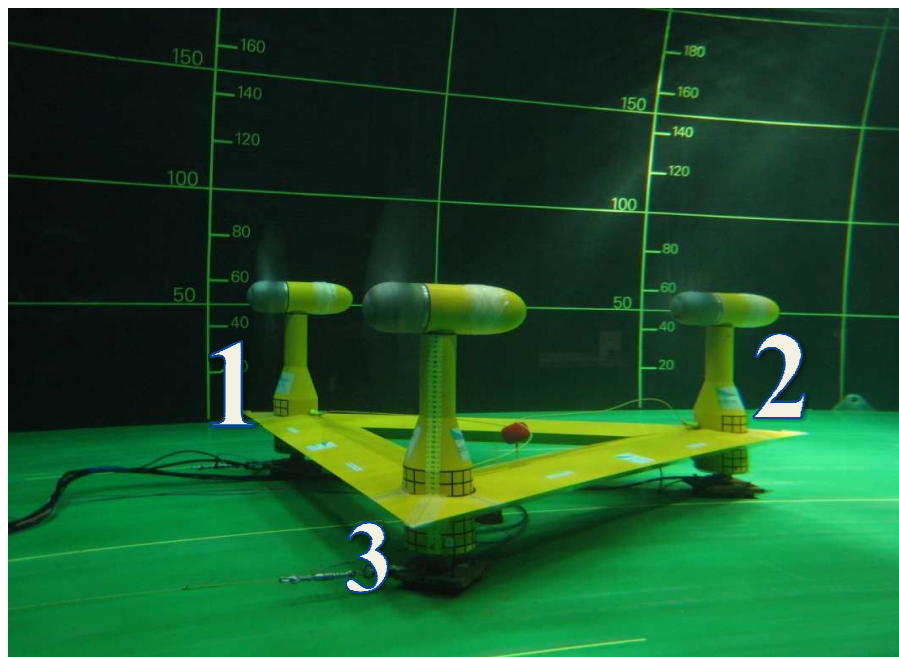


Figure 8.2 : Small scale delta stream structure being tested in the Ifremer water tank

8.1.3 Results

A comparison of the lift and drag force obtained on the structure without and with profiles is shown respectively on Figure 8.3 and Figure 8.4. The lift force is calculated by adding the three components on each foot (top picture of Figure 8.3 and Figure 8.4). Positive values represent a compression on load cells, which means a negative lift, while negative values represent tension on load cells and indicate a positive lift. For the drag force, both starboard and port components must be added.

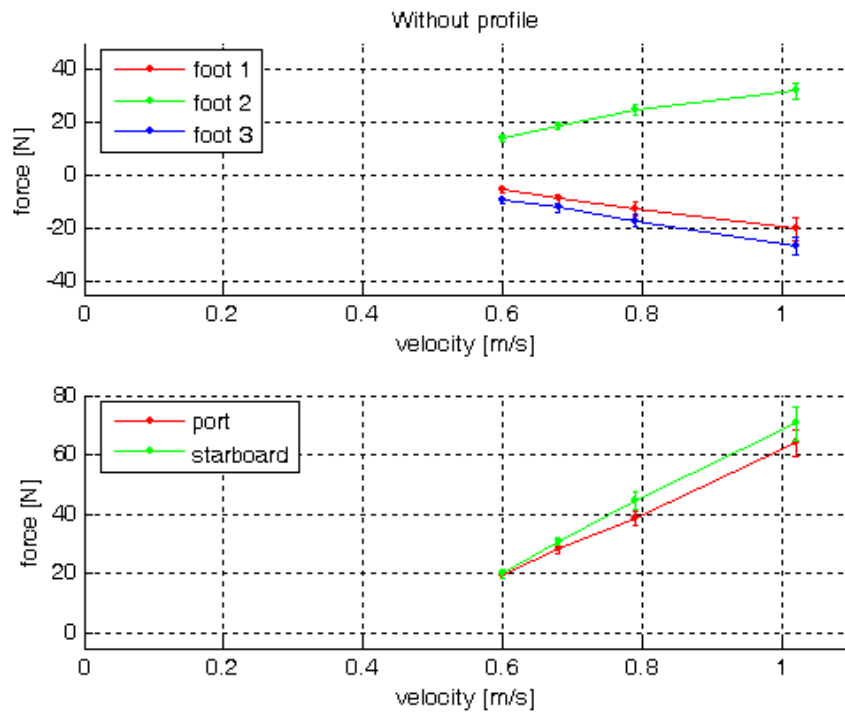


Figure 8.3 : Lift force (top picture) and drag force (bottom picture) measured on the structure without profile

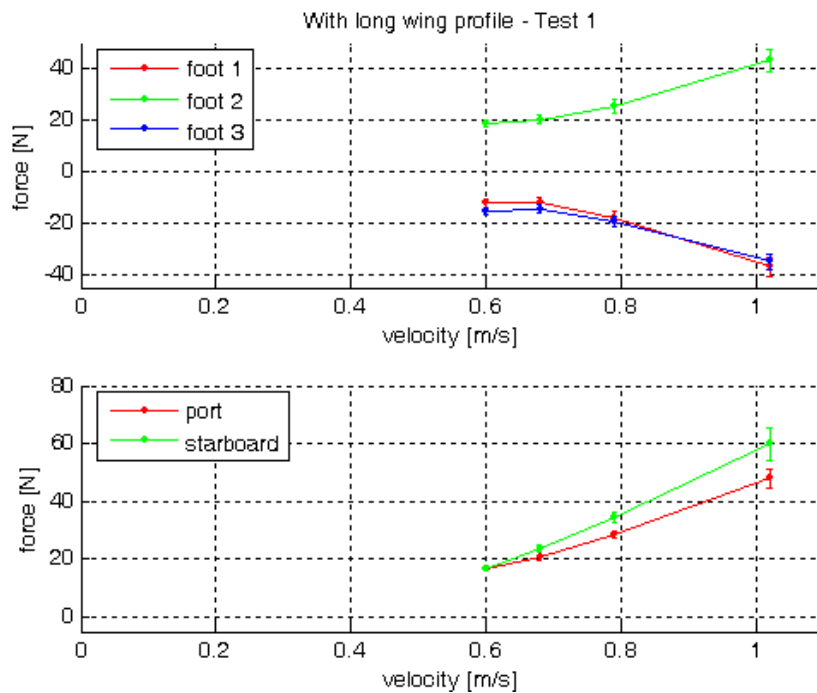


Figure 8.4 : Lift force (top picture) and drag force (bottom picture) measured on the structure with profile I

Without any profile, an upward lift of 20 and 27 N is observed for the feet facing the flow, while a downward lift of 32 N is observed for the foot behind. With profiles I on

the structure, an upward lift of 35 N is observed for the feet facing the flow while there is a downward lift, of 42 N now, on the foot behind. The drag, around 130 N without profile, decreases until 110 N with profile I on the structure.

8.1.4 Conclusion

These results were not expected, since a very poor downward lift is produced by the structure, even with profiles on. These results may be poor because of several reasons: it could be a problem of similitude between full scale and small scale structure. Indeed, the Froude similitude is generally used in naval architecture studies, because it takes into account free surface phenomena and gravity force, and hence it is used to model a structure in waves or when free surface effects are important. But when free surface and gravity are not governing the flow, as for hydro elastic behaviour of risers in the stream, other similitude relationships have to be considered. The Reynolds similitude, for example, respects viscous effects [28]. So the Froude similitude used here may be one cause of these unexpected results. Another reason could be the sharper edges on the small scale profile (profile I), which could make a difference from the results obtained in CFD on a similar shape with smoother edges (profile G).

8.2 Complementary two dimensional CFD results

8.2.1 Introduction

Because of unexpected results obtained from tank testing, complementary two dimensional CFD runs are performed, to reach some understanding of the situation. CFD runs on profile I, (small scale and sharp edges) are performed to be compared with tank testing results, to make sure that CFD results are comparable to the tank testing results. I2 profile (full scale and sharp edges) is also compared with profile G (full scale and smooth edges) to find out if the sharper edges can produce a significant difference of lift force compared to smooth edges.

8.2.2 Geometry and set up

The size of the domain is the same as for the one used in Chapter 7:, with 40x35x0.04 m for the full scale domain. For the small scale domain, it is 2x1.16x0.04 m. The

boundary layer is described by a dedicated boundary layer mesh. The model employs a wall function formulation that dispenses with the need to resolve the viscous sublayer. The y^+ is 11. A size function allows the mesh growing up from the foil to the domain boundaries. A typical mesh of 260 000 nodes is used for the full scale domain, and 50 000 for the small scale one.

A velocity profile with 4.5 m/s at the surface is used at the inlet boundary condition for full scale test, to be comparable with profile G at the same velocity. For small scale tests, the same velocity profile as the one measured in the water tank in Ifremer is used, with a surface velocity of 1 m/s. At the outlet, an average static pressure of 300 000 Pa is set in both cases.

8.2.3 Results

8.2.3.1 Comparison between small scale sharp foils and tank testing

The plot of the pressure coefficient distribution on a line around the foil (Figure 8.5) shows that, contrarily to previous pressure coefficient plot, the pressure on the lower face on the foil is not smaller than the pressure on the upper face in the central peak area. The curve of the pressure coefficient on the lower face only crosses the one on the upper face in few points, making a very small area of negative pressure and hence of negative lift. Hence, this curve shows that the small scale profile produces a positive lift in CFD results.

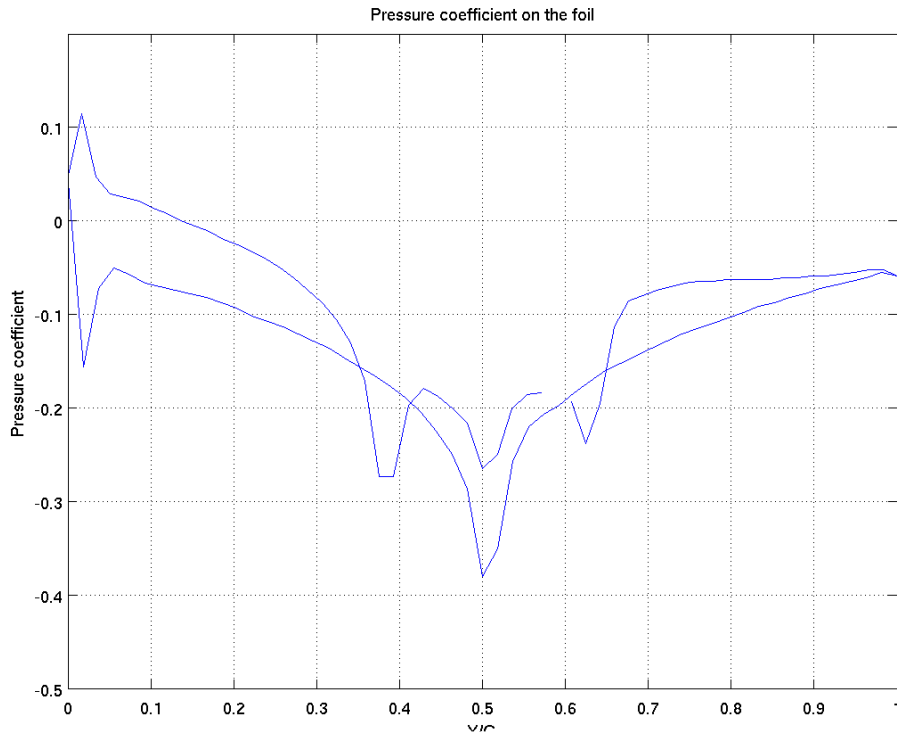


Figure 8.5 : Pressure distribution on a line around foil I

The CFD results for the small scale profile are a production of upward lift force of 0.227 N on a 4 cm slice of foil, and 0.058 N of drag. To get the total drag and lift on the structure in CFD, some assumptions have to be made:

- Foils of 20 m length were considered in full scale, which means that they are 0.667 m in small scale. So results on the 4 cm slice are multiplied by 25 to have the value on a one meter foil, and multiplied again by 0.667 to have the value on the foil facing the flow in tank testing scale.
- There are three foils on the structure, but each of the two foils which are not facing the flow is expecting to produce half of the lift force produced by the foil facing the flow.

To get the total drag and lift produced by the structure in tank testing, values shown on Figure 8.4 are considered, and total lift and drag are calculated as follows:

- For the lift, the resulting value is the sum of the individual components on each foot.
- For the drag, both starboard and port components must be added.

So results are comparable and presented in the following table:

	Tank	CFD prof I
Lift	-28 N	7.5 N
Drag	110 N	3 N

Table 8.1 : Drag and Lift on the structure for tank testing and CFD results in small scale.

When considering lift results, tank testing results show a small downward lift while CFD results are producing a very small upward lift. But the order of the quantity of lift produced is the same and around zero. For the drag force, results from tank testing are a bit more substantial than CFD results, but still in the same order. Small differences observed between both ways of estimating drag and lift can be explained because tank testing was performed on the whole structure with turbines on, whereas CFD results are only made on a very small slice of the foil and don't consider the turbines. The main conclusion of this comparison is, when keeping in mind the structural differences in the two tests, CFD results seem to match tank testing results.

8.2.3.2 Full scale comparison between sharp and smooth shape

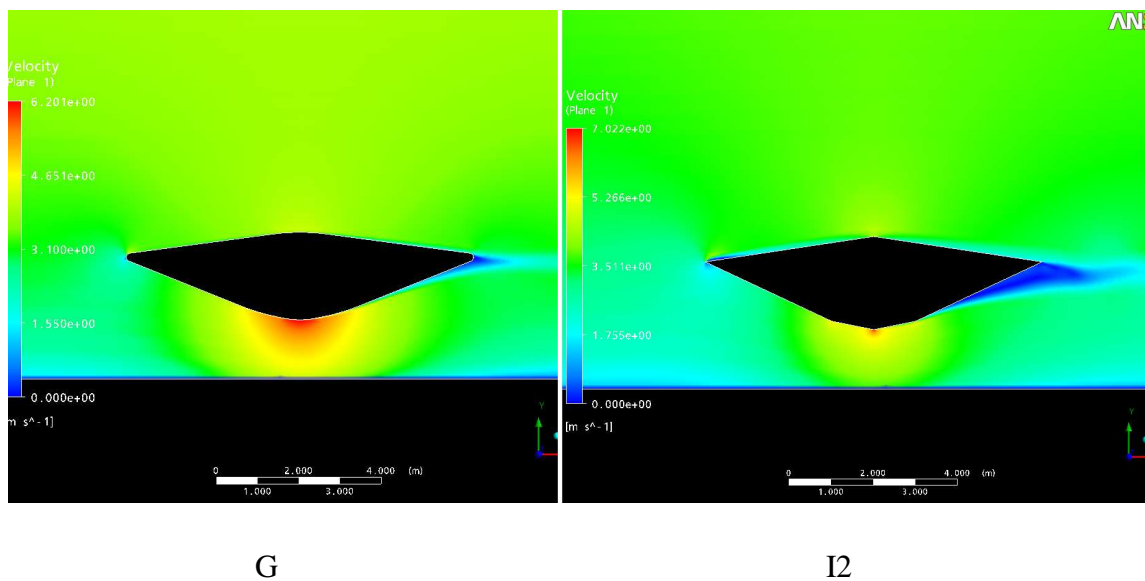
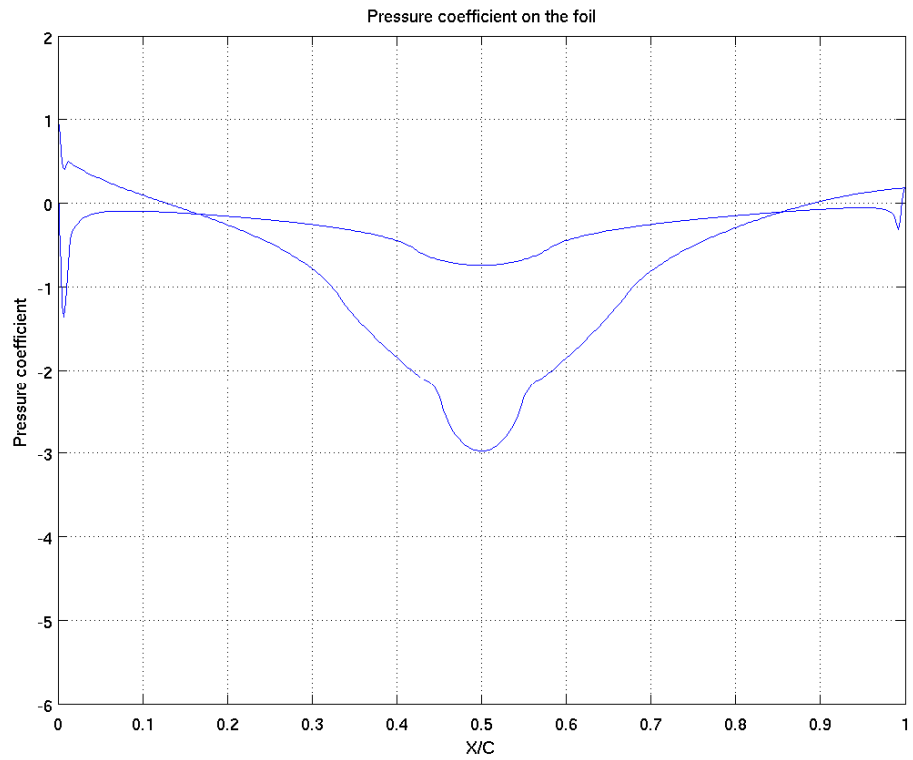
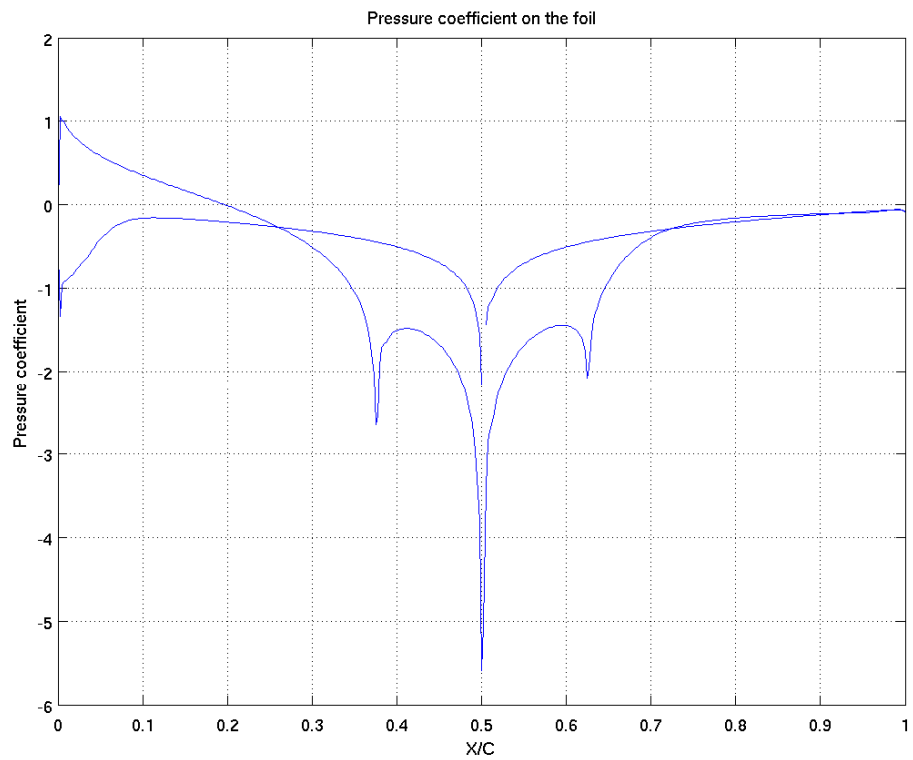


Figure 8.6 : Full scale comparison between smooth (G) and sharp (I2) edges profile.

Figure 8.7 shows the pressure distribution on a line around the foil.



G



I2

Figure 8.7 : Pressure distribution on a line around foils G and I2

The difference of shape appears clearly with the presence of peaks value on the sharper edges of foil I2, which decrease significantly the area defined by the difference of pressure coefficient between the upper and the lower face of the foil, representing the quantity of negative lift. Hence, the quantity of negative lift is much greater for profile G than for profile I2, while the only difference between these two foils is the sharp edges.

The quantity of lift and drag generated by profile G and I2 is shown in the following table:

	G	I2
Lift	-488 900 N	-187 000 N
Drag	18 100 N	35 200 N

Table 8.2 : Drag and Lift of a 22 m length full scale profile. G: smooth, I2: sharp.

The comparison of two profiles of comparable shape, one being smoother than the other one, is very significant in that it highlights the importance small details can have on the overall hydrodynamic behaviour. As shown on Figure 8.6, the wake separation on profile I2 appears just after the bottom sharp edge, and creates a much bigger wake than profile G, with an oscillation of the wake behind the profile. In terms of drag and lift influence, profile I2 produces only 38% of the downward lift generated by profile G, whereas the drag of profile I2 is twice the drag generated by profile G. Hence, small changes on geometry can produce drastically different results in terms of hydrodynamic efficiency.

8.2.4 Conclusion

Tank testing and CFD results comparison in small scale shows that CFD produces consistent results, when comparable profiles are employed. Hence, even if tank testing does not validate the interest of foil “I” to produce downward lift, it does validate that CFD produces trustworthy results since they match together. Hence, CFD results have shown that in full scale, the profile I2 is not suitable to produce a sufficient quantity of downward lift, compared to a similar smoother shape. This happened because of sharper edges which create angles, and these angles encourage the wake to detach

upstream. The effect of angles on the pressure coefficient distribution has been shown since peak values are present where sharp edges create angles, and this feature shows the importance of having a perfectly smooth profile to generate lift.

Chapter 9: Conclusion

The main objectives of this study were to show that downward lift can be produced by fitting a hydrofoil to the delta structure and to study the influence of different foil parameters on the size of downward lift generated.

The first stage of the hydrofoil investigation study showed that a distorted profile provides a larger downward lift force than a symmetrical profile. Hence, a more distorted shape can produce an amount of downward lift, which even if it is not enough to maintain the structure in its location can nevertheless help reduce the cost of traditional mooring by dead ballast such as concrete or steel.

However, the performance of the deformed profile element is not enough to produce the expected downward force, because of the proximity from the ground which reduces the lift potential of the foil. One result presented in this study shows that a profile produces a lift force which is dependent on the distance above the ground. Hence, the further the profile is away from the ground, the greater the downward lift force is. An additional parameter which can be changed is the chord of the profile: as the profile chord grows so the lift rises and the drag decreases, showing that a longer chord profile has a better hydrodynamic shape to obtain the downward lift force.

However, the requirements of the industrial project impose that an easy to build profile be used, structurally sound and not too expensive to construct. These requirements are essentially met by using the smallest amount of profiling material. The distance from the sea floor is set at 2.5 m for the prototype and can not be changed if foils are positioned on the horizontal structural pipes. These constraints imply that the profile shouldn't be very distorted, because it would induce the occurrence of large regions of separated flow and lead to reduced negative lift, its chord can not be too large, because

it would imply a large quantity of glass fibre to be built, and if it is set on the horizontal pipes that make up the delta structure, it can not be further away from the ground, because the horizontal pipes are 2.5 m from the sea floor.

Keeping in mind those aspects, only the profile chord could actually be changed, and a thickness to chord ratio of $\frac{1}{4}$ is shown to be the best compromise. Based on this shape, tank tests were performed, and the very small downward lift observed in these tests, led to further investigations being carried out to explain those results.

Two major facts could be pointed out as the reasons of such a difference between tank testing and CFD results. First, the similitude law employed in tank testing can either conserve the Froude number or the Reynolds number. Here, the choice to conserve the Froude number could be the cause of a bad representation of viscous effects, and hence, of lift and drag forces. Second, the shape tested in the tank trials was slightly different than the shape modelled in CFD, it had sharper edges and these encouraged boundary layer separation.

In order to examine if these hypotheses were correct, a number of additional runs were performed in CFD. In the first one the same geometry as used in the tank testing was modelled. The model had the same dimensions, the same profile with sharp edges and was simulated at the same velocity used in the tank tests. The numerical results showed the same order of results as those obtained in tank testing, and the difference can be explained by the presence or not of vertical piles with the turbines. The second run showed the difference of lift force between profiles having the same characteristics but one having sharper edges than the other. The sharp edges profile produced only 38% of the lift produced by the smooth edges profile.

Hence, these additional runs show that the CFD runs are not the source of the discrepancy between the experimental tank testing and numerical results since when modelling the same thing, both results are in accordance. The CFD runs don't prove that Froude similitude was a problem, but they prove that the profile shape needs to be smooth as what could look like a small building detail makes a significant difference in term of drag and lift produced.

The outcome of this work is that yes, such profile could potentially provide enough or contribute significantly to the generation of down-thrust. It is not possible at this stage of the project to confirm the exact proportion of down-thrust required for the device to remain stationary on the seabed. The reason is the following: the velocity at which the turbine starts to shed power is 2.25m/sec so the maximum thrust (horizontal force on the device) is to be found at that flow velocity. The maximum horizontal force is the sum of the thrust generated by each turbine (30 Tonnes each) and the hydrodynamic drag on the supporting structure which has been estimated to 40 Tonnes at 2.25 m/sec so the max horizontal force will be 130 Tonnes at 2.5 m/sec. The reason is that the turbine thrust decreases sharply after 2.25 m/sec due to design peculiarities of that turbine.

To conclude, the main merit of this study was to highlight the fact that negative lift can be produced such as to dynamically anchor, if not totally at least to a large measure, a tidal generation device. The performance of this anchorage method could however be further exploited if free from the current industrial constraints. The different parameters influencing this negative lift generation have been detailed, and two major foil shapes are proposed. At a thickness to chord ratio of $\frac{1}{4}$, a more distorted profile can produce more lift force but could be more expensive and have a less structurally sound configuration. The less distorted profile produces approximately 20% less lift but is cheaper to construct and likely safer structurally.

Chapter 10: Future work

There is a need for extensive evaluation of the lift generated by hydrofoils in a tidal stream current, to get more information about the lift force in both tidal stream directions. Additional ideas of how to increase the lift force generated are proposed as well.

The observations presented in this thesis were performed on the basis of individual sections of the foil facing the flow on the delta shape. These sections are a small thickness of 4 cm, and the results obtained are then multiplied to get the lift on a 25 m length hydrofoil. In order to estimate the lift generated by the two other foils of the delta, cases could be run with an angle between the inlet velocity and the foil. This would give an estimation of the drag generated by the two other foils in the two directions of the tidal stream.

However, to take into account the interaction between the three foils, and since this interaction is not the same depending on the tidal stream direction, an estimation of the lift generated by the three foils would produce better results by directly computing the three dimensional model of the structure.

To increase the quantity of lift generated, an idea inspired from high-lift devices on aerofoils, such as slats, to accelerate the boundary layer and to retard the boundary layer separation could be considered. The case of a profile with a slat could be studied to estimate in how much quantity the lift force would be improved.

The findings of this work are valuable contributions to the offshore industry, with particular regards to the proof of concept of the development of a new anchoring system. This proof of concept has to be considered in the range of conditions tested here and further investigation will determinate the application of the concept to other conditions.

REFERENCES

1. Anderson, J., Degrez, G., Degroote, J., Dick, E., Grundmann, R., Vierdendeels, J. (2009) *Computational Fluid Dynamics : An introduction*. 3rd ed.
2. Ansys-CFX (2006) Theory guide
3. Balme, R., Le Saux, K., (2007) "A simulation model for the evaluation of the electrical power potential harnessed by a marine current turbine in Raz de Sein", *IEEE*.
4. Blevins, R.D, (1990) *Flow induced vibration*, Van Nostrand Reinhold, New York.
5. Boyle, G., (2004) *Renewable energy: power for a sustainable future*, 2nd ed., Oxford University Press.
6. Bryden, I. G. and Couch, S. J. (2006), "ME1—marine energy extraction: tidal resource analysis", *Renewable Energy*, vol. 31, no. 2, pp. 133-139.
7. Charlier, R. H. (2003), "A "sleepers" awakes: tidal current power", *Renewable and Sustainable Energy Reviews*, vol. 7, no. 6, pp. 515-529.
8. Daskovsky, M. (2000), "The hydrofoil in surface proximity, theory and experiment", *Ocean engineering*, vol 27, pp 1129-1159.
9. Denny, E. (2009), "The economics of tidal energy", *Energy Policy*, vol. 37, no. 5, pp. 1914-1924.
10. DNV-RP-C205, recommended practice, environmental conditions and environmental loads, April 2007.
11. Fay, (1983) "Performance of small-scale tidal power plants", *Journal of energy* [0146-0412], vol. 7, no.6, pp.529 -535.
12. Freeman, C., Amaral Teixeira, J., Trarieux, F., Ayre, R. (2009) " Design of a gravity stabilised fixed pitch tidal turbine of 400 kW ", *Proceedings of the 8th European Wave and Tidal Energy Conference, Uppsala, Sweden*.
13. Gerwick, B.C, (2000) *Construction of marine and offshore structures*, 2nd ed.
14. Hagerman, G., Polagye, B., Bedard, R., and Previsic, M. (2006) "EPRI guideline methodology for estimating tidal current energy resources and power

production by tidal in-stream energy conversion (TISEC) devices”. Electric Power Research Institute.

15. Hefazi, H., Kural, O., Chen, H., and Cebeci, T. (1998) “Hydrofoil design and optimization for fast ships”, *Proceedings of the 1998 ASME International Congress and Exhibition Anaheim, CA*.
16. Hoerner (1956), Fluid dynamic drag.
17. Hoerner (1958), Fluid dynamic lift.
18. Houghton, E.L., Carpenter, P.W. (2003), Aerodynamics for engineering students, 5th ed.
19. Hsin, C., Wu, J. and Chang, S. (2006), "Design and optimization method for a two-dimensional hydrofoil", *Journal of Hydrodynamics, Ser.B*, vol. 18, no. 3, Supplement 1, pp. 323-329.
20. Jacobs, E.N, Ward, K.E., and Pinkerton R.M., (1933) “The characteristics of 78 related airfoil sections from tests in the variable-density wind tunnel”, *NACA Report No. 460*.
21. Khan, M. J., Bhuyan, G., Iqbal, M. T. and Quaicoe, J. E. (2009), "Hydrokinetic energy conversion systems and assessment of horizontal and vertical axis turbines for river and tidal applications: A technology status review", *Applied Energy*, vol. 86, no. 10, pp. 1823-1835.
22. Launder, B.E, Spalding, D.B (1974) "The numerical computation of turbulent flow", *Computational Mechanics in Applied Mechanics and Engineering*, vol. 3 pp.269.
23. Liu, Z., Hyun, B., Kim, M. and Jin, J. (2008), "Experimental and numerical study for hydrodynamic characteristics of an oscillating hydrofoil", *Journal of Hydrodynamics, Ser.B*, vol. 20, no. 3, pp. 280-287.
24. MacCormack, R.W., Paullay, A.J. (1972), “Computational efficiency achieved by time splitting of difference operators”, *AIAA papers 72-154*.
25. Marsh, G. (2004), "Tidal turbines harness the power of the sea", *Reinforced Plastics*, vol. 48, no. 6, pp. 44-47.

26. McDonald, P.W (1971) “The computation of transonic flow through two dimensional gas turbine cascades”, *ASME Paper 71-GT-89, Gas Turbine Conference and products show*, Houston, Texas.
27. Moe, G. and Verley, R.L.P (1980) “Hydrodynamic damping of offshore structures in waves and currents”, *Proceedings of the OTC*, 37, 44.
28. Molin, B. (2002), *Hydrodynamique des structures offshores, Ed. Technip*.
29. Myers, L., Bahaj, A.S. (2006), “Power output performance characteristics of a horizontal axis marine current turbine”, *Renewable energy*, vol. 31, pp 197-208.
30. Pranesh, M.R. and Mani, J.S. (1988) “Similitude engineering – ocean structure interaction” *Ocean engineering*, vol 15, No2, pp 189-200.
31. Rizzi, A.W., Inuoye, M., (1973) “Time split finite volume method for 3D blunt body flows”, *AIAA Journal*, vol. 11, pp 1478-1485.
32. Rosen, B., Laiosa, W. and Davis, W. (2000) “CFD studies for America’s cup 2000”, AIAA 2000-4339
33. Shaw, C.T. *Using computational fluid dynamics*, ed. Prentice Hall.
34. Triton Consultants Ltd. (2006), “Potential tidal current energy resources— analysis background”. Canadian Ocean Energy Atlas (Phase 1) Report to NRC Canadian Hydraulics Centre as part of contract to Natural Resources, Canada.
35. Tritton D.J. (1977) *Physical Fluid dynamics*. 1st edition, pp 28-29, pp 109.
36. Tu, J., Yeoh, G.H., Liu, C. (2008) *Computational Fluid Dynamics: a practical approach*.
37. The Carbon Trust, (2006), “Future Marine Energy”
38. Westwood, A. (2004), "Ocean power: Wave and tidal energy review", *Refocus*, vol. 5, no. 5, pp. 50-55.
39. www.marineturbines.com
40. National Air and Space Museum of Washington
www.nasm.si.edu/exhibitions/gal109/NEWHTF/HTF513B.HTM

41. Xie, N. and Vassalos, D. (2007), "Performance analysis of 3D hydrofoil under free surface", *Ocean Engineering*, vol. 34, no. 8-9, pp. 1257-1264.

APPENDIX 1: SUMMARY OF PROFILE NAMES AND CHARACTERISTICS

Name of the profile in the thesis	Name of the file .res in CFX	Description of the profile
A	tube1_3_Omesh_004	symmetrical profile, no plate thickness, height to width ratio 1/3, at 2.5 m from the ground
B	tube2_2O_004	asymmetrical profile at 0.5 above centre, no plate thickness, ratio 1/3, at 2.5 m from the ground
C	tube3_008	asymmetrical profile at 0.5, with plate thickness, ratio 1/3, at 2.5 m from the ground
C2	tube3_3_002	asymmetrical profile at 0.5, with plate thickness, ratio 1/3, at 10 m from the ground
D	tube2F_009	asymmetrical profile at 0.7, with plate thickness, ratio 1/3, at 2.5 m from the ground
E	tube3_2_003	asymmetrical profile at 0.7, with plate thickness, ratio 1/5, at 2.5 m from the ground
F	tube3_8_004	asymmetrical profile at 0.5, with plate thickness, ratio 1/3.5, at 2.5 m from the ground
G	tube3_4_002	asymmetrical profile at 0.5, with plate thickness, ratio 1/4, at 2.5 m from the ground
H	tube3_7_002	asymmetrical profile at 0.7, with plate thickness, ratio 1/4, at 2.5 m from the ground
I	profile4_reducedscale2_012	asymmetrical profile at 0.5, with plate thickness, ratio 1/4, with sharp edges, scale 1/30
I2	profile4_fullscale_009	asymmetrical profile at 0.5, with plate thickness, ratio 1/4, with sharp edges, full scale

APPENDIX 2: MATLAB SCRIPT TO COMPUTE THE VELOCITY PROFILE ACCORDING TO 7TH POWER LAW

```
1 %Open a file and write the heading necessary for a velocity profile in CFX
2 - fid = fopen ('velocity_4p5_half_struct.csv','w');
3 - fprintf(fid, '# 4.5 m/s profile boundary condition\n\n');
4 - fprintf(fid, '[Name]\n');
5 - fprintf(fid, 'Profile4p5ms0p04y2p5x15\n');
6 - fprintf(fid, '[Spatial Fields]\n');
7 - fprintf(fid, 'x , y , z\n');
8 - fprintf(fid, '[Data]\n')
9 - fprintf(fid, 'x[m], y[m], z[m], u[m s^-1], v[m s^-1], w[m s^-1]\n')
10
11 %Initialize all variables to their future size and fill of zeros
12 - x=zeros(71,1);
13 - y=zeros(71,1);
14 - z=zeros(71,1);
15 - u=zeros(71,1);
16 - v=zeros(71,1);
17 - w=zeros(71,1);
18
19 % change the Uinf= change the infinite velocity at the sea surface (top of
20 % domain)
21 - Uinf=4.5;
22
23 %Start the loops
24 % j: step along the thickness of the domain ( z direction)
25 % i: step along the depth of the domain (y direction)
26 - for j=0:0.02:0.04
27 - for i=1:71
28 %The velocity profile will be set at the entrance of the domain,
29 % In x=-15 compare to the centre of the XYZ axis
30 % with a depth y varying from -2.5m to 32.5 m
31 % with a thickness z varying from 0 to 0.04 m
32 - x(i,1)=-15;
33 - y(i,1)=((i-6)*0.5);
34 - z(i,1)=j;
35 % The velocity in each point is calculated according to seventh power law
36 - u(i,1)=-Uinf*((y(i,1)+2.5)/35)^(1/7);
37 % The velocity in each direction is written for each point on the inlet:
38 - fprintf(fid, '%5.2f, %5.2f, %5.2f, %5.2f, %5.2f, %5.2f\n', x(i), y(i), z(i), u(i), v(i), w(i))
39
40 - end
41 - end
42 - status=fclose(fid);
```

APPENDIX 3: MATLAB SCRIPT TO PLOT DRAG AND LIFT EVOLUTION FROM MONITOR POINTS FILE

```

1 %*****
2 % This routine computes:
3 % Inputs are: Forces normal and tangent /X&Y drag and lift
4 % Outputs are: plot of drag and lift versus time
5 % Date: 10.11.08
6 %*****
7
8 % Monitor file options .out is converted to a file named ...out.csv
9 % Data from the ...out.csv file is read from line 32500 (where our
10 % considered data starts to be written, must be change in each file)and
11 % stored in the variable called "data"
12 data=csvread('/home/CCNT/c119304/profile4fullscale/profile4fullscale_009out.csv',32500,0);
13
14 % Parameters written in the .csv file are first listed, starting by @start
15 % and finishing by @end. If the force normal in X direction is the 17th
16 % variable name to be listed after @start, data will be written after the
17 % @end in the 17th column.
18 % In our case columns used in .csv file to calculate the drag and lift are:
19 FORCEXnormal=data(:,17);
20 FORCEYnormal=data(:,18);
21 FORCEXtangent=data(:,20);
22 FORCEYtangent=data(:,21);
23 time=data(:,4);
24
25 % As drag and lift are oscillating, we want to calculate a mean value when
26 % drag and lift are oscillating around a stable mean value (converged zone).
27 % In the mean value will be calculated on the 10 000 last values of the
28 % drag and lift vectors.
29 n=length(FORCEXnormal);
30 indstart=n-10000;
31 indend=n;
32
33 % calculation of drag and lift, and mean values
34 drag=FORCEXnormal+FORCEXtangent;
35 lift=FORCEYnormal+FORCEYtangent;
36 meandrag=mean(drag(indstart:indend));
37 meanlift=mean(lift(indstart:indend));
38
39 % find the biggest and the smallest value of drag and lift in the converged
40 % zone
41 maxdrag(1,1)=max(drag(indstart:indend));
42 maxdrag(1,2)=min(drag(indstart:indend));
43 for i=indstart:indend
44     if maxdrag(1,1)==drag(i)
45         indmax(1,1)=i;
46     end
47     if maxdrag(1,2)==drag(i)
48         indmax(1,2)=i;
49     end
50 end
51 t_maxdrag(1,1)=time(indmax(1,1));
52 t_maxdrag(1,2)=time(indmax(1,2));
53 abs_var_drag=abs(maxdrag(1,1)-maxdrag(1,2));
54 err_drag=(abs_var_drag*100)/meandrag
55
56 maxlift=max(lift(indstart:indend));
57 minlift=min(lift(indstart:indend));
58 for i=indstart:indend
59     if maxlift==lift(i)
60         inlmax=i;
61     end
62     if minlift==lift(i)
63         inlmin=i;
64     end
65 end
66 t_maxlift=time(inlmax);
67 t_minlift=time(inlmin);
68 abs_var_lift=abs(maxlift-minlift);
69 err_lift=abs_var_lift*100/abs(meanlift)

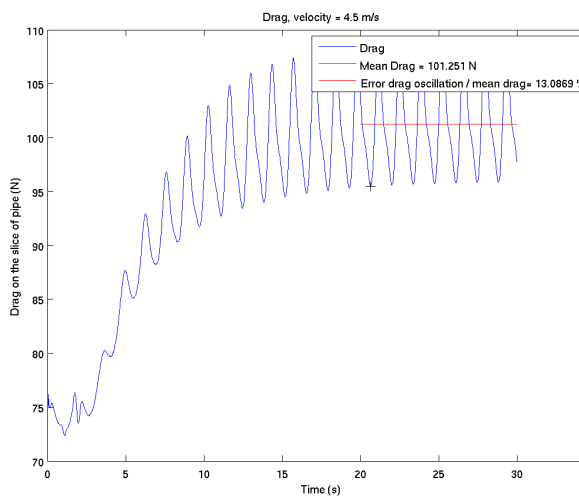
```

```

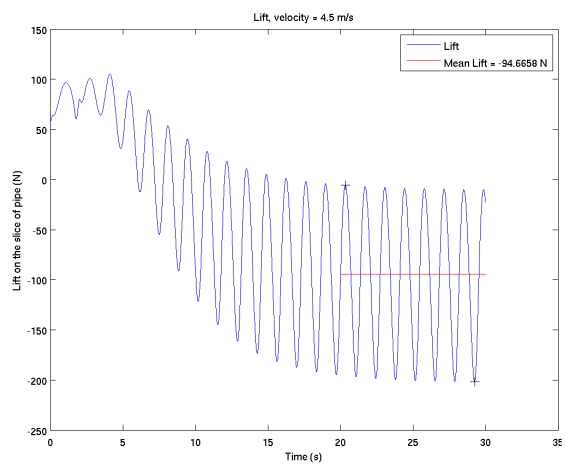
55 -
56 -     maxlift=max(lift(indstart:indend));
57 -     minlift=min(lift(indstart:indend));
58 -     for i=indstart:indend
59 -         if maxlift==lift(i)
60 -             inlmax=i;
61 -         end
62 -         if minlift==lift(i)
63 -             inlmin=i;
64 -         end
65 -     end
66 -     t_maxlift=time(inlmax);
67 -     t_minlift=time(inlmin);
68 -     abs_var_lift=abs(maxlift-minlift);
69 -     err_lift=abs_var_lift*100/abs(meanlift)
70 -
71 -     % plot of drag and lift versus time
72 -     figure(1)
73 -     plot(time, drag,time(indstart:indend),meandrag,'r');
74 -     hold on
75 -     plot(t_maxdrag,maxdrag,'+k','MarkerSize',8)
76 -     xlabel('Time (s)')
77 -     ylabel('Drag on the slice of pipe (N)')
78 -     title('Drag')
79 -     legend('Drag',sprintf('Mean Drag = %g N',meandrag),sprintf('Error drag oscillation / mean drag= %g %%',err_drag))
80 -     print Drag_profile4fullscale_009 -dpng
81 -
82 -     figure(2)
83 -     plot(time, lift);
84 -     hold on
85 -     plot(time(indstart:indend),meanlift,'r')
86 -     plot(t_maxlift,maxlift,'+k','MarkerSize',8)
87 -     plot(t_minlift,minlift,'+k','MarkerSize',8)
88 -     xlabel('Time (s)')
89 -     ylabel('Lift on the slice of pipe (N)')
90 -     title('Lift')
91 -     legend('Lift',sprintf('Mean Lift = %g N',meanlift))
92 -     print Lift_profile4fullscale_009 -dpng
93 -

```

When running the Matlab script for profile D for example, the code make the two following pictures :



Drag profile D



Lift profile D

